Selective chemical looping combustion of acetylene in ethylene-rich streams

Matthew Jacob[1], Huy Nguyen[1], Rishi Raj[1], Javier Garcia-Barriocanal[2], Jiyun Hong[3], Jorge E. Perez-Aguilar[3], Adam S. Hoffman[3], K. Andre Mkhoyan[1], Simon R. Bare[3], Matt Neurock[1], Aditya Bhan[1*]

Affiliations:

[1]: Department of Chemical Engineering and Materials Science, University of Minnesota; Minneapolis, MN 55455, United States

[2]: Characterization Facility, University of Minnesota; Minneapolis, MN 55455, United States

[3]: Stanford Synchrotron Radiation Lightsource, SLAC National Accelerator Laboratory; Menlo Park, CA 94025, United States

[*]: Corresponding author. Email: abhan@umn.edu

Abstract:

The requirement for C_2H_2 concentrations below 2 parts per million (ppm) in gas streams for C_2H_4 polymerization necessitates its semi-hydrogenation to C_2H_4. We demonstrate selective chemical looping combustion of C_2H_2 in C_2H_4-rich streams by Bi_2O_3 as an alternative catalytic pathway to reduce C_2H_2 concentration below 2 ppm. Bi_2O_3 combusts C_2H_2 with a first-order rate constant that is 3000 times greater than the rate constant for C_2H_4 combustion. In successive redox cycles, lattice oxygen of Bi_2O_3 can be fully replenished without discernible changes in local Bi coordination or C_2H_2 combustion selectivity. Heterolytic activation of C-H bonds across Bi-O sites and the higher acidity of C_2H_2 results in significantly lower barriers for C_2H_2 activation than C_2H_4, enabling selective catalytic hydrocarbon combustion leveraging differences in molecular deprotonations energies.

C_2H_2 concentrations in C_2H_4 must be < 2 ppm to prevent deactivation of C_2H_4 polymerization catalysts (*1–3*). Industrially, the most common route to produce C_2H_4 involves steam cracking of saturated hydrocarbon feedstocks such as naphtha, which results in C_2H_2 formation as a by-product up to 2.5 wt% (*4*, *5*). C_2H_2 semi-hydrogenation on Pd-based catalysts at temperatures ranging from 373 to 523 K and moderate pressures of ~ 5 bar is used to enhance C_2H_4 yields and reduce C_2H_2 concentrations < 2 ppm (*6*). To enable C_2H_2 semi-hydrogenation at appreciable rates, the catalyst must be proficient in adsorbing H_2 and C_2H_2 but desorb C_2H_4 before it can be further hydrogenated or oligomerized. Alloying Pd-based catalysts with other metals such as Ag (*7–10*), Ga (*11*), or Cu (*12*, *13*) improves C_2H_4 yields by modifying the electronic properties of the active site to either bind C_2H_2 or H_2 more strongly, enhancing rates, or lowering the barrier for C_2H_4 desorption relative to the barrier for the thermodynamically favored hydrogenation to C_2H_6, thus enhancing selectivity. However, modification of the electronic properties of the active site to decrease the barrier for C_2H_4 desorption typically results in weaker adsorption of C_2H_2, leading to lower rates (*7*, *8*, *10*).

An alternative strategy to selectively remove C_2H_2 from C_2H_4-rich gas streams utilizes a reducible oxide to selectively activate the C-H bonds of C_2H_2, initiating a reaction cascade which results in combustion. Hydrocarbon combustion at high temperatures (>1000 K) with O_2 cofeeds is a radical-mediated process that results in the indiscriminate activation of hydrocarbons and in limited selectivity to combustion of one hydrocarbon in a mixture (*14*, *15*). The use of a solid oxygen-carrier as the active oxidant for hydrocarbon combustion in the absence of gaseous O_2 has been demonstrated with numerous material formulations, but no selective hydrocarbon combustion processes have been reported.

By using an oxide with active sites that selectively activate C-H bonds of C_2H_2, lattice O can be discharged stoichiometrically to combust C_2H_2 in mixtures with C_2H_4 during reduction half cycles and replenished by air during oxidation half cycles. Separation of the reduction and oxidation half cycles avoids flammability concerns associated with high-temperature combustion and the formation of unselective oxygen species upon the conversion of molecular oxygen (O_2). The viability of such a process is predicated upon the selectivity for C_2H_2 combustion during reduction half cycles and the regenerability of the oxide after redox cycling.

Bi_2O_3, a post-transition metal oxide with highly reducible (*16*) and mobile lattice oxygen (*17, 18*) which has been utilized in fuel cells as a solid electrolyte (*18, 19*), in gas sensing applications (*20, 21*), and as a selective hydrogen combustion catalyst (*22-25*), is reported herein to reduce C_2H_2 concentrations below 2 ppm in C_2H_4-rich streams in chemical looping operation. The regenerability of C_2H_2 combustion rates in successive stoichiometric redox cycles in which 20 to 30% of O atoms in Bi_2O_3 are removed during each reduction step and fully replenished with O_2 demonstrates the feasibility of removing trace quantities of C_2H_2 in mixtures with excess C_2H_4. Kinetic analyses show that the rate constant for C_2H_2 combustion, which is unconvoluted by diffusion of O to catalytically relevant surfaces, exceeds the C_2H_4 combustion rate constant by a factor of 3000, a property afforded by heterolytic C-H activation on Bi-O sites. Redox cycling significantly changes Bi_2O_3 surface morphology without the formation of new Bi or Bi_2O_3 phases with lower selectivity to C_2H_2 combustion.

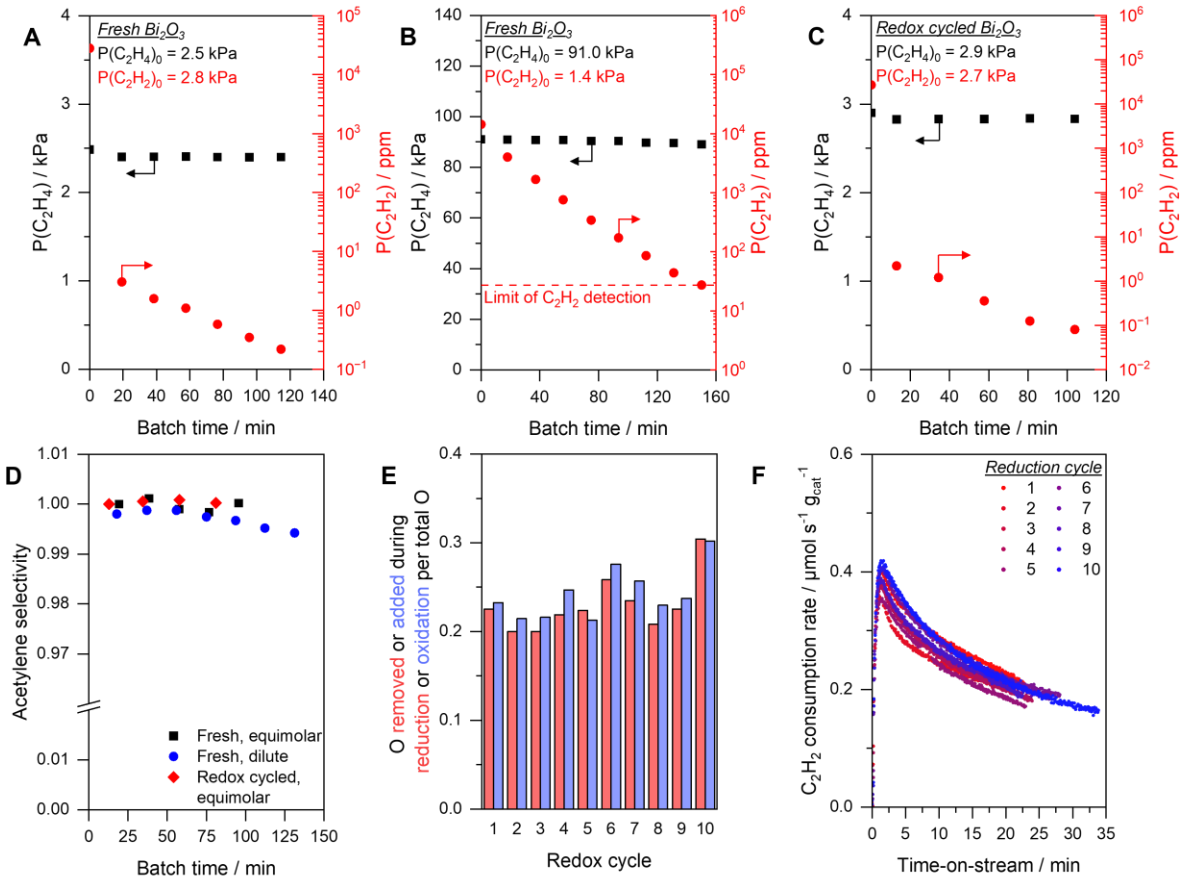

Fig. 1: Demonstration of selective removal of C_2H_2 from C_2H_4 streams
Selective catalytic combustion of C_2H_2 in C_2H_4 for fresh Bi_2O_3 in (**A**) an equimolar mixture and (**B**) a dilute mixture and for (**C**) redox cycled Bi_2O_3 in an equimolar mixture. (**D**) C_2H_2 selectivity as a function of batch time for the data shown in (**A-C**) ($S = \frac{\hat{k}(C_2H_2)}{\hat{k}(C_2H_2)+\hat{k}(C_2H_4)}$, where $\hat{k}$ denotes the first-order rate constant for the consumption of C_2H_2 or C_2H_4, in μmol s^{-1} g_{cat}^{-1} kPa^{-1}). (**E**) The amount of oxygen removed or added from the catalyst in each redox cycle, relative to the total number of O atoms in fresh Bi_2O_3, and (**F**) rates of C_2H_2 consumption in the reduction cycles of successive chemical looping reduction/oxidation cycles. Batch reaction conditions for (**A**): $m(Bi_2O_3)$=251.1 mg, T=773 K, $P(C_2H_4)_0$=2.5 kPa, $P(C_2H_2)_0$=2.8 kPa, $P(He)_0$=6.4 kPa, balance N_2. Batch reaction conditions for (**B**): $m(Bi_2O_3)$=254.7 mg, T=663 K, $P(C_2H_4)_0$=91 kPa, $P(C_2H_2)_0$=1.4 kPa, $P(He)_0$=6.4 kPa, balance N_2. Batch reaction conditions for (**C**): m(redox cycled Bi_2O_3)=261.0 mg, T=773 K, $P(C_2H_4)_0$=2.9 kPa, $P(C_2H_2)_0$=2.7 kPa, $P(CH_4)_0$=5.3 kPa, $P(He)_0$=45.9 kPa, balance N_2. Flow reaction conditions for (**E** and **F**): $m(Bi_2O_3)$=1004.2mg, T=673 K. Reduction conditions: $P(C_2H_4)_0$=$P(C_2H_2)_0$=1.1kPa, $P(CH_4)_0$=1.4 kPa, $P(N_2)_0$=20.9 kPa, balance argon, total flow rate=1.67 cm^3_{STP} s^{-1}. Oxidation conditions: $P(O_2)_0$=2.4 kPa, $P(He)_0$=21.8 kPa, balance argon, total flow rate = 1.67 cm^3_{STP} s^{-1}. The catalyst was isolated in 0.17 cm^3_{STP} s^{-1} He between reduction and oxidation treatments.

Reaction studies

We exposed C_2H_2 and C_2H_4 to bulk Bi_2O_3 with a BET surface area of 0.2 m^2 g^{-1} in an air-free recirculating batch reactor system (see Fig. S1 for a reactor schematic). The mass loading of Bi_2O_3, and thus the amount of O available for reaction, was modulated to ensure that < 20% of lattice O atoms were removed during reduction half-cycles in a recirculating batch reactor. Upon exposure of an equimolar mixture of C_2H_2 and C_2H_4 to Bi_2O_3 at 773 K (Fig. 1A), the C_2H_2 partial pressure dropped from 28,000 ppm to 3 ppm within 20 min, whereas the C_2H_4 partial pressure dropped from 2.48 kPa to 2.40 kPa. The C_2H_2 concentration dropped < 1 ppm within 1 hour, and the C_2H_4 partial pressure remained at 2.40 kPa.

The feasibility of selective C_2H_2 combustion was examined with a 65:1 C_2H_4:C_2H_2 molar ratio gas mixture representative of naphtha steam-cracking effluent gas compositions containing up to 1.4 wt% C_2H_2 (*4*). In the dilute mixture (Fig. 1B), the conversions of C_2H_2 and C_2H_4 after 2.5 hours at 673 K were 99.8% and < 2%, respectively, before the C_2H_2 concentration was too low to measure due to overlap with the peak for C_2H_4 in the gas chromatograph. Even after redox cycling in which 20 to 30% of O atoms were removed from the oxide by C_2H_2 combustion and fully replenished by reoxidation with O_2 in 10 successive redox cycles, the redox-cycled Bi_2O_3 sample exposed to an equimolar mixture of C_2H_2 and C_2H_4 at 773 K could reduce C_2H_2 concentration from 26,600 ppm to below 1 ppm in less than 50 min at 773 K whereas C_2H_4 conversion remained < 3% (Fig. 1C).

The selectivities to C_2H_2 combustion, as evaluated by comparison of the pseudo first-order rate constants for C_2H_2 and C_2H_4 consumption in each mixture examined in Fig. 1, A to C, are shown in Fig. 1D. The selectivity to C_2H_2 combustion exceeded 99% in every case, with no change in selectivity observed for a redox-cycled Bi_2O_3 sample relative to a fresh sample, showing that redox cycled Bi_2O_3 remained as effective as fresh Bi_2O_3 in removing C_2H_2 from gas streams containing C_2H_4. These high selectivities persisted despite the transient evolution of the ensemble of exposed active sites during stoichiometric reduction cycles that removed O atoms from the oxide, implying that, on average, the difference in activation barriers for C_2H_2 and C_2H_4 did not change appreciably on the ensemble of Bi-O active sites available for combustion. These results were corroborated computationally (see below) by observation of the same difference in transition state energy for the C-H activation of C_2H_2 and C_2H_4 on Bi-O sites with varying Bi-O bond lengths to simulate real catalysts that were partially reduced to expose active sites with varying coordination environments and surface terminations.

The longevity of Bi_2O_3 used for selective C_2H_2 combustion with repeated redox cycling was evaluated in a flow reactor (refer to Fig. S2 for a reactor schematic). During reduction half-cycles, Bi_2O_3 was exposed to an equimolar mixture of C_2H_2 and C_2H_4 at 673 K to remove lattice O atoms as CO_2 and H_2O. After an intervening purge of the system with inert helium, the partially reduced Bi_2O_3 was exposed to O_2 to replenish lattice O in the bulk metal oxide abstracted during the reduction cycle. Samples referred to hereafter as redox cycled were prepared during this experiment. Fig. 1E shows the integrated amounts of O removed from the oxide as CO_2 and H_2O and added to the oxide from O_2 consumption during reduction and oxidation cycles, respectively, relative to the total amount of O in fully stoichiometric Bi_2O_3.

During the oxidation cycles, all lattice O atoms removed by reduction in equimolar C_2H_2/C_2H_4 could be fully regenerated, as illustrated by O removed during the reduction step being equal to the O added during the subsequent oxidation step. Differences in O removed or added reflect slight variations in the length of the reduction step; the last reduction step was allowed to progress for slightly longer and removed 35% of O atoms from the oxide, all of which were replenished by oxidation.

Figure 1F compares the rates of C_2H_2 consumption during each reduction half-cycle and shows that when the Bi_2O_3 catalyst was not over-reduced during reduction, C_2H_2 consumption

rates are regenerable for 10 redox cycles. Additional experimental details of the reduction and oxidation half cycles can be found in Figs. S3 – S5, and an analogous experiment shown in Fig. S6 exposing Bi_2O_3 to only C_2H_4 as a reductant demonstrated the low reactivity of C_2H_4. The reproducibility of C_2H_2 combustion rates and full reoxidation of partially reduced Bi_2O_3 in repeated reduction/oxidation cycles were also verified in redox cycling experiments removing only 10% of O atoms in each reduction step, as shown in Figs. S7 and S8.

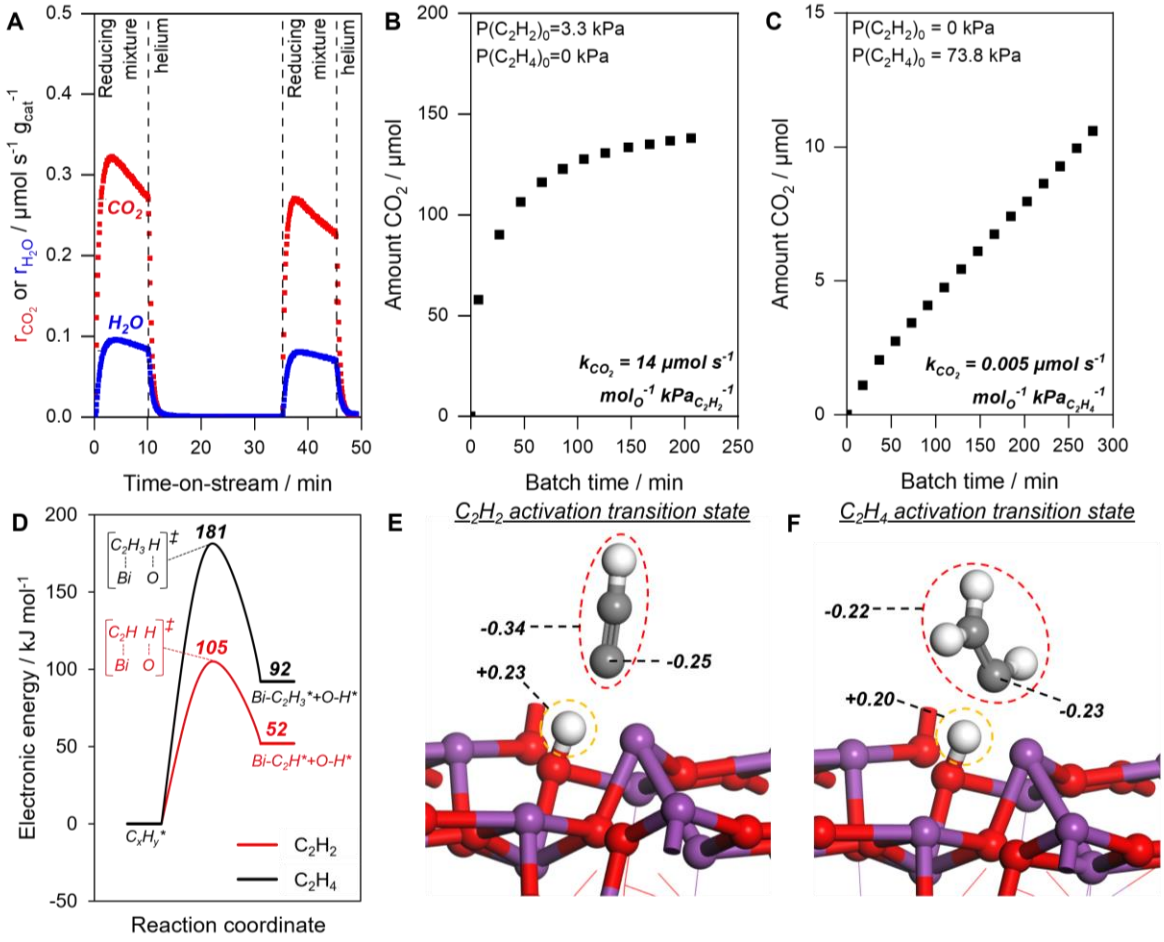

Fig. 2: Kinetics of C_2H_2 and C_2H_4 activation

(**A**) Dwell experiment showing combustion product evolution rates upon exposure of Bi_2O_3 to 1:10 C_2H_2:C_2H_4 before and after helium treatment. (**B** and **C**) The amount of CO_2 formed upon exposure of Bi_2O_3 to (**B**) C_2H_2 with no C_2H_4 and (**C**) C_2H_4 with no C_2H_2 in a recirculating batch reactor at 663 K. (**D**) The reaction energy diagram for C-H activation of C_2H_2 and C_2H_4 across a non-bonded Bi-O site, and the corresponding transitions states for (**E**) C_2H_2 and (**F**) C_2H_4. Transition state and product state energies are referenced to the physisorbed state. The numbers correspond to charges on C and H atoms and the C_xH_y fragment formed in the C-H scission transition state. Bi atoms are purple, O atoms are red, C atoms are gray, and H atoms are white. Flow reaction conditions for (**A**): m(Bi_2O_3)=1.0 g, T=673 K, P(C_2H_2)=2.2 kPa, P(C_2H_4)=21.5 kPa, P(CH_4)=2 kPa, P(Ar)=34.8 kPa, balance N_2, total flow rate=0.83 cm^3_{STP} s^{-1}. During the dwell step, the catalyst was exposed to He with a flow rate of 0.83 cm^3_{STP} s^{-1}. Batch reaction conditions for (**B**): m(Bi_2O_3)=258.4 mg, T=663 K, $P(C_2H_2)_0$=3.3 kPa, $P(C_2H_4)_0$=0 kPa, $P(CH_4)_0$=2.1 kPa, $P(He)_0$=51.4 kPa, balance N_2. Batch reaction conditions for (**C**): m(Bi_2O_3)=250.0 mg, T=663 K, $P(C_2H_2)_0$=0 kPa, $P(C_2H_4)_0$=73.8 kPa, $P(Ar)_0$=2.5 kPa, balance He.

Kinetic studies

Chemical looping reduction and oxidation cycles necessarily involve simultaneous kinetic rate processes involving lattice oxygen abstraction by the reacting hydrocarbon and physical rate processes involving diffusion of lattice oxygen to O-deficient regions on the surface of the catalyst. The surface coverage of lattice O atoms during redox half-cycles is dictated by the rate at which lattice O is supplied to surface O vacancies relative to the rate at which surface O is removed by combustion. We probed the contributions of lattice O diffusion to measured C_2H_2 combustion kinetics with a dwell experiment (*26*). During a stoichiometric reduction cycle, an inert dwell step was used to redistribute lattice O atoms throughout the oxide and alleviate any gradients in O concentration. Equal combustion product evolution rates before and after the inert dwell step indicated that the reductant contacted a surface with equal chemical potential of the oxidant before and after the inert dwell step, showing that lattice O diffusion is fast relative to surface lattice O abstraction by combustion. Fig. 2A depicts the results of a dwell experiment with an intervening helium purge lasting 25 min after removal of 7% of lattice O atoms in Bi_2O_3 in 1:10 C_2H_2:C_2H_4. The same H_2O and CO_2 evolution rates were observed before and after the inert dwell step, indicating that lattice O diffusion was faster than surface reaction kinetics; thus, measured C_2H_2 combustion kinetics were not convoluted by lattice O diffusion at 673 K. Equivalent rates of C_2H_2 consumption before and after the dwell step (Fig. S9) corroborated this result.

Dwell experiments were repeated at a range of viable process conditions. Bi_2O_3 combusted C_2H_2 at temperatures as low as 555 K (Fig. S10). Dwell experiments at 573 K (Fig. S11) and 773 K (Fig. S12) showed that lattice O diffusion constraints only became relevant at 773 K. At 673 K, however, comparison of the rate of lattice oxygen removal by C_2H_2 combustion and a lower bound on the rate of lattice oxygen diffusion revealed that lattice O diffusion rates exceeded rates of lattice O abstraction by C_2H_2 combustion by a factor > 12 (Figs. S13 and S14), indicating that C_2H_2 activation kinetics measured at 663 K were limited solely by rates of surface reactions. Further discussion on the barrier for O diffusion in Bi_2O_3 is provided in the text accompanying Fig. S15.

Rate constants for C_2H_2 and C_2H_4 combustion, free from O diffusion limitations, were assessed independently to determine if the lack in reactivity of C_2H_4 in the presence of C_2H_2 was caused by suppression or occupancy of C_2H_4 combustion sites by C_2H_2. During a batch reaction with C_2H_2 exposed to Bi_2O_3, C_2H_2 combusted to produce CO_2 (Fig. 2B); however, the rate at which CO_2 was produced decreased as the reaction progressed because of stoichiometric consumption of lattice O by C_2H_2, resulting in a lower C_2H_2 concentration and in fewer lattice O atoms remaining.

After accounting for the decrease in lattice O during stoichiometric reduction half cycles by normalizing combustion rates by remaining O atoms, we found that C_2H_2 combustion was first order in C_2H_2 pressure with a rate constant for CO_2 formation of 14 $\mu mol\ CO_2\ s^{-1}\ mol_O^{-1}\ kPa_{C_2H_2}^{-1}$ at 663 K and an apparent barrier for C_2H_2 activation of 113 ± 8 kJ mol^{-1} (see Fig. S16) in absence of heat and mass transport limitations (see Eqs. S7 – S19 and the accompanying discussion). The individual rate constant for C_2H_4 combustion assessed in the absence of C_2H_2 was 0.005 $\mu mol\ CO_2\ s^{-1}\ mol_O^{-1}\ kPa_{C_2H_4}^{-1}$ (Fig. 2C), 3000× smaller than the C_2H_2 combustion rate constant, demonstrating that occupancy of catalytically relevant sites for C_2H_4 combustion by C_2H_2 was not responsible for the high selectivity to C_2H_2 observed in molecular mixtures. The measured apparent barrier for C_2H_4 activation of 165 ± 20 kJ mol^{-1} (see Fig. S17) led to a difference between the experimentally measured apparent activation barriers for C_2H_2 and C_2H_4 of 52 kJ mol^{-1}, supporting the hypothesis that activation of C_2H_4 on bare Bi_2O_3 surfaces was energetically

disfavored relative to activation of C_2H_2. Enumeration of the rate constants for C_2H_2 activation with CO_2, C_2H_4, and H_2O cofeeds (see Figs. S18 – S20) showed that C_2H_2 activation rates were not inhibited by surface coverages of CO_2, C_2H_4 or H_2O. A rate constant for H_2 combustion on Bi_2O_3 at 663 K of 5.6 μmol H_2 s^{-1} mol_O^{-1} $kPa_{H_2}^{-1}$ (see Fig. S21) indicated that H_2 present in real feeds containing C_2H_2 and H_2 may combust to remove lattice O as well.

Theoretical studies

First-principles density functional theory (DFT) calculations were performed to examine the adsorption and activation of C_2H_2 and C_2H_4 over a model (010) surface of α-Bi_2O_3 and in turn elucidate the mechanistic origin for the high reactivity of C_2H_2 on Bi_2O_3. Previous calculations showed that the (010) surface is the lowest energy α-Bi_2O_3 surface (*27*) and provided valuable insights into the oxidation of hydrogen on Bi_2O_3 (*28*). Calculations herein showed that C_2H_2 as well as C_2H_4 weakly adsorbed on exposed Bi sites with an energy of -11 kJ mol^{-1}. The C-H bonds of C_2H_2 and C_2H_4 could be cleaved homolytically on O-O or Bi-Bi site pairs or heterolytically across Bi-O site pairs. Homolytic activation of C_2H_2 on undercoordinated Bi sites proceeded through metal insertion into the C-H bond, resulting in an activation energy of 148 kJ mol^{-1} (see Fig. S22 and S23 for details of the Bi_2O_3 models used for the periodic and cluster calculations, respectively, Fig. S24, A to C, for reactant, transition state, and product state geometries, and Table S1 for Bi-H and Bi-C bond lengths). Attempts to activate C_2H_2 across O-O site pairs instead converged to a heterolytic transition state across a Bi-O site.

In the heterolytic C-H activation of C_2H_2 and C_2H_4 over Bi-O site pairs, a proton and a negatively charged carbanion formed that were stabilized by the negative O^{2-} and positive Bi^{3+} charged surface sites, respectively. We investigated C-H activation of C_2H_2 and C_2H_4 on different active sites on the (010) α-Bi_2O_3 surface comprised of under-coordinated Bi_{3c}^{3+} and O^{2-} site pairs involving: (i) *bonded* Bi_{3c}-O and (ii) *non-bonded* Bi_{3c}-O site pairs, with respective Bi-O distances of 2.16 and 3.09 Å. Given the ensemble of Bi-O sites exposed on α-Bi_2O_3 surfaces during reaction, these sites represented limiting cases of sites with varying Bi-O distances across which C-H bonds may be activated.

The C-H activation barrier for C_2H_2 over the non-bonded Bi-O site was calculated to be slightly higher at 105 kJ mol^{-1} (see Fig. 2D and Fig. S24, D to F, and Table S1) than over the bonded Bi-O site at 87 kJ mol^{-1} (Fig. S24, G to I, and Table S1), with overall reaction energies of 52 and 77 kJ mol^{-1}, respectively. Activation of C_2H_4 on the non-bonded and bonded Bi-O sites proceeded with transition state energies of 181 kJ mol^{-1} (see Fig. 2D, Fig. S25, A to C, and Table S2) and 162 kJ mol^{-1} (see Fig. S25, D to F, and Table S2) and overall reaction energies of 92 and 140 kJ mol^{-1}, respectively.

The transition-state geometries that contribute to the differences in transition state energies on Bi-O sites are illustrated in Fig. S26. Although C-H activation of C_2H_2 and C_2H_4 over non-bonded Bi-O sites resulted in transition-state energies that were 18 and 19 kJ mol^{-1} higher, respectively, than on bonded Bi-O sites, these limiting cases resulted in C-H activation barriers for C_2H_2 that were 75 kJ mol^{-1} and 76 kJ mol^{-1} more favorable than C_2H_4, respectively, as illustrated in Fig. 2D over non-bonded Bi-O sites. Chemical looping reduction cycles may lead to a distribution of sites that contribute unequally to measured rates of hydrocarbon activation, but we do not expect that evolution of the ensemble of exposed sites would lead to changes in selectivity to C_2H_2 activation. Experimentally, no changes in the >99% selectivity to C_2H_2 activation were observed in redox-cycling experiments during removal of up to 20% of total lattice O atoms in Bi_2O_3 (see Fig. 1D).

The results in Fig. 2, E and F, provide additional evidence for the heterolytic nature of the activation steps for C_2H_2 and C_2H_4, respectively, by showing the charges on the H atoms and C_xH_y fragments in the transition state (enumerated by cluster calculations). The hydrogen atoms formed upon the C-H scission of both molecules become protonic with positive atomic charges of +0.23 e and +0.20 e for C_2H_2 and C_2H_4 activation, respectively. The electrons in the C-H bond localized in the residual hydrocarbon fragment, yielding anionic CH≡C(-) and CH_2=CH(-) fragments with overall charges of -0.34 e and -0.22 e, respectively.

The preferential stabilization of the C_2H_2 activation transition state appeared to be the result of C_2H_2 tending to cleave heterolytically with energy given by the deprotonation energy, DPE, rather than homolytically with energy given by the bond dissociation energy, BDE. Although C_2H_2 is more difficult to activate homolytically in the gas phase than C_2H_4 (BDE = 558 kJ mol^{-1} vs. 464 kJ mol^{-1} (*29*)), heterolytic dissociation of the C-H bond in C_2H_2 is 125 kJ mol^{-1} more favorable than C_2H_4 (DPE = 1580 kJ mol^{-1} vs. 1705 kJ mol^{-1} (*30*)). The higher acidity of the C-H bond in C_2H_2 results from the stronger stabilization of the resulting CH≡C(-) anion, which has more s character (50%) than the resulting CH_2=CH(-) anion (33.3%), and thus allows the excess electron density to lie closer to the nuclei.

Despite differences in transition state lateness on bonded and non-bonded Bi-O sites, the C-H activation transition states for both C_2H_2 and C_2H_4 were late as assessed by the O-H and Bi-C bond lengths relative to the reactant and product states (see Tables S1 and S2) and involved the near complete dissociation of the C-H bonds. The transition-state energies reflect, in part, contributions from the DPEs of C_2H_2 and C_2H_4, resulting in a lower barrier for C_2H_2 activation on Bi-O than C_2H_4. Based on the hypothesis that rates of hydrocarbon combustion initiated by rate-determining heterolytic C-H scission will scale with molecular DPEs, we probed the viability of extrapolating this concept to other hydrocarbon mixtures by examining selective combustion of 1,3-butadiene in propane on Bi_2O_3. 1,3-butadiene has a DPE (1672 kJ mol^{-1} (*30*)) which is 83 kJ mol^{-1} lower than that of propane (1755 kJ mol^{-1} (*30*)) but a BDE (445 kJ mol^{-1} (*31*)) which is 34 kJ mol^{-1} higher than propane (411 kJ mol^{-1} (*29*)).

At 773 K, Bi_2O_3 selectively combusted 1,3-butadiene with > 98% selectivity (see Fig. S27), consistent with selective combustion of the more acidic C-H bonds in 1,3-butadiene in mixtures with propane. Further discussion on the use of Bi_2O_3 as a combustion catalyst for 1-butene and 1,3-butadiene is provided in the discussion accompanying Figs. S28 and S29. Low BDE values for molecules which may form stable radical species upon C-H scission may enable alternate homolytic reactivity pathways which limit the use of DPE as a sole molecular descriptor for catalytic cycles initiated by non-heterolytic C-H activation. These homolytic C-H activation routes are inaccessible for activation of C_2H_2 or C_2H_4 on Bi_2O_3 due to their high BDE values of 558 kJ mol^{-1} and 464 kJ mol^{-1}, respectively (*29*).

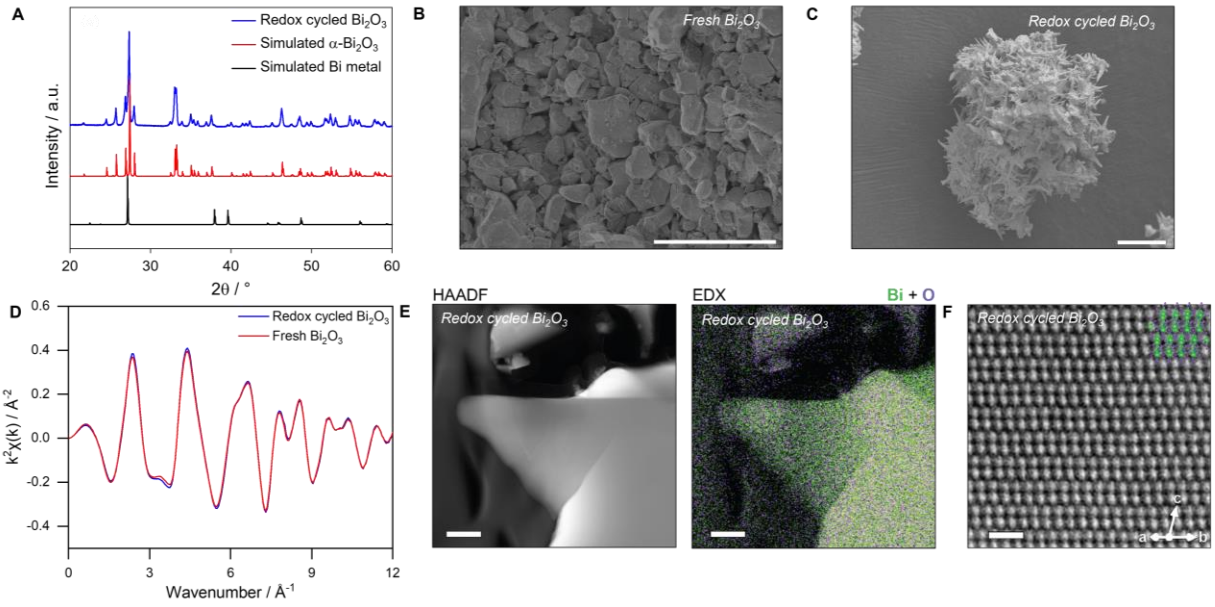

Fig. 3: Characterization of fresh and redox cycled Bi_2O_3
(**A**) X-ray diffraction (XRD) patterns of redox cycled Bi_2O_3, referenced against XRD patterns of α-Bi_2O_3 (*32*) and Bi metal (*33*) simulated from their corresponding crystallographic information files. (**B-C**) Scanning electron microscopy (SEM) images of the Bi_2O_3 catalyst (**B**) prior to (scale bar is 20 μm) and (**C**) after 10 successive reduction/oxidation cycles (scale bar is 100 μm). (**D**) Bi L_3-edge x-ray absorption spectroscopy (XAS) k^2-weighted χ(k) oscillations of fresh Bi_2O_3 and redox cycled Bi_2O_3. (**E**) Low-magnification high-angle annular dark-field scanning transmission electron microscopy (HAADF-STEM) image of a needle-like feature on the redox-cycled Bi_2O_3 with STEM-energy-dispersive x-ray (EDX) elemental map. The map is overlayed over the HAADF image showing the distribution of Bi and O everywhere in the structure. Scale bars are 200 nm. (**F**) Atomic-resolution HAADF-STEM image from the redox-cycled sample showing the crystal structure of Bi_2O_3 viewed along [110] direction. The image was low-pass filtered for clarity. The atomic model of the α-Bi_2O_3 structure is overlayed to show the match. The scale bar is 1 nm.

Surface characterization

The DFT results are predicated on the persistence of α-Bi_2O_3 surfaces during reaction conditions and after repeated redox cycling, especially considering the redistribution of lattice O consequent from the removal and full replenishment of 20 to 30% of O atoms during redox cycles. We used a suite of characterization techniques to develop a better understanding of the catalytically relevant surfaces after partial reduction by C_2H_2 combustion and the effects redox cycling has on phase, particle morphology, and local Bi coordination. Temperature-programmed oxidation (TPO) of a partially reduced Bi_2O_3 sample was used to assess the absence or presence of coke on particle surfaces after partial reduction by C_2H_2 combustion (Fig. S30). After reduction of Bi_2O_3 to θ_O = 0.84, 7.1 μmol C g_{cat}^{-1} were removed as CO_2 during the subsequent TPO, relative to the 430 μmol C g_{cat}^{-1} reacted during the preceding reduction step, indicating minimal coke formation during reduction half cycles.

X-ray diffraction (XRD) was used to evaluate the presence of other Bi_2O_3 polymorphs or crystalline Bi metal domains in fresh, partially reduced, and redox cycled Bi_2O_3 samples. In-situ

XRD diffraction patterns of fresh Bi_2O_3 heated to 773 K in flowing air (see Fig. S31) illustrated that no other polymorphic Bi_2O_3 phases form up to 773 K; all shifts in peak positions with increasing temperature could be attributed solely to anisotropic lattice expansion (see Fig. S32), as has been observed by Yashima et al. (*34*). A series of partially reduced Bi_2O_3 samples were prepared by removal of 8%, 17%, and 28% of O atoms by C_2H_2 combustion at 673 K followed by cooling to ambient conditions in argon. The XRD patterns of partially reduced Bi_2O_3 samples exhibited peaks for α-Bi_2O_3 and Bi metal, which increased monotonically with extent of reduction (see Fig. S33). The discussion accompanying Figs. S33 - S41 provides further details regarding the phase and composition of partially reduced Bi_2O_3 samples. Heating of a partially reduced Bi_2O_3 sample above the melting point of Bi metal (544 K) resulted in the disappearance of diffraction peaks for Bi metal (see Fig. S34). Fig. 3A compares the XRD patterns of the redox-cycled Bi_2O_3 sample to simulated XRD patterns for α-Bi_2O_3 and Bi metal. After cooling to ambient conditions following full reoxidation by O_2, the redox-cycled Bi_2O_3 catalyst exhibited high crystallinity and was composed of the α polymorph of Bi_2O_3, with only trace peaks from Bi metal and no other Bi_2O_3 polymorphs detected, illustrating that reoxidation steps in redox cycling experiments can fully regenerate partially reduced Bi_2O_3 particles with minimal changes in catalytic activity (see Fig. 1C and 1F).

Despite the phase purity of redox-cycled Bi_2O_3 observed by XRD, the textural properties of Bi_2O_3 particles were altered by redox cycling; Figs. 3B and 3C, compare SEM images of fresh and redox-cycled Bi_2O_3 particles, respectively. The fresh catalyst exposed large, flat facets, whereas the redox-cycled Bi_2O_3 sample adopted a surface with needle-like structures. These textured surfaces were observed on all redox cycled particles; additional SEM images are shown in Fig. S42. These changes in morphological properties were also observed on the Bi_2O_3 sample subjected to five successive redox cycles in which fewer than 10% of O atoms were removed from the oxide during each reduction step (see Fig. S43).

We determined the phase and stoichiometry of these needle-like structures relative to fresh Bi_2O_3 samples using ex-situ XAS and x-ray photoelectron spectroscopy (XPS) to probe changes in local Bi coordination and oxidation state, EDX to assess the Bi:O stoichiometry in these needles (specifically to address if these features were composed of Bi metal that was unable to be reoxidized), and HAADF-STEM to determine differences in the facets exposed on the needle-like structures. Comparisons of the Bi 4f and O 1s XPS spectra of fresh and redox-cycled Bi_2O_3 samples (see Figs. S44 and S45) indicated that all near-surface Bi cations exhibited the +3 oxidation state with only minor differences in the O 1s spectra. Figure 3D shows negligible differences in k^2-weighted momentum (k)-space oscillations for fresh and redox-cycled Bi_2O_3 (see Fig. S46 for comparisons of the normalized absorbances of the Bi-L_{III} edge and the magnitude and imaginary components of Fourier-transformed EXAFS for the fresh and redox cycled Bi_2O_3 samples). These results qualitatively indicated that the redox-cycled Bi_2O_3 sample contains Bi cations with the same local environment as fresh α-Bi_2O_3 samples.

Extended x-ray absorption fine structure (EXAFS) modeling of the structures of fresh and redox-cycled Bi_2O_3 samples (shown in Fig. S47, with fitting parameters for the fresh and redox-cycled samples shown in Tables S6 and S7, respectively) indicated that the effective bond lengths of the three Bi-O bonds and one Bi-Bi bond included in the fits, bond length disorder (σ^2) parameters, and amplitude reduction factors were the same when we used fitting procedures that fixed the coordination numbers of each of the paths included. These EXAFS fitting parameters reflected contributions of Bi particles throughout the bulk of the oxide particles and were not specific to Bi atoms on the catalytically relevant surfaces.

We used STEM to probe the phase and stoichiometry of the needle-like structures directly without convolution by Bi atoms subsiding in the bulk of Bi_2O_3 particles. Figure 3E shows a set of HAADF-STEM images of the dendritic growth on redox-cycled Bi_2O_3 along with STEM-EDX compositional maps. The needle-like spikes were composed of Bi and O, with no apparent phase segregation or formation of Bi metal cores (see also Fig. S48). The even distribution of Bi and O seen in STEM-EDX maps was consistent with the maps obtained from fresh Bi_2O_3 particles (see Fig. S49). The crystal structure of the needle-like structures was further corroborated by the observation of α-Bi_2O_3, shown in Fig. 3F (for images obtained from fresh Bi_2O_3 samples, see Fig. S49). These observations further support formation of α-Bi_2O_3 in the needle-like structures during redox-cycling.

Discussion

We demonstrate selective chemical looping C_2H_2 combustion as an alternative to C_2H_2 semi-hydrogenation to purify C_2H_4-rich gas streams with an inexpensive bulk Bi_2O_3 catalyst that does not require elevated pressures, is tolerant to CO_2, H_2O, and C_2H_4, and retains reactivity for C_2H_2 combustion with high selectivity across multiple redox cycles after full reoxidation. The rate constant for C_2H_2 combustion was ~ 3000× the rate constant for C_2H_4 combustion, consistent with the ~ 75 kJ mol^{-1} difference in DFT-derived transition state energies on Bi-O sites. DFT results indicated that the high selectivity of Bi_2O_3 to C_2H_2 combustion in C_2H_4 mixtures could be attributed to the formation of heterolytic C-H activation transition states on Bi-O sites of α-Bi_2O_3 which favored the activation of molecules with more acidic C-H bonds, such as C_2H_2. After redox cycling, the catalyst exhibited no changes in local Bi coordination and only trace amounts of Bi metal. The significant changes in particle morphology observed after redox cycling are ascribed to recrystallization of the O-deficient reduced state upon exposure to O_2 to regenerate crystalline α-Bi_2O_3 domains. This application of selective hydrocarbon combustion has the potential to circumvent conventional separation methods for the removal of molecules with more acidic C-H bonds, such as alkynes, from multi-component hydrocarbon mixtures.

References and Notes

(1) Trotuş, I.-T.; Zimmermann, T.; Schüth, F. Catalytic Reactions of Acetylene: A Feedstock for the Chemical Industry Revisited. *Chem. Rev.* **2014**, *114* (3), 1761–1782. https://doi.org/10.1021/cr400357r.

(2) Borodziński, A.; Bond, G. C. Selective Hydrogenation of Ethyne in Ethene-Rich Streams on Palladium Catalysts. Part 1. Effect of Changes to the Catalyst During Reaction. *Catal. Rev.* **2006**, *48* (2), 91–144. https://doi.org/10.1080/01614940500364909.

(3) Borodziński, A.; Bond, G. C. Selective Hydrogenation of Ethyne in Ethene-Rich Streams on Palladium Catalysts, Part 2: Steady-State Kinetics and Effects of Palladium Particle Size, Carbon Monoxide, and Promoters. *Catal. Rev.* **2008**, *50* (3), 379–469. https://doi.org/10.1080/01614940802142102.

(4) Pässler, P.; Hefner, W.; Buckl, K.; Meinass, H.; Meiswinkel, A.; Wernicke, H.-J.; Ebersberg, G.; Müller, R.; Bässler, J.; Behringer, H.; Mayer, D. Acetylene. In *Ullmann's Encyclopedia of Industrial Chemistry*; Wiley-VCH Verlag GmbH & Co. KGaA, Ed.; Wiley-VCH Verlag GmbH & Co. KGaA: Weinheim, Germany, **2011**; p a01_097.pub4. https://doi.org/10.1002/14356007.a01_097.pub4.

(5) Seifzadeh Haghighi, S.; Rahimpour, M. R.; Raeissi, S.; Dehghani, O. Investigation of Ethylene Production in Naphtha Thermal Cracking Plant in Presence of Steam and Carbon Dioxide. *Chem. Eng. J.* **2013**, *228*, 1158–1167. https://doi.org/10.1016/j.cej.2013.05.048.

(6) Zhao, X.; Chang, Y.; Chen, W.-J.; Wu, Q.; Pan, X.; Chen, K.; Weng, B. Recent Progress in Pd-Based Nanocatalysts for Selective Hydrogenation. *ACS Omega* **2022**, *7* (1), 17–31. https://doi.org/10.1021/acsomega.1c06244.

(7) Khan, N. A.; Shaikhutdinov, S.; Freund, H.-J. Acetylene and Ethylene Hydrogenation on Alumina Supported Pd-Ag Model Catalysts. *Catal. Lett.* **2006**, *108* (3), 159–164. https://doi.org/10.1007/s10562-006-0041-y.

(8) Sheth, P. A.; Neurock, M.; Smith, C. M. First-Principles Analysis of the Effects of Alloying Pd with Ag for the Catalytic Hydrogenation of Acetylene−Ethylene Mixtures. *J. Phys. Chem. B* **2005**, *109* (25), 12449–12466. https://doi.org/10.1021/jp050194a.

(9) Pei, G. X.; Liu, X. Y.; Wang, A.; Lee, A. F.; Isaacs, M. A.; Li, L.; Pan, X.; Yang, X.; Wang, X.; Tai, Z.; Wilson, K.; Zhang, T. Ag Alloyed Pd Single-Atom Catalysts for Efficient Selective Hydrogenation of Acetylene to Ethylene in Excess Ethylene. *ACS Catal.* **2015**, *5* (6), 3717–3725. https://doi.org/10.1021/acscatal.5b00700.

(10) Studt, F.; Abild-Pedersen, F.; Bligaard, T.; Sørensen, R. Z.; Christensen, C. H.; Nørskov, J. K. On the Role of Surface Modifications of Palladium Catalysts in the Selective Hydrogenation of Acetylene. *Angew. Chem. Int. Ed.* **2008**, *47* (48), 9299–9302. https://doi.org/10.1002/anie.200802844.

(11) Ota, A.; Armbrüster, M.; Behrens, M.; Rosenthal, D.; Friedrich, M.; Kasatkin, I.; Girgsdies, F.; Zhang, W.; Wagner, R.; Schlögl, R. Intermetallic Compound Pd_2Ga as a Selective Catalyst for the Semi-Hydrogenation of Acetylene: From Model to High Performance Systems. *J. Phys. Chem. C* **2011**, *115* (4), 1368–1374. https://doi.org/10.1021/jp109226r.

(12) Huang, F.; Peng, M.; Chen, Y.; Cai, X.; Qin, X.; Wang, N.; Xiao, D.; Jin, L.; Wang, G.; Wen, X.-D.; Liu, H.; Ma, D. Low-Temperature Acetylene Semi-Hydrogenation over the Pd_1–Cu_1 Dual-Atom Catalyst. *J. Am. Chem. Soc.* **2022**, *144* (40), 18485–18493. https://doi.org/10.1021/jacs.2c07208.

(13) Kyriakou, G.; Boucher, M. B.; Jewell, A. D.; Lewis, E. A.; Lawton, T. J.; Baber, A. E.; Tierney, H. L.; Flytzani-Stephanopoulos, M.; Sykes, E. C. H. Isolated Metal Atom Geometries as a Strategy for Selective Heterogeneous Hydrogenations. *Science* **2012**, *335* (6073), 1209–1212. https://doi.org/10.1126/science.1215864.

(14) Westbrook, C. K.; Dryer, F. L. Chemical Kinetic Modeling of Hydrocarbon Combustion. *Prog. Energy Combust. Sci.* **1984**, *10* (1), 1–57. https://doi.org/10.1016/0360-1285(84)90118-7.

(15) Hucknall, D. *Chemistry of Hydrocarbon Combustion*; Springer Science & Business Media, 2012.

(16) Hinuma, Y.; Toyao, T.; Kamachi, T.; Maeno, Z.; Takakusagi, S.; Furukawa, S.; Takigawa, I.; Shimizu, K. Density Functional Theory Calculations of Oxygen Vacancy Formation and Subsequent Molecular Adsorption on Oxide Surfaces. *J. Phys. Chem. C* **2018**, *122* (51), 29435–29444.

(17) Boyapati, S.; Wachsman, E. D.; Jiang, N. Effect of Oxygen Sublattice Ordering on Interstitial Transport Mechanism and Conductivity Activation Energies in Phase-Stabilized Cubic Bismuth Oxides. *Solid State Ionics* **2001**, *140* (1), 149–160. https://doi.org/10.1016/S0167-2738(01)00698-1.

(18) Sammes, N. M.; Tompsett, G. A.; Näfe, H.; Aldinger, F. Bismuth Based Oxide Electrolytes— Structure and Ionic Conductivity. *Journal of the European Ceramic Society* **1999**, *19* (10), 1801–1826. https://doi.org/10.1016/S0955-2219(99)00009-6.

(19) Azad, A. M.; Larose, S.; Akbar, S. A. Bismuth Oxide-Based Solid Electrolytes for Fuel Cells. *Journal of Materials Science* **1994**, *29* (16), 4135–4151.
(20) Hussain, M.; Batool, S. S.; Imran, Z.; Ahmad, M.; Rasool, K.; Rafiq, M. A.; Hasan, M. M. Oxygen Sensing and Transport Properties of Nanofibers of Silica, Bismuth Doped Silica and Bismuth Silicate Prepared via Electrospinning. Sensors and Actuators B: Chemical **2014**, 192, 429–438.
(21) Cabot, A.; Marsal, A.; Arbiol, J.; Morante, J. R. Bi_2O_3 as a Selective Sensing Material for NO Detection. *Sensors and Actuators B: Chemical* **2004**, *99* (1), 74–89.
(22) Tsikoyiannis, J. G.; Stern, D. L.; Grasselli, R. K. Metal Oxides As Selective Hydrogen Combustion (SHC) Catalysts and Their Potential in Light Paraffin Dehydrogenation. *Journal of Catalysis* **1999**, *184* (1), 77–86. https://doi.org/10.1006/jcat.1998.2363.
(23) Grasselli, R. K.; Stern, D. L.; Tsikoyiannis, J. G. Catalytic Dehydrogenation (DH) of Light Paraffins Combined with Selective Hydrogen Combustion (SHC): I. DH→SHC→DH Catalysts in Series (Co-Fed Process Mode). *Applied Catalysis A: General* **1999**, *189* (1), 1–8. https://doi.org/10.1016/S0926-860X(99)00224-0.
(24) Grasselli, R. K.; Stern, D. L.; Tsikoyiannis, J. G. Catalytic Dehydrogenation (DH) of Light Paraffins Combined with Selective Hydrogen Combustion (SHC): II. DH+SHC Catalysts Physically Mixed (Redox Process Mode). *Applied Catalysis A: General* **1999**, *189* (1), 9–14. https://doi.org/10.1016/S0926-860X(99)00195-7.
(25) Låte, L.; Thelin, W.; Blekkan, E. A. Selective Combustion of Hydrogen in the Presence of Hydrocarbons: Part 2. Metal Oxide Based Catalysts. *Applied Catalysis A: General* **2004**, *262* (1), 63–68. https://doi.org/10.1016/j.apcata.2003.11.018.
(26) Hwang, A.; Wu, J.; Getsoian, A. "Bean"; Iglesia, E. Kinetic Relevance of Surface Reactions and Lattice Diffusion in the Dynamics of Ce–Zr Oxides Reduction–Oxidation Cycles. *J. Phys. Chem. C* **2023**, *127* (6), 2936–2952. https://doi.org/10.1021/acs.jpcc.2c08117.
(27) Lei, Y.-H.; Chen, Z.-X. Density Functional Study of the Stability of Various α-Bi_2O_3 Surfaces. *J. Chem. Phys.* **2013**, *138* (5), 054703. https://doi.org/10.1063/1.4788667.
(28) Jacob, M.; Nguyen, H.; Neurock, M.; Bhan, A. Kinetics of Redox Half-Cycles on Bi_2O_3 for the Selective Catalytic Combustion of Hydrogen. *ACS Catal.* **2024**, *14* (7), 4568–4580. https://doi.org/10.1021/acscatal.3c05585.
(29) *CRC Handbook of Chemistry and Physics*, 95th ed.; Haynes, W. M., Ed.; CRC Press: Boca Raton, 2014. https://doi.org/10.1201/b17118.
(30) Linstrom, P. NIST Chemistry WebBook, NIST Standard Reference Database 69, 1997. https://doi.org/10.18434/T4D303.
(31) St. John, P. C.; Guan, Y.; Kim, Y.; Kim, S.; Paton, R. S. Prediction of Organic Homolytic Bond Dissociation Enthalpies at near Chemical Accuracy with Sub-Second Computational Cost. *Nat. Commun.* **2020**, *11* (1), 2328. https://doi.org/10.1038/s41467-020-16201-z.
(32) Ivanov, S. A.; Tellgren, R.; Rundlo¨f, H.; Orlov, V. G. Structural Studies of α-Bi_2O_3 by Neutron Powder Diffraction. *Powder Diffr.* **2001**, *16* (4), 227–230. https://doi.org/10.1154/1.1401200.
(33) Wyckoff, R. W. G. *Crystal Structures - Volume 1*, 2nd ed.; Interscience Publishers: New York, 1963.
(34) Yashima, M.; Ishimura, D.; Ohoyama, K. Temperature Dependence of Lattice Parameters and Anisotropic Thermal Expansion of Bismuth Oxide. *J. Am. Ceram. Soc.* **2005**, *88* (8), 2332–2335. https://doi.org/10.1111/j.1551-2916.2005.00432.x.
(35) Brunauer, S.; Emmett, P. H.; Teller, E. Adsorption of Gases in Multimolecular Layers. *J. Am. Chem. Soc.* **1938**, *60* (2), 309–319. https://doi.org/10.1021/ja01269a023.

(36) Ravel, B.; Newville, M. ATHENA, ARTEMIS, HEPHAESTUS: Data Analysis for X-Ray Absorption Spectroscopy Using IFEFFIT. *J. Synchrotron Radiat.* **2005**, *12* (4), 537–541. https://doi.org/10.1107/S0909049505012719.

(37) Kresse, G.; Hafner, J. Ab Initio Molecular Dynamics for Liquid Metals. *Phys. Rev. B* **1993**, *47* (1), 558–561. https://doi.org/10.1103/PhysRevB.47.558.

(38) Kresse, G.; Hafner, J. Ab Initio Molecular-Dynamics Simulation of the Liquid-Metal--Amorphous-Semiconductor Transition in Germanium. *Phys. Rev. B* **1994**, *49* (20), 14251–14269. https://doi.org/10.1103/PhysRevB.49.14251.

(39) Kresse, G.; Furthmüller, J. Efficiency of Ab-Initio Total Energy Calculations for Metals and Semiconductors Using a Plane-Wave Basis Set. *Comput. Mater. Sci.* **1996**, *6* (1), 15–50. https://doi.org/10.1016/0927-0256(96)00008-0.

(40) Kresse, G.; Furthmüller, J. Efficient Iterative Schemes for Ab Initio Total-Energy Calculations Using a Plane-Wave Basis Set. *Phys. Rev. B* **1996**, *54* (16), 11169–11186. https://doi.org/10.1103/PhysRevB.54.11169.

(41) Blöchl, P. E. Projector Augmented-Wave Method. *Phys. Rev. B* **1994**, *50* (24), 17953–17979. https://doi.org/10.1103/PhysRevB.50.17953.

(42) Kresse, G.; Joubert, D. From Ultrasoft Pseudopotentials to the Projector Augmented-Wave Method. *Phys. Rev. B* **1999**, *59* (3), 1758–1775. https://doi.org/10.1103/PhysRevB.59.1758.

(43) Perdew, J. P.; Burke, K.; Ernzerhof, M. Generalized Gradient Approximation Made Simple. *Phys. Rev. Lett.* **1996**, *77* (18), 3865–3868. https://doi.org/10.1103/PhysRevLett.77.3865.

(44) Henkelman, G.; Jónsson, H. Improved Tangent Estimate in the Nudged Elastic Band Method for Finding Minimum Energy Paths and Saddle Points. *J. Chem. Phys.* **2000**, *113* (22), 9978–9985. https://doi.org/10.1063/1.1323224.

(45) Henkelman, G.; Jónsson, H. A Dimer Method for Finding Saddle Points on High Dimensional Potential Surfaces Using Only First Derivatives. *J. Chem. Phys.* **1999**, *111* (15), 7010–7022. https://doi.org/10.1063/1.480097.

(46) Marenich, A. V.; Jerome, S. V.; Cramer, C. J.; Truhlar, D. G. Charge Model 5: An Extension of Hirshfeld Population Analysis for the Accurate Description of Molecular Interactions in Gaseous and Condensed Phases. *J. Chem. Theory Comput.* **2012**, *8* (2), 527–541. https://doi.org/10.1021/ct200866d.

(47) Gaussian 16, Revision C.01, M. J. Frisch, G. W. Trucks, H. B. Schlegel, G. E. Scuseria, M. A. Robb, J. R. Cheeseman, G. Scalmani, V. Barone, G. A. Petersson, H. Nakatsuji, X. Li, M. Caricato, A. V. Marenich, J. Bloino, B. G. Janesko, R. Gomperts, B. Mennucci, H. P. Hratchian, J. V. Ortiz, A. F. Izmaylov, J. L. Sonnenberg, D. Williams-Young, F. Ding, F. Lipparini, F. Egidi, J. Goings, B. Peng, A. Petrone, T. Henderson, D. Ranasinghe, V. G. Zakrzewski, J. Gao, N. Rega, G. Zheng, W. Liang, M. Hada, M. Ehara, K. Toyota, R. Fukuda, J. Hasegawa, M. Ishida, T. Nakajima, Y. Honda, O. Kitao, H. Nakai, T. Vreven, K. Throssell, J. A. Montgomery, Jr., J. E. Peralta, F. Ogliaro, M. J. Bearpark, J. J. Heyd, E. N. Brothers, K. N. Kudin, V. N. Staroverov, T. A. Keith, R. Kobayashi, J. Normand, K. Raghavachari, A. P. Rendell, J. C. Burant, S. S. Iyengar, J. Tomasi, M. Cossi, J. M. Millam, M. Klene, C. Adamo, R. Cammi, J. W. Ochterski, R. L. Martin, K. Morokuma, O. Farkas, J. B. Foresman, and D. J. Fox, Gaussian, Inc., Wallingford CT, **2016**.

(48) Zhao, Y.; Truhlar, D. G. A New Local Density Functional for Main-Group Thermochemistry, Transition Metal Bonding, Thermochemical Kinetics, and Noncovalent Interactions. *J. Chem. Phys.* **2006**, *125* (19), 194101. https://doi.org/10.1063/1.2370993.

(49) Dolg, M.; Wedig, U.; Stoll, H.; Preuss, H. Energy-adjusted Ab Initio Pseudopotentials for the First Row Transition Elements. *J. Chem. Phys.* **1987**, *86* (2), 866–872. https://doi.org/10.1063/1.452288.

(50) Dunning, T. H., Jr. Gaussian Basis Sets for Use in Correlated Molecular Calculations. I. The Atoms Boron through Neon and Hydrogen. *J. Chem. Phys.* **1989**, *90* (2), 1007–1023. https://doi.org/10.1063/1.456153.

(51) Jain, A.; Ong, S. P.; Hautier, G.; Chen, W.; Richards, W. D.; Dacek, S.; Cholia, S.; Gunter, D.; Skinner, D.; Ceder, G.; Persson, K. A. Commentary: The Materials Project: A Materials Genome Approach to Accelerating Materials Innovation. *APL Mater.* **2013**, *1* (1), 011002. https://doi.org/10.1063/1.4812323.

(52) Froment, G.F.; Bischoff, K.B.; De Wilde, J. (**2011**) Chemical Reactor Analysis and Design. 3rd Edition, John Wiley & Sons, Inc., New York.

(53) Lemmon, E. W.; Jacobsen, R. T. Viscosity and Thermal Conductivity Equations for Nitrogen, Oxygen, Argon, and Air. *International Journal of Thermophysics* **2004**, *25* (1), 21–69.

(54) Higgins, B.; Binous, H **2013**, Binary Diffusion Coefficients for Gases, Wolfram Demonstrations Project. demonstrations.wolfram.com/BinaryDiffusionCoefficientsForGases/

(55) "JADE Pro ." 2023. Livermore, CA, USA.: MDI Materials Data.

(56) Dharmadhikari, V. S.; Sainkar, S. R.; Badrinarayan, S.; Goswami, A. Characterisation of Thin Films of Bismuth Oxide by X-Ray Photoelectron Spectroscopy. *Journal of Electron Spectroscopy and Related Phenomena* **1982**, *25* (2), 181–189.

(57) Meng, L.; Xu, W.; Zhang, Q.; Yang, T.; Shi, S. Study of Nanostructural Bismuth Oxide Films Prepared by Radio Frequency Reactive Magnetron Sputtering. *Applied Surface Science* **2019**, *472*, 165–171.

Acknowledgments:

Funding: This work was primarily supported by the U.S. Department of Energy Office of Basic Energy Sciences under Award DE-SC0025321 and partially under Award DE-SC0024710. Parts of this work were carried out in the Characterization Facility, University of Minnesota, which receives partial support from the NSF through the MRSEC (Award number DMR-2011401) and the NNCI (Award number ECSS-2025124) programs. HN and MN gratefully acknowledge the Minnesota Supercomputing Institute (MSI) at the University of Minnesota for computational resources. Use of the Stanford Synchrotron Radiation Lightsource, SLAC National Accelerator Laboratory, is supported by the U.S. Department of Energy, Office of Science, Office of Basic Energy Sciences under Contract No. DE-AC02-76SF00515. Co-ACCESS, part of the SUNCAT Center for Interface Science and Catalysis, is supported by the U.S. Department of Energy, Office of Basic Energy Sciences, Chemical Sciences, Geosciences and Biosciences Division.

Author contributions:

Conceptualization: MJ and AB

Methodology: MJ, HN, RR, JG, JH, JP, and AH.

Investigation: MJ, HN, RR and JG

Visualization: MJ, HN, and RR

Funding acquisition: AB, SRB, KAM, and MN

Project administration: AB

Supervision: JG, KAM, SRB, MN and AB

Writing – original draft: MJ

Writing – review & editing: all authors

Competing interests: MJ and AB are listed as inventors on a provisional patent that has been filed for this work (U.S. nonprovisional patent application No. 18/743,688). The authors declare no competing interests.

Data and materials availability: All data are available in the manuscript or in the supplementary materials.

Supplementary Materials

Materials and Methods

Supplementary Text

Figs. S1 to S49

Tables S1 to S7

References (*35*-*57*)

Science
AAAS

Supplementary Materials for

Selective chemical looping combustion of acetylene in ethylene-rich streams

Matthew Jacob, Huy Nguyen, Rishi Raj, Javier Garcia-Barriocanal, Jiyun Hong, Jorge E. Perez-Aguilar, Adam S. Hoffman, K. Andre Mkhoyan, Simon R. Bare, Matt Neurock, Aditya Bhan*

*: Corresponding author: abhan@umn.edu

The PDF file includes:

Materials and Methods
Supplementary Text
Figs. S1 to S49
Tables S1 to S7
References

Materials and Methods

Catalyst preparation and testing

Bulk Bi_2O_3 (Sigma-Aldrich, 99.999%) was pressed, crushed, and sieved to yield particles with diameters between 177 μm and 400 μm for catalytic testing. Pelletized Bi_2O_3 was loaded in a quartz reactor (Technical Glass Products, I.D. = 10.5 mm, O.D. = 12.75 mm) and supported between two quartz wool plugs, and quartz rods (O.D. = 9 mm) were placed upstream and downstream of the catalyst to minimize reactor dead volume and, consequently, homogeneous reactions. An Inconel cylinder surrounding the quartz reactor facilitated heat transfer from a surrounding furnace (National Element, FA-120). Reaction temperature was monitored and controlled by two K-type thermocouples (Omega) diametrically contacting the quartz reactor at the location of the catalyst. Reaction lines were heated with resistive heating tape and an oven to maintain gas temperatures above 383 K to prevent condensation of gaseous species. Gas composition was monitored with a gas-chromatograph (Agilent 8890 GC) equipped with a Plot-Q column (30m length × 0.32 mm inner diameter, 20 μm film thickness) to separate permanent gases and hydrocarbons with cryogenic temperatures and a thermal conductivity detector (TCD) placed in series before a flame-ionization detector (FID) for hydrocarbon detection. Helium was used as a carrier gas. CO_x species were converted to CH_4 in the FID with a methanizer (Activated Research, Jetanizer^{TM}) to enable accurate quantification of CO in the FID unconvoluted by coelution with argon.

Gas (Ar (Airgas, UHP), CH_4 (Airgas, 99.999%), He (Airgas, 99.9995%), 5% C_2H_2/N_2 (Airgas), C_2H_4 (Matheson, 99.999%)) flows were metered to the catalytic testing unit with MKS mass flow controllers (GM50A). Prior to reaction, the catalyst was heated to the reaction temperature at 0.083 K s^{-1} in 0.33 cm^3_{STP} s^{-1} flowing helium. Meanwhile, gases were introduced to the system for a minimum of 30 minutes to stabilize the gas composition. Pressure transducers (Omega, PX32B1) were placed upstream and downstream of the catalyst bed to monitor the pressure drop across the reactor. For catalytic batch reactions, a four-way valve which introduced reactant gas flows to the batch reactor system was closed after the gas composition had stabilized, filling the closed system with a defined amount of gas and CH_4 internal standard. Gases were recirculated with an in-line recirculating pump (Senior Metal Bellows, MB-21) (see Fig. S1 for a simplified batch reactor schematic). Gas species compositions in the batch reactor system were monitored by comparison to the number of moles of CH_4 internal standard in the batch reactor system. Prior to the start of reaction, GC injections were taken to measure gas species concentrations in the batch reactor system. A 6-way valve connected to the reactor was switched to incorporate the reactor into the batch reactor system to commence reactions.

Stoichiometric C_2H_2 combustion reactions on Bi_2O_3 remove O atoms as CO_2 and H_2O. The number of O atoms still remaining in the oxide at any point during batch reactions can be assessed by Eq. S1, where $m_o(0)$ is the number of moles of O atoms in a fully stoichiometric Bi_2O_3 oxide, $m_O(t)$ is the number of moles of O remaining, $n_i(t)$ is the number of moles of an O-containing species i, and x_i is the number of moles of O contained within species i in the recirculating batch reactor.

$$m_O(t) = m_O(0) - \sum_i x_i n_i(t) \tag{S1}$$

The fraction of O atoms remaining in the oxide at any point during reduction or oxidation is then given by θ_O, shown in Eq. S2.

$$\theta_O(t) = \frac{m_O(t)}{m_O(0)} \tag{S2}$$

Rates of product evolution and reactant consumption in a recirculating batch reactor are evaluated by a finite difference method through three consecutive measurements, as shown in Eq. S3 for rates of C_2H_2 consumption. Carbon balances closed within 10%. Reaction rates are normalized by the number of O atoms remaining in the oxide during stoichiometric reduction half-cycles.

$$r(C_2H_2) = \frac{dn_{C_2H_2}}{dt}\frac{1}{m_O(t)} \approx \frac{\Delta n_{C_2H_2}}{\Delta t}\frac{1}{m_O(t)} \tag{S3}$$

During either batch or flow reactions in which both C_2H_2 and C_2H_4 are present as reactants with differing concentrations, we define the selectivity to C_2H_2 activation as the ratio of the pseudo-first order rate constant for the consumption of C_2H_2 to the sum of the pseudo first-order rate constants for C_2H_2 consumption and C_2H_4 consumption, as shown in Eq. S4 and Eq. S5.

$$Acetylene\ selectivity = \frac{\hat{k}(C_2H_2)}{\hat{k}(C_2H_2) + \hat{k}(C_2H_4)} \tag{S4}$$

$$\hat{k}(C_2H_x) = -\frac{r(C_2H_x)}{P(C_2H_x)} \tag{S5}$$

Reactant conversions during experiments in a recirculating batch reactor were assessed using Eq. S6.

$$X_i(t) = \frac{n_i(0) - n_i(t)}{n_i(0)} \tag{S6}$$

During flow reactions, species concentrations were monitored by both GC and online mass-spectrometry (MS) (MKS Cirrus 2). The online MS was placed downstream of the GC with gases positioned to flow into the capillary feeding the online MS (see Fig. S2). Response factors for gas species in the MS (relative to Ar, m/z = 40) were calculated by calibration against gas flow rates enumerated by GC and were updated after each GC injection. In experiments with mixtures of C_2H_4 and C_2H_2, C_2H_4 species concentrations were measured by the intensity of m/z = 27 relative

to m/z = 40. C_2H_2 concentrations were measured by the intensity of m/z = 26 relative to m/z = 40 after subtraction of the contribution to m/z = 26 from C_2H_4.

N_2 physisorption

Nitrogen adsorption isotherms were collected at 77 K with an ASAP 2020 surface area and porosity analyzer (Micromeritics) after degassing approximately 20 g of Bi_2O_3 at < 150 Pa at 393 K for 4 h to remove water. The Brunauer-Emmett-Teller (BET) (*35*) surface area obtained from the N_2 physisorption isotherm was 0.2 $m^2\ g^{-1}$, indicating the nonporous nature of Bi_2O_3.

X-ray Diffraction (XRD)

Powder XRD patterns were collected with a Rigaku Smartlab XE in the 2θ range of 20-60° with a scan rate of 2.5° min^{-1} and step size of 0.005° in Bragg-Brentano geometry with Cu Kα radiation. During temperature programmed XRD experiments, samples were mounted in an Anton Parr DHS 1100 in-situ cell with a graphite dome surrounding the sample to allow for control of the gas environment. Peaks corresponding to the graphite dome are marked in the diffraction patterns for temperature programmed XRD experiments. Prior to each scan collected at elevated temperature, the sample was heated to the temperature setpoint at a rate of 0.167 K min^{-1}, and the beam was realigned.

X-ray Absorption Spectroscopy (XAS)

XAS spectra at Bi L_3-edge were collected at beamline 9-3 of Stanford Synchrotron Radiation Lightsource (SSRL) at SLAC National Laboratory. Beamline 9-3 is a 16-pole, 2-tesla wiggler beamline with a vertically collimating mirror for harmonic rejection and a cylindrically bent mirror for focusing. The photon energy was selected using a liquid-nitrogen cooled, double-crystal Si (220) monochromator (crystal orientation = 0°). Fresh, redox-cycled, and partially reduced Bi_2O_3 sample pellets (~38 mg) were prepared by dilution with cellulose to a 1:10 Bi_2O_3:cellulose weight and were pressed into 7-mm diameter pellets with a hand press (International Crystal Laboratories). The XAS data were collected in transmission mode using N_2-filled ion chambers. Pepto-Bismol® (bismuth subsalicylate, $C_7H_5BiO_4$) was used as a reference, and it was scanned simultaneously with the Bi_2O_3 samples for energy calibration. The maximum of the first derivative position of the Pepto-Bismol® scan at 13,418.6 eV was used for energy calibration. A total of 4 scans were collected for each sample to improve signal-to-noise ratio of the XAS spectrum.

The Demeter software package was used for data processing and analysis (*36*). For calibration, normalization, and background subtraction, the Athena software was used. EXAFS modeling was performed using Artemis software. For generating scattering paths, the crystal structure of Bi_2O_3 was obtained from Ivanov et al. (*32*). The monoclinic unit cell of α-Bi_2O_3 has two Bi atoms with unique coordination environments; accordingly, aggregate scattering paths (margin of 0.2 Å and beta of 3°) used to fit fresh and redox-cycled Bi_2O_3 were generated with Artemis software. EXAFS of fresh Bi_2O_3 and redox-cycled Bi_2O_3 were modelled using one Bi-Bi and three Bi-O first shell Bi-O scattering paths generated with the aggregate function. The k-range of 4.01 $Å^{-1}$ < k < 13.4 $Å^{-1}$ and R-range of 1 Å < r < 4 Å were used for the fitting, with a Hanning window with dk = 1 $Å^{-1}$ and dr = 0 Å. Application of these fitting procedures to fresh α-Bi_2O_3 yielded an amplitude reduction factor of 0.74. Partially reduced Bi_2O_3 samples were fit using one Bi-O and one Bi-Bi aggregate scattering path (margin of 0.1 Å and beta of 3°) from α-Bi_2O_3 and one Bi-Bi scattering path from Bi metal (*33*) with a k range of 4.01 $Å^{-1}$ < k < 12.4 $Å^{-1}$ (dk = 1 $Å^{-}$

[1]) and an R range of 1 Å < R < 4 Å (dR = 0 Å) and a Hanning window. The amplitude reduction factor was fixed at 0.74 for fitting of partially reduced Bi_2O_3 samples.

Scanning Electron Microscopy (SEM)

SEM images were obtained with a Hitachi SU8230 Field Emission Gun with a 5 kV electron beam accelerating voltage. Samples were sputter coated on carbon to avoid effects from electron charging.

Scanning Transmission Electron Microscopy (STEM)

Fresh and redox-cycled Bi_2O_3 catalyst specimens were prepared into electron-transparent cross-sections for STEM studies using focused-ion beam performed on a FEI Helios NanoLab G4 dual-beam system. A protective amorphous-C (a-C) layer of 1 μm and Pt were deposited on the region of interest before ion milling. The FIB was operated at 30 kV with 5 kV electron beam. The specimens were investigated using an aberration-corrected FEI Titan G2 60-300 (S)TEM microscope equipped with a CEOS DCOR probe corrector, a monochromator, and a super-X EDX spectrometer. The microscope was operated at 200 kV with a STEM incident probe convergence angle of 25.5 mrad and a probe current of 80 pA. HAADF-STEM images were acquired at a detector inner and outer collection of angles of 55 and 200 mrad respectively. The STEM-EDX elemental maps were acquired and analyzed using Bruker Espirit software.

X-ray photoelectron spectroscopy (XPS)

X-ray photoelectron spectroscopy (XPS) analysis of fresh, partially reduced, and redox cycled Bi_2O_3 samples was conducted with a PHI 5000 Versaprobe III Photoelectron Spectrometer at 298 K using a monochromated Al K_α source (1486.6 eV). Binding energies were calibrated in reference to the C 1s peak at 285 eV.

Computational methods

First-principles periodic density functional theory (DFT) calculations were carried out using the Vienna Ab-initio Simulation Package (VASP) (*37-40*). Projector-Augmented Wave (PAW) potentials were used to describe interactions between core and valence electrons (*41, 42*). The Perdew-Burke-Ernzerhof (PBE) functional was used to determine the exchange and correlation energies (*43*). The energy cutoff for the plane-wave basis set is 396 eV. Electronic and ionic convergence criteria were set at 10^{-6} eV and 0.05 eV $Å^{-1}$, respectively, with a Gamma-centered (2 x 2 x 1) K-point mesh grid. Gaussian smearing was used with a smearing width of 0.02 eV. Transition state structures were initially established by the climbing image nudged elastic band (CI-NEB) (*44*) and were subsequently isolated by the Dimer (*45*) method. All calculations are spin unpolarized. Charge analyses were carried out by the Charge Model 5 (CM5) (*46*) in cluster models using the Gaussian16 program (*47*). The M-06L exchange-correlation functional was employed (*48*). The Stuttgart/Dresden effective core potentials and basis set (*49*) were used for Bi atoms, while the diffusion Dunning basis set aug-cc-pVDZ (*50*) was applied for C, H, and O atoms. Cluster models were cut out from the VASP-optimized periodic structures. Dangling oxygens were capped by hydrogen atoms as detailed in Fig. S23.

Computational model of α-Bi_2O_3

The α-Bi_2O_3 bulk structure was retrieved from the Materials Project database (*51*). The surface model consists of an α-Bi_2O_3 (010) slab with approximately four Bi-O layers and a 14 Å

vacuum (see Fig. S22), with the bottom two layers fixed to resemble the rigidity of the bulk. The (010) facet was theoretically predicted by Lei and Chen (*27*) to be the most stable facet of α-Bi_2O_3. We note that these authors suggested that low-index facets have small differences in surface energies, potentially leading to different exposed facets in actual catalysts. In our model, we terminate the surface with Bi as lattice oxygen is consumed during combustion reactions, leaving Bi exposed on the surface. This termination creates a topmost layer consisting of 3-coordinated Bi (Bi_{3c}) defect sites and 5-coordinated (Bi_{5c}) bulk-like sites. Attempts to adsorb substrates on Bi_{5c} sites were unsuccessful, indicating that these sites are saturated. Hence, subsequent calculations focused on the defect sites Bi_{3c} which will be referred to hereafter and in the main text as only Bi.

Supplementary Text

Assessment of heat and mass transport limitations

The Bi_2O_3 catalyst used in this study has an external surface area of 0.20 $m^2\ g^{-1}$ and is nonporous, ruling out internal mass and heat transport limitations. The absence of external mass transfer limitations was assessed by Eq. S7, from Chapter 3 of Froment, Bischoff, and De Wilde (*52*)

$$\Delta p_A = \frac{r_A M_m p_{fA} Sc^{2/3}}{a_m G j_d} \quad \text{(S7)},$$

where Δp_A is the partial pressure drop of reactant acetylene from the bulk fluid phase to the surface of the catalyst (bar), r_A is the reaction rate per gram of catalyst (mol $C_2H_2\ s^{-1}\ g_{cat}^{-1}$), M_m is the mixture molar mass (g mol^{-1}), p_{fA} is the film pressure factor (bar), Sc is the Schmidt number, a_m is the catalyst surface area ($m^2\ g^{-1}$), G is the mass flux rate (kg $m^{-2}\ s^{-1}$), and j_d is the mass transfer factor. The following calculations assess mass transfer limitations for C_2H_2 combustion on Bi_2O_3 upon exposure of 3.3 kPa C_2H_2 in N_2 to 285 mg Bi_2O_3 at 663 K. Upon introduction of the reactant mixture to Bi_2O_3, the rate of acetylene consumption, evaluated across the first three consecutive data points, is 4.6×10^{-8} mol $C_2H_2\ s^{-1}\ g_{cat}^{-1}$ at an average $P(C_2H_2)$ of 1.1 kPa. The mixture molar mass is 27.93 g mol^{-1}, as evaluated by Eq. S8.

$$M_m = \sum_i^N y_i M_i \quad \text{(S8)}$$

The film pressure factor is given by Eq. S9, where p_t is the total pressure and p_A is the C_2H_2 pressure. For the combustion of C_2H_2 by lattice oxygen of Bi_2O_3 to form two CO_2 molecules and one H_2O molecule, δ_A is two, yielding a film pressure factor of 1.08 bar.

$$p_{fA} = p_t + \delta_A p_A \quad \text{(S9)}$$

The Schmidt number, shown in Eq. S10, is assessed using the mixture viscosity (Eq. S11), mixture density (Eq. S12), and C_2H_2 diffusivity in N_2. At 663 K, the viscosity of the mixture is 3.14×10^{-5} kg $m^{-1}\ s^{-1}$ (*53*), and the gas density is 0.51 kg m^{-3}. The diffusivity of C_2H_2 in N_2 is $6.64 \times 10^{-5}\ m^2\ s^{-1}$ (*54*). The corresponding Schmidt number is 0.92.

$$Sc = \frac{\mu_m}{\rho_m D_{Am}} \quad \text{(S10)}$$

$$\mu_m = \sum_i^N y_i \mu_i \quad \text{(S11)}$$

$$\rho_m = \frac{M_m}{V_0}\frac{T_0}{T} \quad \text{(S12)}$$

The Reynolds number is given by Eq. S13, where d_p is the particle diameter. A recirculation rate of 5 $cm^3_{STP}\ s^{-1}$ was measured in the recirculating batch reactor, corresponding to a molar flow rate of 2.04×10^{-4} mol s^{-1}. For a reactor bed with a diameter of 10.5 mm, the mass flux rate, G, is

6.6×10^{-2} kg s^{-1} m^{-2}. Catalyst particles were crushed and sieved between 40-80 mesh to yield agglomerates with diameters ranging from 1.8×10^{-4} m to 4.2×10^{-4} m. The average particle diameter used in this calculation is 2.5×10^{-4} m, yielding a Reynolds number of 0.53. The mass transfer factor for Re < 190 is given by Eq. S14. For a Reynolds number of 0.53, the mass transfer factor is 2.30. The corresponding C_2H_2 partial pressure drop from the bulk fluid to the catalyst surface is 4.3×10^{-8} bar, indicating minimal contributions by external mass transfer resistances on surface reaction rates.

$$Re = \frac{d_p G}{\mu_m} \tag{S13}$$

$$j_d = 1.66 Re^{-0.51} \tag{S14}$$

In chemical looping combustion, reduction and oxidation half cycles occur in distinct steps with distinct enthalpic contributions which must sum to the enthalpy of the overall reaction. For C_2H_2 combustion, shown in Eq. S15, the enthalpy of reaction at 298 K is -1256 kJ mol^{-1} (*30*). The oxidation half cycle (Eq. S16) is exothermic with an enthalpy of approximately -300 kJ mol^{-1} (*16*, *28*); this energy is equal in magnitude to the oxygen vacancy formation energy. The corresponding enthalpy of the reduction half cycle (Eq. S17) which closes the balance between the enthalpy of the overall C_2H_2 combustion reaction and the formation of five oxygen vacancies is 244 kJ mol^{-1}. The following calculations assess the magnitude of the temperature drop from the bulk fluid to the catalyst surface using Eq. S18 from Chapter 3 of Froment, Bischoff, and De Wilde (*52*).

$$C_2H_2 + {}^5/_2\, O_2 \rightarrow 2CO_2 + H_2O \tag{S15}$$

$${}^1/_2\, O_2 + O_{vac} \rightarrow O_L \tag{S16}$$

$$C_2H_2 + 5O_L \rightarrow 2CO_2 + H_2O + 5O_{vac} \tag{S17}$$

$$\Delta T = \frac{r_A(-\Delta H) Pr^{2/3}}{a_m j_h C_{pm} G} \tag{S18}$$

In Eq. S18, the enthalpy of the reduction half cycle is given by ΔH (J mol^{-1}), Pr is the Prandtl number, j_h is the heat transfer factor, and C_{pm} is the heat capacity of the reaction mixture. The Prandtl number is given by Eq. S19

$$Pr = \frac{C_{pm}\mu_m}{M_m \lambda_m} \tag{S19},$$

where λ_m is the mixture thermal conductivity (W m^{-1} K^{-1}). The mixture thermal conductivity is 0.049 W m^{-1} K^{-1}, yielding a Prandtl number of 0.72 (*53*). The heat transfer factor was obtained from Fig. 3.2.2-1 in Froment, Bischoff, and De Wilde and has a value of 1 (*52*). The corresponding temperature difference between the catalyst surface and bulk fluid is 6.1×10^{-4} K, indicating that heat transfer resistances are negligible.

Reactor configurations used in catalytic testing

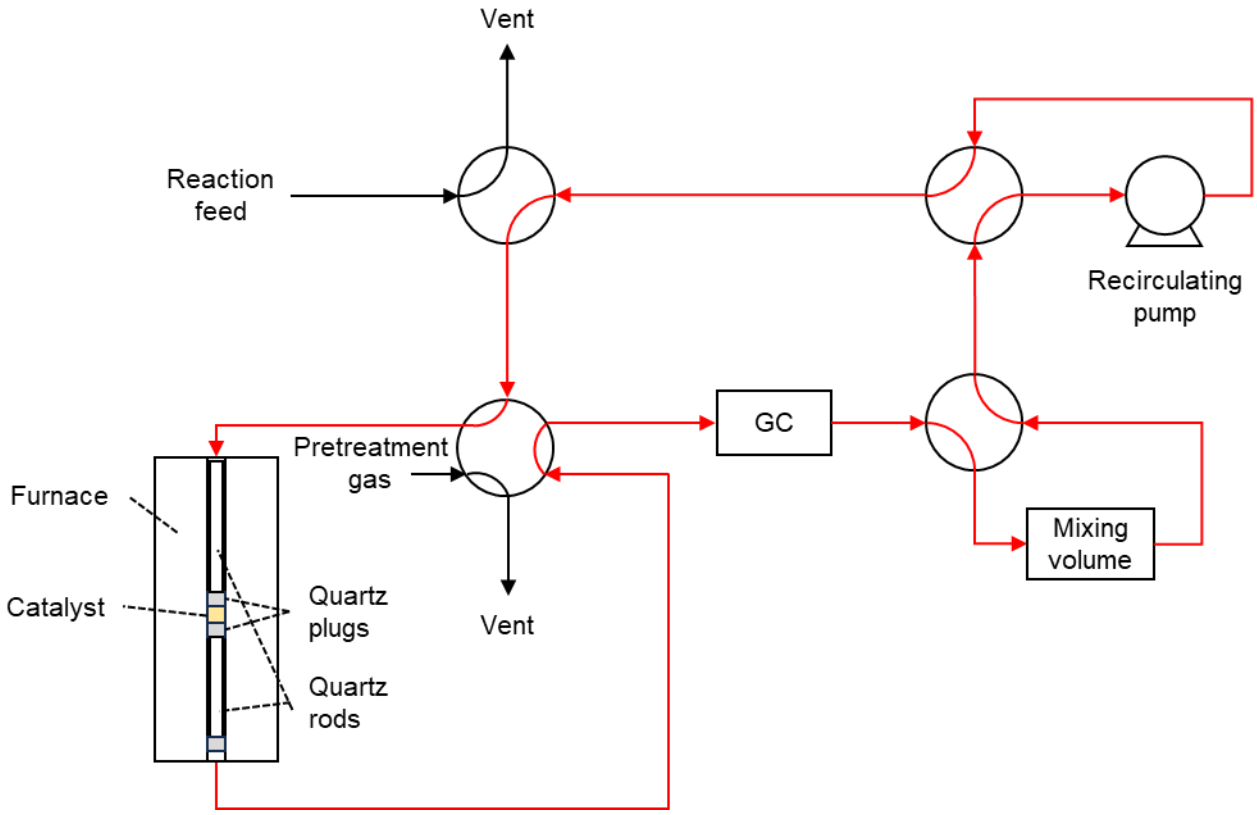

Fig. S1. Recirculating batch reactor diagram

Flow diagram illustrating the components of a recirculating batch reactor. The catalyst is isolated between quartz wool plugs, with quartz rods placed upstream and downstream of the catalyst inside of a quartz reactor tube which is heated by an annular furnace. During the pretreatment phase, pretreatment gases are metered to the reactor and sent out to the vent, while reaction gases are metered through the system, which includes the GC, mixing volume, and recirculating pump, before being sent to the vent. After gas flows stabilize, the four-way-valve sending reaction gases to the unit is switched, isolating the reaction gases inside of the batch reactor volume. The recirculating pump is then switched on, and the gas composition of the batch reactor is analyzed by GC in the absence of any reaction. The catalytic reaction is commenced by switching the six-way-valve controlling gas flows to the reactor to incorporate the reactor into the batch reaction system with reaction gases. For more details regarding batch reactor operation, see https://bhan.cems.umn.edu/software.

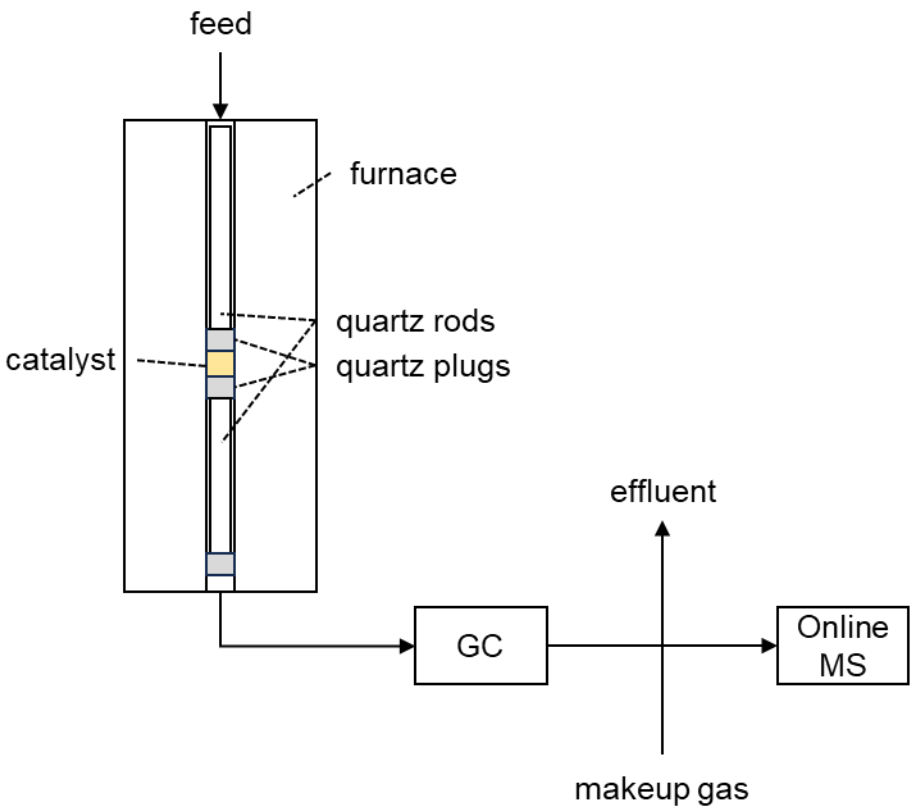

Fig. S2. Mass spectrometer flow diagram

Simplified diagram illustrating the flow configuration during flow reactions using the online MS. The flow after the GC is directed towards the stream going to the MS, while a makeup gas stream ensures that gas will flow to the MS and the effluent even if the feed flow is interrupted.

Redox cycling experiment reducing Bi_2O_3 to θ_O~0.8

Fig. S3 shows the C_2H_2 selectivity and product evolution rates during stoichiometric reduction half-cycles, and Fig. S4 shows the rate of oxygen consumption across 10 redox cycles during the subsequent oxidation half-cycles. Fig. S5 compares the moles of carbon reacted by C_2H_2 combustion during reduction steps to the moles of carbon removed as CO_2 during the subsequent oxidation steps. In each oxidation step, fewer than 1.3% of the C atoms reacted could be removed as CO_2, indicating minimal coke formation.

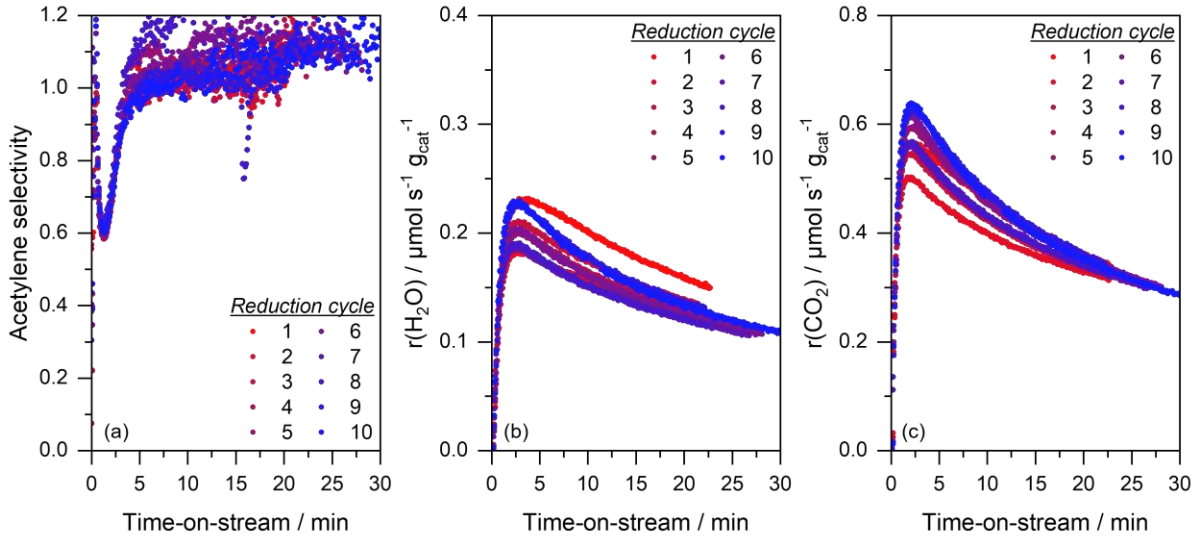

Fig. S3. Reduction half cycles during redox cycling at θ_O > 0.7

(a) Selectivity to acetylene combustion, as defined by Eq. S4, and combustion product (b) H_2O and (c) CO_2 evolution rates during reduction half cycles measured in a flow reactor. C_2H_2 combustion rates during this experiment are shown in Fig. 1f. Flow reaction conditions: $m(Bi_2O_3)$=1004.2 mg, T=673 K. Reduction conditions: $P(C_2H_4)=P(C_2H_2)$=1.1kPa, $P(CH_4)$=1.4 kPa, $P(N_2)$=20.9 kPa, balance Ar, total flow rate=1.67 cm^3_{STP} s^{-1}. Oxidation conditions: $P(O_2)$=2.4 kPa, P(He)=21.8 kPa, balance Ar, total flow rate = 1.67 cm^3_{STP} s^{-1}. The catalyst was isolated in 0.17 cm^3_{STP} s^{-1} He between reduction and oxidation treatments. Species concentrations were measured with an online mass spectrometer in reference to the flow rate of the Ar internal standard (m/z = 40). Samples referred to hereafter as redox-cycled were prepared during this experiment.

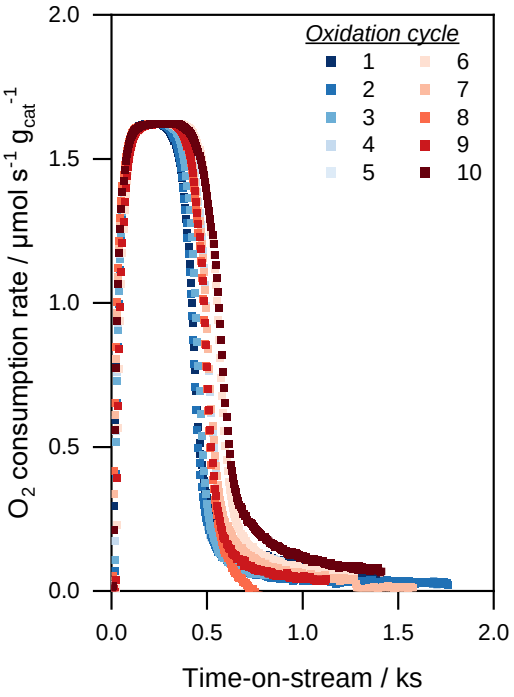

Fig. S4. Oxidation half cycles during redox cycling at θ_O > 0.7

Rates of oxygen consumption during oxidation half-cycles in a flow reactor after partial reduction of Bi_2O_3 in reduction half-cycles (shown in Fig. S3). Maximum bed-averaged O_2 consumption rates of 1.6 µmol s^{-1} g_{cat}^{-1} were achieved due to full conversion of influent O_2. Flow reaction conditions: m(Bi_2O_3)=1004.2 mg, T=673 K. Reduction conditions: P(C_2H_4)=P(C_2H_2)=1.1kPa, P(CH_4)=1.4 kPa, P(N_2)=20.9 kPa, balance Ar, total flow rate =1.67 cm^3_{STP} s^{-1}. Oxidation conditions: P(O_2)=2.4 kPa, P(He)=21.8 kPa, balance Ar, total flow rate = 1.67 cm^3_{STP} s^{-1}. The catalyst was isolated in 0.17 cm^3_{STP} s^{-1} He between reduction and oxidation treatments. Species concentrations were measured with an online mass spectrometer in reference to the flow rate of an Ar internal standard (m/z = 40). Samples referred to hereafter as redox-cycled were prepared during this experiment.

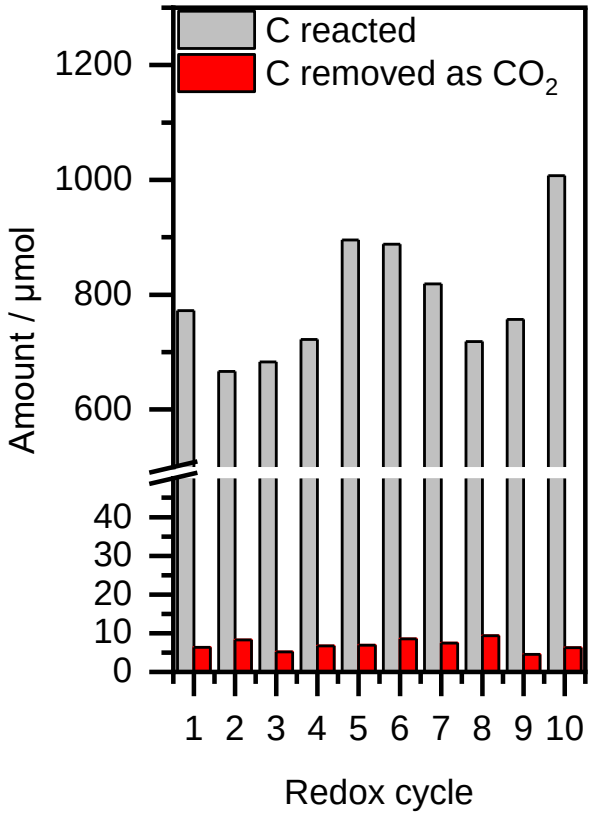

Fig. S5. Carbon reacted during reduction half cycles and carbon removed during oxidation half cycles

Amounts of C reacted (obtained by the consumption of C_2H_2) during the reduction half cycles and C removed as CO_2 during subsequent oxidation half cycles in the experiment detailed in Fig. 1, E and F, and Figs. S3 and S4. The number of C atoms removed as CO_2 was quantified by tracking the intensity of the m/z=44 fragment relative to the m/z=40 fragment from the argon internal standard in the reactor effluent with an online mass spectrometer.

Redox cycling experiment with only C_2H_4 as a reductant

A reduction experiment with only C_2H_4 present as a reductant was performed. The maximum C_2H_4 consumption rate during this experiment was approximately 0.35 μmol s^{-1} g_{cat}^{-1}, before the rate drops below 0.05 μmol s^{-1} g_{cat}^{-1}. If C_2H_4 combustion was responsible for this initially high C_2H_4 activation rate, the corresponding CO_2 and H_2O evolution rates would exhibit a maximum of 0.70 μmol s^{-1} g_{cat}^{-1}. The left y-axis axis of Fig. S6 shows the CO_2 and H_2O evolution rates which peak at 0.0017 and 0.0007 μmol s^{-1} g_{cat}^{-1}, respectively, which is over two orders of magnitude lower than what would be expected if the spike in C_2H_4 consumption were due to C_2H_4 combustion. No other products were detected in this experiment, suggesting that the peak in C_2H_4 consumption is due to reactor hydrodynamics when the 6-way-valve is switched to commence the reaction. Transient behavior is observed for the first 0.1 ks in each experiment performed in flow configuration with an online mass-spectrometer.

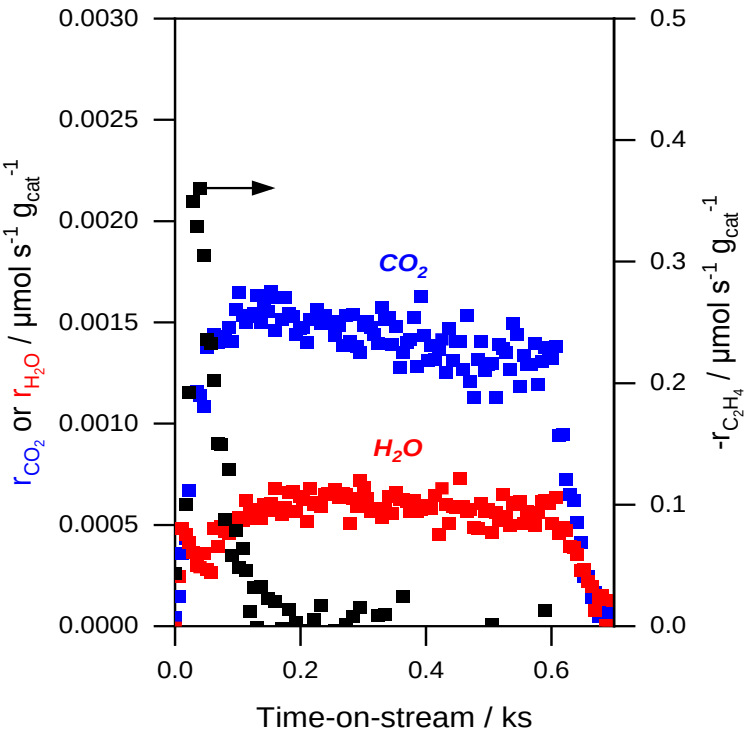

Fig. S6. Redox cycling with C_2H_4

Reduction experiment performed in a flow reactor with product concentrations monitored with an online mass spectrometer. Flow reaction conditions: m(Bi_2O_3)=1.000 g, T=673 K, P(C_2H_4)=21.5 kPa, P(CH_4)=2 kPa, balance argon, total flow rate = 0.83 cm^3_{STP} s^{-1}. Species concentrations were monitored in reference to the flow rate of the Ar internal standard (m/z = 40).

Redox cycling experiment at θ_O>0.9

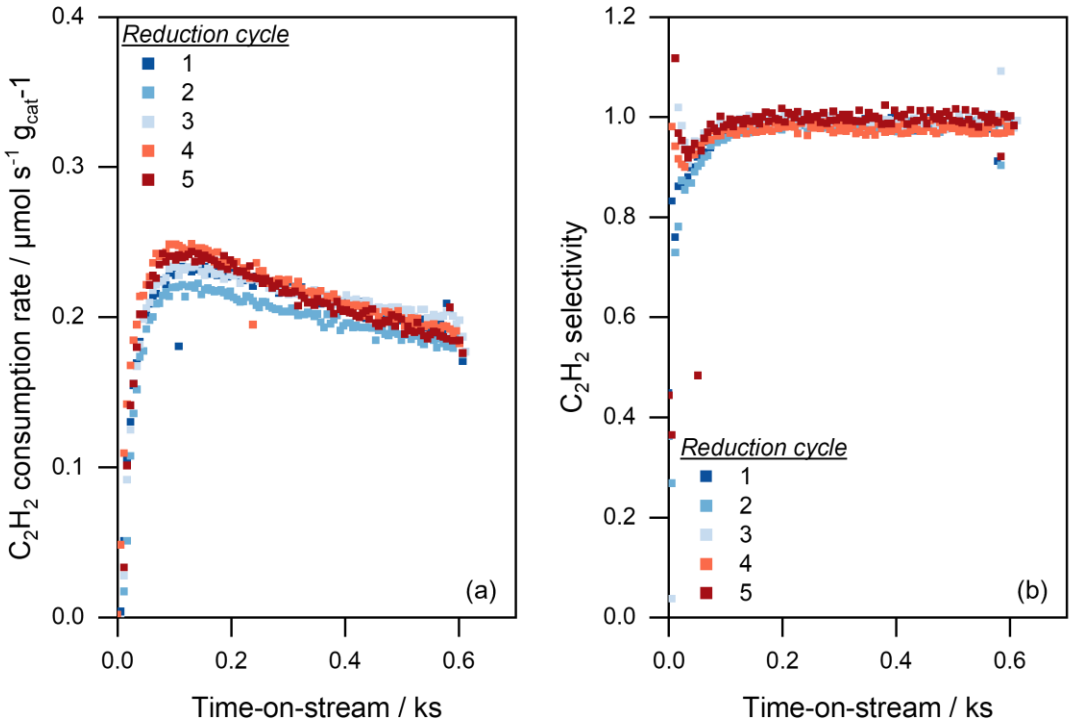

Fig. S7. Reduction half cycles during redox cycling with θ_O > 0.9

Reactant (a) C_2H_2 consumption rates and (b) selectivity to acetylene activation, as defined by Eq. S4, in a redox cycling experiment performed in a flow reactor with species concentrations monitored with an online mass spectrometer. Reaction conditions: T=673 K, m(Bi_2O_3)=984.7 mg. Reduction conditions: P(C_2H_2)=2.15 kPa, P(C_2H_4)=21.5 kPa, P(CH_4)=2 kPa, P(Ar)=34.8 kPa, balance N_2, total flow rate = 0.83 cm^3_{STP} s^{-1}. Oxidation conditions: P(O_2)=6.7 kPa, P(Ar)=34.8 kPa, balance helium, total flow rate = 0.83 cm^3_{STP} s^{-1}. Reducing treatments progressed for 10 minutes each. Between each reduction and oxidation step, the catalyst was exposed to He with a flow rate of 0.33 cm^3_{STP} s^{-1} for at least 15 minutes. Species concentrations were monitored relative to the flow rate of the Ar internal standard (m/z = 40).

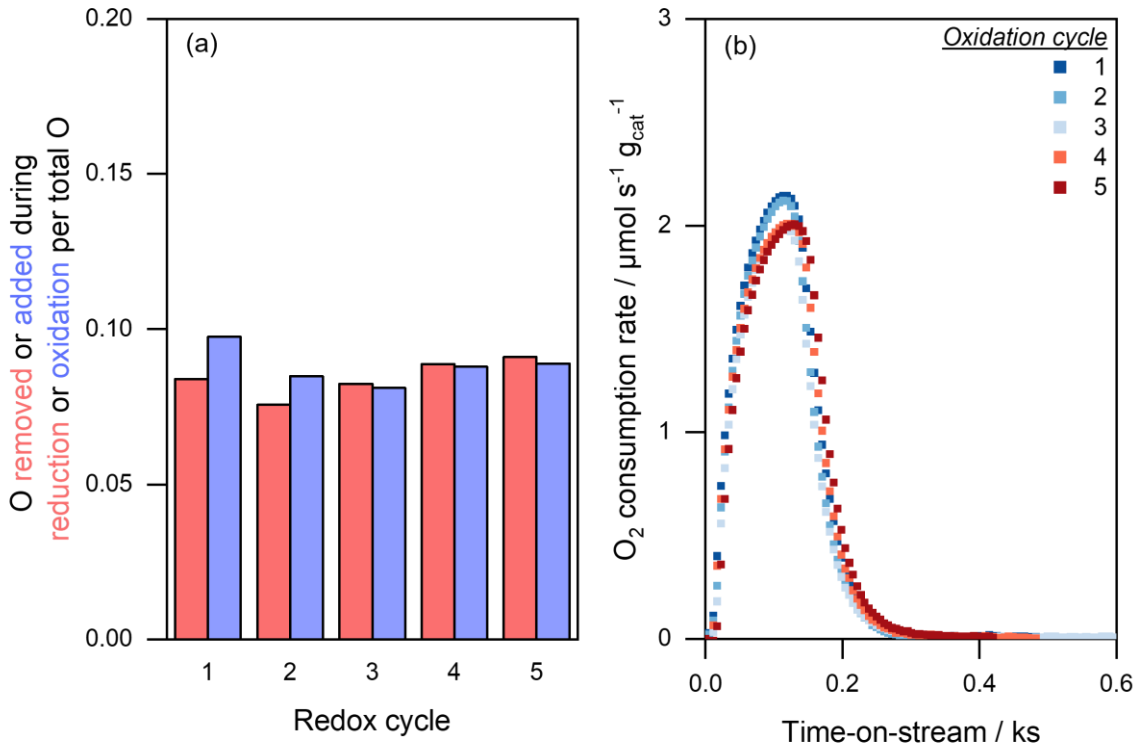

Fig. S8. Mass balances and oxidation half cycles during redox cycling with θ_O > 0.9

(a) Mole balances tracking the number of O atoms removed during reduction half cycles and added during oxidation half cycles, relative to the number of oxygen atoms initially available in the stoichiometric Bi_2O_3 catalyst, and (b) rates of O_2 consumption during oxidation half cycles monitored in a flow reactor. Reaction conditions: T=673 K, m(Bi_2O_3)=984.7 mg. Reduction conditions: P(C_2H_2)=2.15 kPa, P(C_2H_4)=21.5 kPa, P(CH_4)=2 kPa, P(Ar)=34.8 kPa, balance N_2, total flow rate = 0.83 cm^3_{STP} s^{-1}. Oxidation conditions: P(O_2)=6.7 kPa, P(Ar)=34.8 kPa, balance helium, total flow rate = 0.83 cm^3_{STP} s^{-1}. Reducing treatments progressed for 10 minutes each. Between each reduction and oxidation step, the catalyst was exposed to He with a flow rate of 0.33 cm^3_{STP} s^{-1} for at least 15 minutes. O_2 flow rates were monitored with an online mass spectrometer in reference to the flow rate of the Ar internal standard (m/z = 40).

Additional details of the dwell experiment for a 1:10 mixture of C_2H_2:C_2H_4 on Bi_2O_3

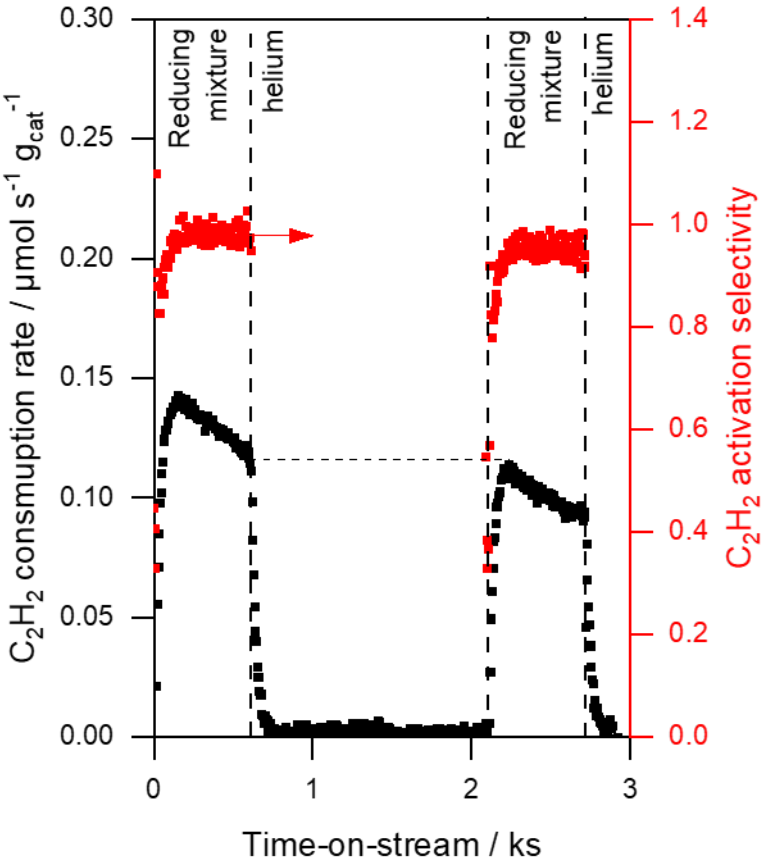

Fig. S9. Acetylene consumption rates and selectivity during a dwell experiment

Rate of C_2H_2 consumption and selectivity to C_2H_2 activation, as defined by Eq. S4, during a dwell experiment with 1:10 C_2H_2:C_2H_4 as a reductant and helium as an inert gas during the dwell step. The catalyst was reduced to θ_O = 0.93 by the end of the first reduction step. Flow reaction conditions: T=673 K, m(Bi_2O_3)=1.0 g, P(C_2H_2)=2.2 kPa, P(C_2H_4)=21.5 kPa, P(CH_4)=2 kPa, P(Ar)=34.8 kPa, balance nitrogen, total flow rate = 0.83 cm^3_{STP} s^{-1}. During the dwell step, the catalyst was exposed to helium with a flow rate of 0.83 cm^3_{STP} s^{-1} for 1.5 ks. Species concentrations were monitored relative to the flow rate of the Ar internal standard (m/z = 40).

Evaluation of the relative rates of oxygen diffusion and surface reactions from 573 K to 773 K

Temperature programmed reduction (TPR) was used to assess the temperature at which C_2H_2 begins to reduce Bi_2O_3. Upon exposure of Bi_2O_3 to 1.0 kPa C_2H_2, combustion products were detected at 555 K (Fig. S10). The flow rates of CO_2 and H_2O eventually decay to zero due to consumption of the lattice oxygen by C_2H_2 combustion.

Dwell experiments were repeated at 573 K and 773 K to assess oxygen diffusion constraints at a range of process conditions. At 573 K, product evolution rates before and after the inert purge step employed to alleviate oxygen concentration gradients were equal, indicating lattice oxygen diffusion does not limit measured rates of selective C_2H_2 combustion (Fig. S11). Acetone is formed with a higher selectivity at lower operating temperatures. In the dwell experiment repeated at 773 K, combustion rates increased by ~ 1.6× after the dwell step, indicating that, unlike at 573 K or 673 K, oxygen diffusion begins to limit combustion rates at 773 K (Fig. S12). The rate of O removal by C_2H_2 combustion at the end of the fist reduction step is 73 μmol s^{-1} m^{-2}.

Although the dwell experiment at 673 K provides evidence that O diffusion to catalytically relevant surfaces does not limit the rate of surface reactions, the dwell experiment does not provide a measure of the relative rates of surface reaction and lattice oxygen diffusion. To probe this, an experiment was performed in a recirculating batch reactor in which the Bi_2O_3 catalyst was reduced with C_2H_2, the system was purged with helium, and then the catalyst was reoxidized with molecular oxygen. The rate of formation of combustion products during the reduction step provides a measure of the rate of abstraction of O from the Bi_2O_3 surface, unconvoluted by oxygen diffusion limitations. Subsequently, when the reactor is purged with helium and the partially reduced catalyst is exposed to molecular oxygen, the rate of reoxidation provides a measure of the rate at which O can be reincorporated back into the catalyst. If the rate of oxygen diffusion from the surface to the bulk (and analogously the rate of oxygen vacancy diffusion to the surface) is slower than the rate of reoxidation with molecular oxygen, then the rate measured in this experiment corresponds directly to the rate of lattice oxygen diffusion. If, however, the rate of oxygen diffusion from the surface to the bulk exceeds the rate of reoxidation with molecular oxygen, then the measured rate of O uptake provides a lower bound on the rate for oxygen diffusion from the surface to the bulk.

Fig. S13 depicts the results of this experiment in which exposure of C_2H_2 to Bi_2O_3 at 673 K results in areal rates of lattice oxygen abstraction during the reduction step which decreased with batch time due to consumption of C_2H_2 from the batch reactor and consumption of lattice oxygen by combustion reactions. The reduction was stopped at a θ_O value of 0.63. The areal rate of lattice oxygen abstraction by C_2H_2 combustion on the surface prior to commencing the reaction was 1.4 μmol s^{-1} m^{-2} when evaluated at θ_O = 0.65 and $P(C_2H_2)$ = 3.0 kPa.

Subsequently, the reactor was purged with helium and isolated from the batch unit without cooling, and the batch unit was filled with a gas mixture containing helium, argon, and 4.8 kPa O_2. Upon exposure of the recirculating oxidant mixture to the partially reduced catalyst, 96% conversion of molecular oxygen is attained within 0.33 ks adding ~ 238 μmol O into the lattice, as shown in Fig. S14, corresponding to an areal rate of uptake of O atoms of 17.6 μmol s^{-1} m^{-2} evaluated at an average θ_O of 0.67 and an average $P(O_2)$ of 2.5 kPa. This value was interpreted as a lower bound on the rate of oxygen diffusion from the particle surface to the bulk (or analogously the rate of oxygen vacancy diffusion from the bulk to the surface).

Eq. S20 defines the Thiele modulus in this system as the ratio of the areal rate of lattice oxygen removal by combustion to the lower bound on the areal rate of oxygen diffusion evaluated at the particle surface at nearly equivalent extents of reduction (θ_O of 0.65 and 0.67, respectively).

The upper bound on the Thiele modulus evaluated at these conditions is 0.08, indicating that at 673 K, surface C_2H_2 combustion rates are far from conditions in which lattice O diffusion would limit the surface reaction rate, consistent with the dwell experiment performed at 673 K indicating no O diffusion limitations.

$$\phi^2 = \frac{Areal\ rate\ of\ O\ removal\ from\ the\ surface\ by\ reaction}{Areal\ rate\ of\ O\ replenishment\ to\ the\ surface\ by\ diffusion} = \frac{\left(2r_{CO_2} + r_{H_2O}\right)\big|_{r=r_p}}{r_{O,diff}\big|_{r=r_p}} \leq \frac{(2r_{CO_2} + r_{H_2O})\big|_{r=r_p}}{-2r_{O_2}\big|_{r=r_p}} \quad \text{(S20)}$$

An estimate for the apparent barrier of oxygen diffusion was assessed to understand how oxygen diffusion rates scale with temperature. We estimated a barrier for O diffusion by analyzing the rate at which partially reduced Bi_2O_3 is reoxidized by O_2, as shown in Fig. S15a; if diffusion rates exceed surface reoxidation rates, then measured oxidation rates provide a lower bound on diffusion rates, but if diffusion is slow, measured oxidation rates correspond directly to diffusion rates. We interpret reoxidation rates as a lower bound on O diffusion rates and use measured oxidation rates to estimate the barrier for O diffusion by assessing pseudo first-order rate constants for reoxidation by O_2 during the temperature ramp, as shown in Fig. S15b. The apparent barrier for oxidation of partially reduced Bi_2O_3 measured between 394 K and 464 K is 49 ± 2 kJ mol^{-1}. We carried out theoretical calculations to determine the intrinsic barrier for subsurface oxygen to diffuse to a defect site on the model (010) surface of α-Bi_2O_3, as shown in Fig. S15c. The intrinsic barrier for atomic oxygen to move from the subsurface was calculated to be 70 kJ mol^{-1} which is lower than the barriers for C-H activation and is exothermic with an overall energy of -13 kJ mol^{-1}.

Extrapolating the lower bound on the rate of O diffusion measured at 673 K of 17.6 μmol s^{-1} m^{-2} to 773 K via the Arrhenius expression shown in Eq. S21 using an apparent barrier for O diffusion of 49 kJ mol^{-1}, the estimated rate of O diffusion at 773 K in Bi_2O_3 is 55 μmol s^{-1} m^{-2}. The rate of O removal at the end of the first reduction step during the dwell experiment shown in Fig. S12 is 73 μmol s^{-1} m^{-2}, indicating that O diffusion may be insufficient to replenish the O being removed from Bi_2O_3 surfaces exposed to 0.7 kPa C_2H_2 at 773 K. Differences in the activation barriers for C_2H_2 activation (113 ± 8 kJ mol^{-1}, see Fig. S16) on Bi_2O_3 surfaces and O diffusion in Bi_2O_3 (49 ± 2 kJ mol^{-1}) yield surface reaction rates which scale more strongly with temperature than O diffusion, leading to the observation of diffusion limitations which only appear at 773 K. These diffusion limitations are indicative of a Thiele modulus which is approaching or exceeding unity.

$$r_{O,diff} \propto \exp\left(-\frac{E_{app,O,diff}}{RT}\right) \quad \text{(S21)}$$

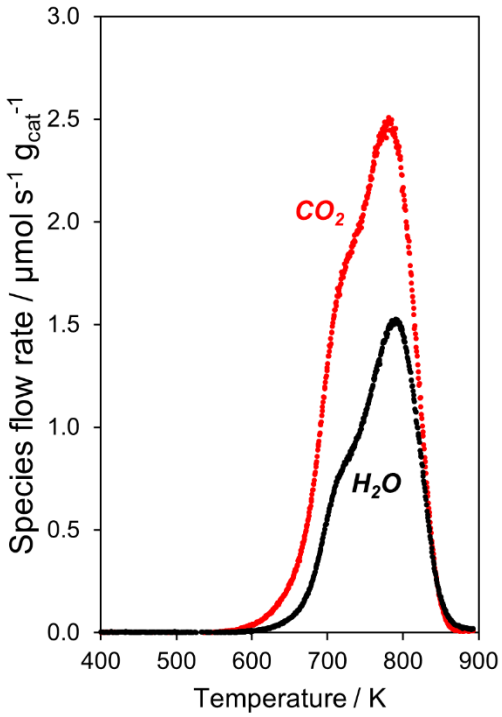

Fig. S10. Temperature programmed reduction of Bi_2O_3 by C_2H_2

CO_2 and H_2O flowrates upon exposure of C_2H_2 to Bi_2O_3 during a TPR experiment in which the temperature was ramped from 298 K to 873 K at 0.17 K s^{-1}. Combustion product flow rates were monitored by tracking the intensity of the m/z=44 and m/z=18 ions for CO_2 and H_2O, respectively, relative to the m/z=28 ion for N_2, which was used as an internal standard. Reaction conditions: m(Bi_2O_3) = 0.1143 g, $T_{initial}$ = 298 K, ramp rate = 0.17 K s^{-1}, P(C_2H_2) = 1.0 kPa, P(N_2) = 19.8 kPa, balance He, total flow rate = 1.67 cm^3_{STP} s^{-1}.

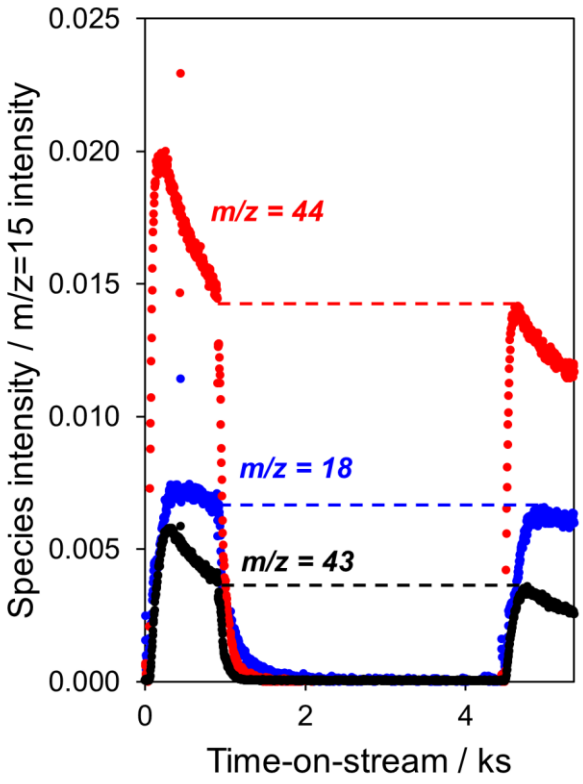

Fig. S11. Product flow rates during a dwell experiment at 573 K

Dwell experiment tracking the intensities of m/z=44, m/z=18, and m/z=43 which correspond to CO_2, H_2O, and acetone, respectively, relative to m/z=15 corresponding to the methyl fragment of the CH_4 internal standard with online mass spectrometry upon exposure of Bi_2O_3 to C_2H_2 at 573 K, with an intervening dwell step purging the reactor with helium. Ion intensities were not calibrated to enumerate flow rates. Reaction conditions: m(Bi_2O_3) = 2.003 g, T = 573 K, P(C_2H_2) = 2.2 kPa, P(CH_4) = 7.7 kPa, P(N_2) = 42.4 kPa, balance Ar, total flow rate = 0.5 cm^3_{STP} s^{-1}. During the dwell step, the reactor was exposed to pure He with a flow rate of 0.5 cm^3_{STP} s^{-1}.

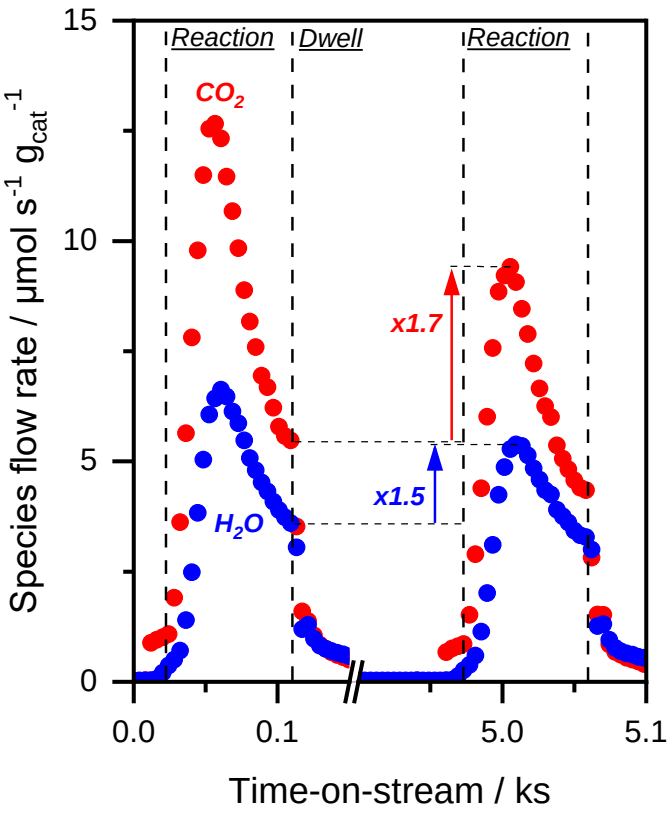

Fig. S12. Product flow rates during a dwell experiment at 773 K

Dwell experiment tracking effluent CO_2 and H_2O flow rates upon exposure of Bi_2O_3 to C_2H_2. Ions corresponding to CO_2 (m/z=44) and H_2O (m/z=18) were calibrated relative to m/z=15 corresponding to the methyl fragment of the CH_4 internal standard. The catalyst was reduced to θ_O = 0.83 after the first dwell step. Reaction conditions: m(Bi_2O_3) = 0.1906 g, T = 773 K, P(C_2H_2)$_0$ = 0.7 kPa, P(CH_4)$_0$ = 2.3 kPa, P(N_2) = 13.3 kPa, balance Ar, total flow rate = 1.67 cm^3_{STP} s^{-1}. During the dwell step, the reactor was exposed to pure He with a flow rate of 1.67 cm^3_{STP} s^{-1}.

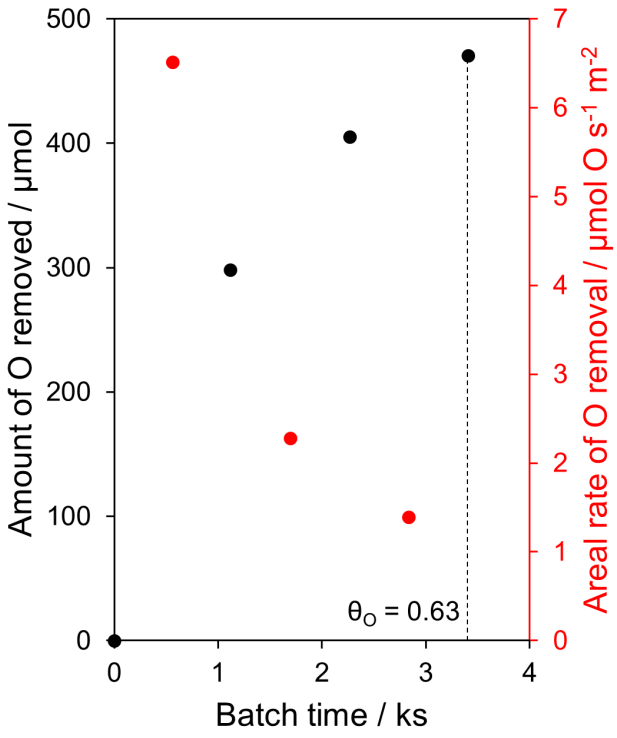

Fig. S13. Rates of O removal by C_2H_2 combustion on Bi_2O_3

Amount of O atoms removed from the Bi_2O_3 lattice upon exposure of the catalyst to C_2H_2 at 673 K in a recirculating batch reactor. The number of O atoms removed from the catalyst is enumerated by tracking the number of O atoms in CO_2 and H_2O combustion products in the recirculating batch reactor. The areal rate of O removal, normalized by the BET surface area of bulk Bi_2O_3 of 0.206 $m^2\ g^{-1}$ enumerated with N_2 physisorption, is plotted on the right y-axis. The reaction was stopped at θ_O of 0.63. Reaction conditions: m(Bi_2O_3) = 0.1989 g, T = 673 K, P(C_2H_2)$_0$ = 6.4 kPa, P(C_2H_4)$_0$ = 5.2 kPa, P(CH_4)$_0$ = 8.2 kPa, balance N_2. The reactor was initially pressurized to 140 kPa to minimize air leaks into the batch reactor.

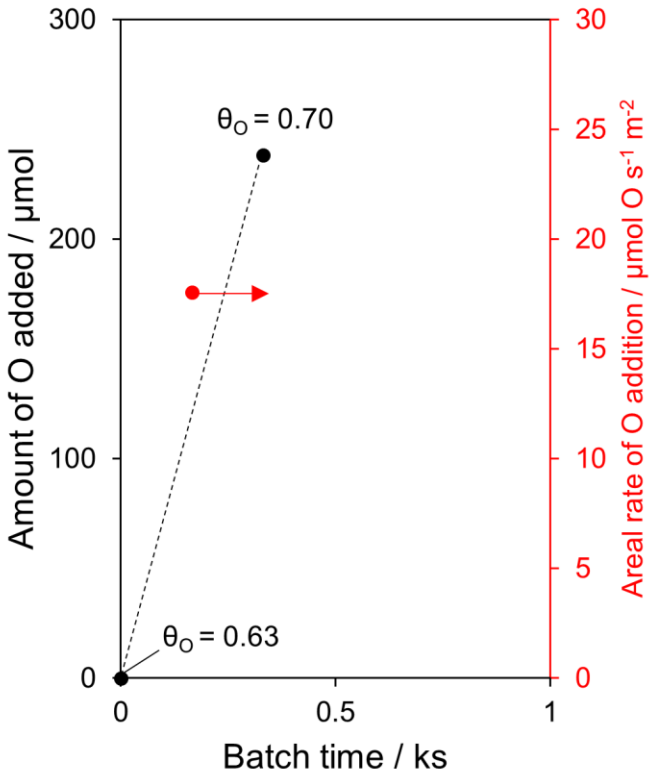

Fig. S14. Rates of O uptake by partially reduced Bi_2O_3 upon exposure to O_2

Amount of O atoms reincorporated into the O-deficient lattice of the partially reduced Bi_2O_3 (reduced to $\theta_O = 0.65$) catalyst prepared from the experiment shown in Fig. S13 upon exposure to molecular oxygen in a recirculating batch reactor. The areal rate of O addition is plotted on the right y-axis. Reaction conditions: $m(Bi_2O_3) = 0.1989$ g, T = 673 K, $P(O_2)_0 = 4.8$ kPa, $P(Ar)_0 = 11.4$ kPa, balance helium. The reactor was initially pressurized to 140 kPa to minimize air leaks into the batch reactor.

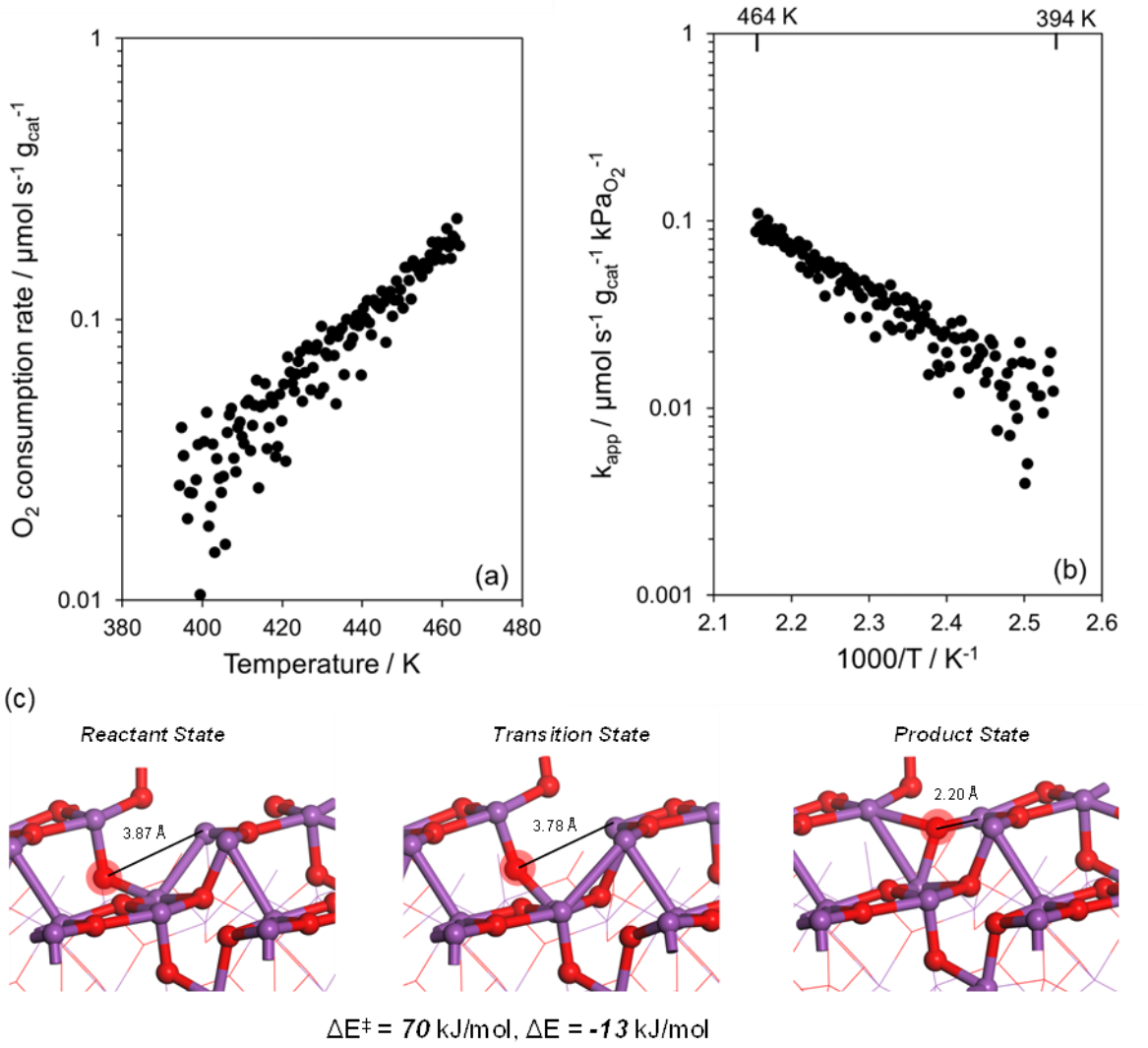

Fig. S15. Rates of reoxidation of partially reduced Bi_2O_3 during a temperature-programmed oxidation experiment with O_2 and the DFT-calculated pathway for vacancy filling with subsurface oxygen

(a) Rates of O_2 consumption and (b) pseudo first-order rate constants for oxidation of Bi_2O_3 by O_2 during a temperature-programmed oxidation (TPO) ramping the temperature from 308 K to 873 K at 0.17 K s^{-1}. The partially reduced Bi_2O_3 was prepared by an isothermal reduction at 673 K upon exposure of Bi_2O_3 to 1.0 kPa C_2H_2 at 1.67 cm^3_{STP} s^{-1} for 4.2 ks to remove 310 μmol O (θ_O = 0.84). The degree of reduction was calculated by integration of the flow rates of CO_2 and H_2O in the effluent during reduction. After reduction, the reactor was rapidly cooled to 308 K while stabilizing the O_2 flow in the bypass stream. The reoxidation was started simultaneously with the temperature program heating the catalyst from 308 K to 873 K at 0.17 K s^{-1}. The rate of O_2 consumption was tracked relative to the baseline O_2 ion intensity (m/z=32) with an Ar internal standard (m/z = 40). Only rates in the temperature range from 394 K to 464 K were used to enumerate an apparent barrier for O diffusion. Reaction conditions: m(Bi_2O_3) = 0.2953 g, $T_{initial}$ = 308 K, ramp rate = 0.17 K s^{-1}, P(O_2) = 2.1 kPa, P(He) = 18.5 kPa, balance Ar, total flow rate =

1.67 cm^3_{STP} s^{-1}. O_2 conversion remained below 5%. (c) DFT-calculated pathway for the diffusion of subsurface oxygen to fill an oxygen vacancy on the (010) surface of α-Bi_2O_3.

Kinetic evaluation of C_2H_2 combustion rates with CO_2, H_2O, and C_2H_4 cofeeds and at varying temperature

At reaction temperatures from 633 K – 663 K, C_2H_2 activation rates were first order in C_2H_2 partial pressure. Rates of C_2H_2 activation were measured in a recirculating batch reactor in the presence of CO_2 or C_2H_4 to probe the influence of CO_2 or C_2H_4 on the active sites for C_2H_2 activation. Rates of C_2H_2 activation were first order with the same apparent first order rate constant with cofeeds of CO_2 or C_2H_4. H_2O cofeeds led to a slight increase in C_2H_2 activation rates and an increase in selectivity to acetone. DFT calculations assessing the binding of water to exposed Bi sites on the (010) surface of α-Bi_2O_3 indicated that water weakly adsorbs with a binding energy of -27 kJ mol^{-1} and a free energy of 24 kJ mol^{-1}. As such, water is not likely to inhibit sites at the high temperatures (T > 663 K) and low water partial pressures ($P(H_2O)$ < 4 kPa) encountered during reaction conditions.

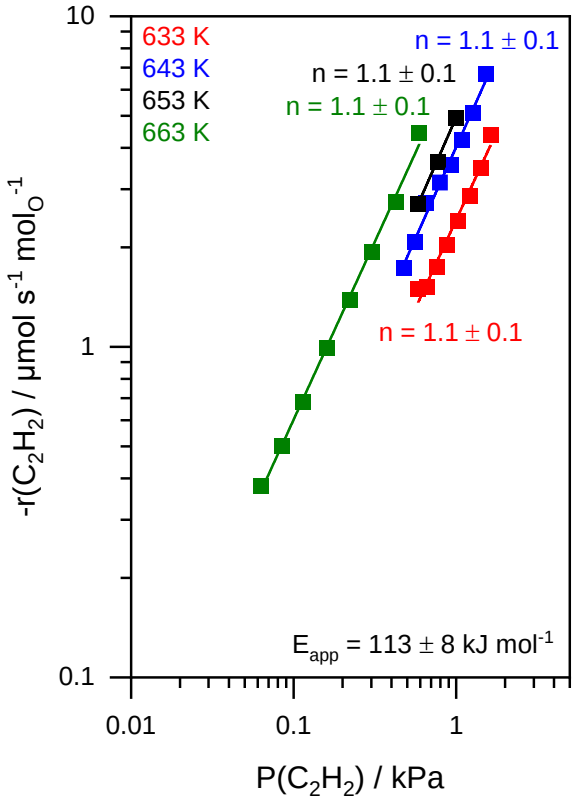

Fig. S16. Kinetics of C_2H_2 activation at 633 K – 663 K

Rates of C_2H_2 activation in batch experiments performed at varying initial C_2H_2 partial pressures. Rates decrease during batch experiments due to the stoichiometric consumption of the C_2H_2 reactant. Rates were calculated by a 3-point finite difference method. All rates were measured at θ_O > 0.8. Lines of best fit are shown for each temperature and show that the reaction is first-order in C_2H_2 partial pressure. The apparent activation energy was enumerated by fitting all data consisting of T and $P(C_2H_2)$ as independent variables and $-r(C_2H_2)$ as a dependent variable to an Arrhenius first-order rate expression in Origin.

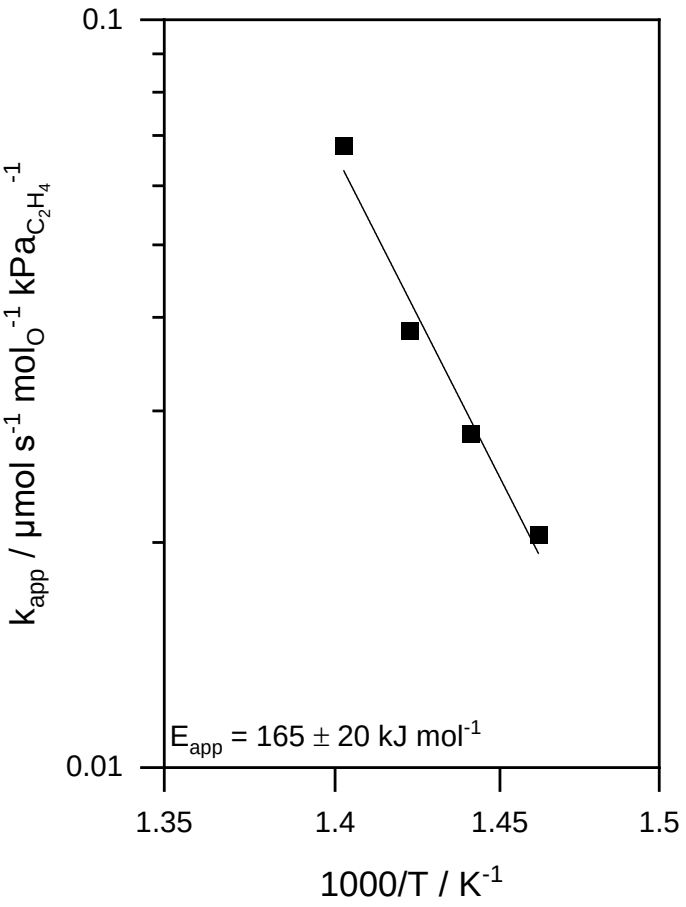

Fig. S17. Apparent barrier for C_2H_4 activation at 684 K – 713 K

The rate constants of C_2H_4 activation measured during independent experiments at varied temperatures in a recirculating batch reactor with C_2H_4 and an argon internal standard. In each experiment, the Bi_2O_3 catalyst mass was ~0.70 g. C_2H_4 activation rates were assessed by the initial rates of consumption of C_2H_4 from the batch reactor averaged across the first three or four data points during an experiment. Rates were normalized by the average number of moles of oxygen remaining in the Bi_2O_3 catalyst for the measured data points ($\theta_O > 0.99$ for each experiment) and by the average C_2H_4 partial pressure across these data points to enable quantification of a pseudo-first order rate constant for C_2H_4 activation. C_2H_4 conversion remained below 6%. The initial partial pressure of C_2H_4 in the batch reactor was 51 kPa during each experiment. The apparent barrier for C_2H_4 activation was assessed by fitting the apparent rate constants to an Arrhenius expression in Origin.

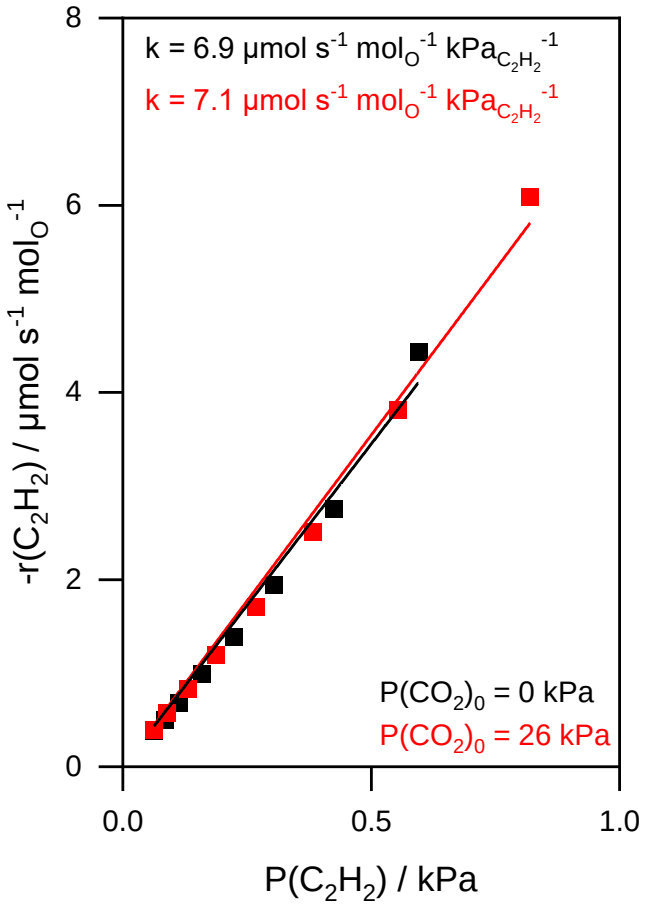

Fig. S18. Rate constants for C_2H_2 activation with CO_2 cofeed

The rates of C_2H_2 activation measured during independent batch reactor experiments with and without cofeed of CO_2. In both experiments, the mass of Bi_2O_3 catalyst is ~ 250 mg. CH_4 was used as an internal standard. The reaction temperature was 663 K. The first order rate constants for C_2H_2 activation as a function of C_2H_2 partial pressure are shown in the figure.

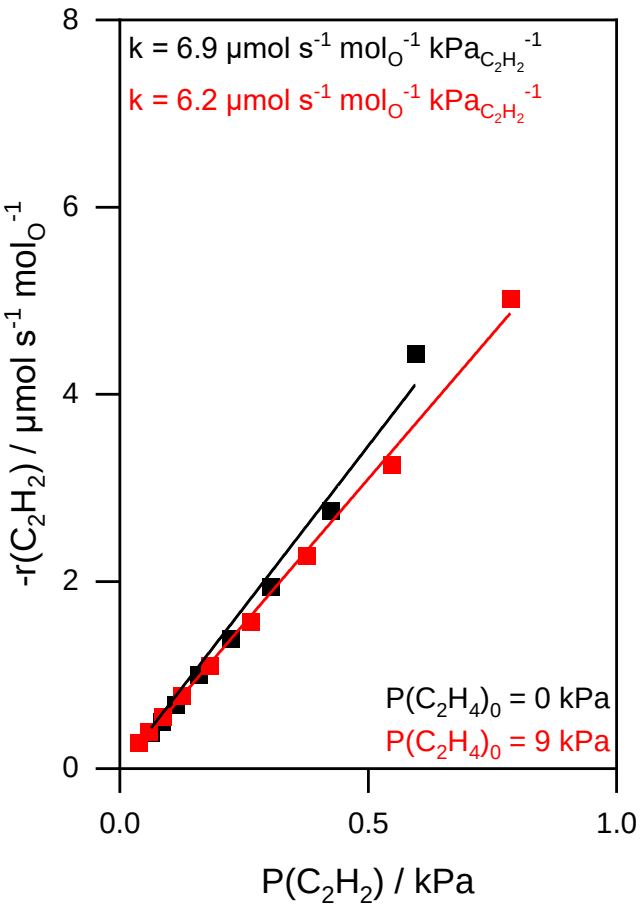

Fig. S19. Rate constants for C_2H_2 activation with C_2H_4 cofeed

The rate of C_2H_2 activation measured during independent batch reactor experiments with and without C_2H_4 cofeed. In both experiments, the mass of Bi_2O_3 catalyst is ~ 250 mg. CH_4 was used as an internal standard. The reaction temperature was 663 K. The first order rate constants for C_2H_2 activation as a function of C_2H_2 partial pressure are shown in the figure.

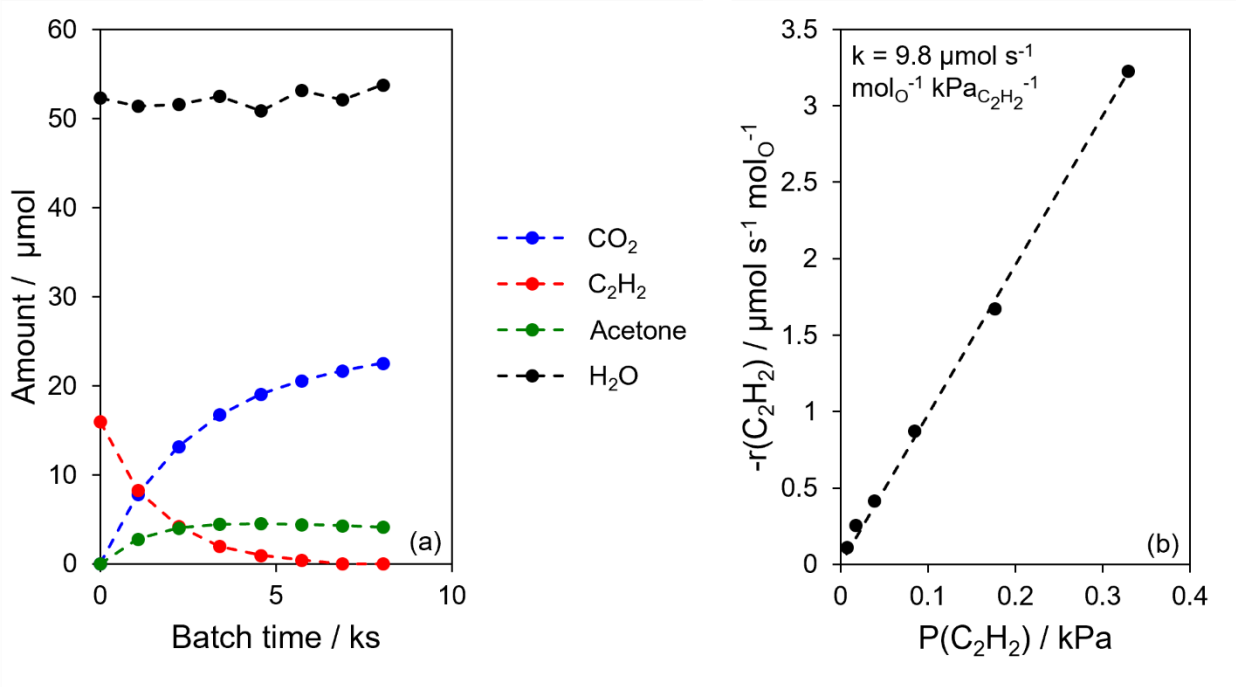

Fig. S20. Amounts of products formed and C_2H_2 activation rates upon exposure of C_2H_2 to Bi_2O_3 with H_2O cofeed

(a) Amounts of C_2H_2, CO_2, H_2O, and acetone and (b) rates of C_2H_2 activation during a batch reaction exposing C_2H_2 to Bi_2O_3 with water cofeed. Rates of acetylene activation were assessed based on the slope between three consecutive measures of the amount of C_2H_2 present in the batch reactor and were normalized by the moles of oxygen remaining in the catalyst at the midpoint. The degree of reduction of the catalyst remained below 7% during the experiment. Reaction conditions: $m(Bi_2O_3)$ = 0.255 g, T = 663 K, $P(C_2H_2)_0$ = 0.6 kPa, $P(H_2O)_0$ = 2.0 kPa, $P(CH_4)_0$ = 3.0 kPa, $P(N_2)_0$ = 11.5 kPa, balance helium.

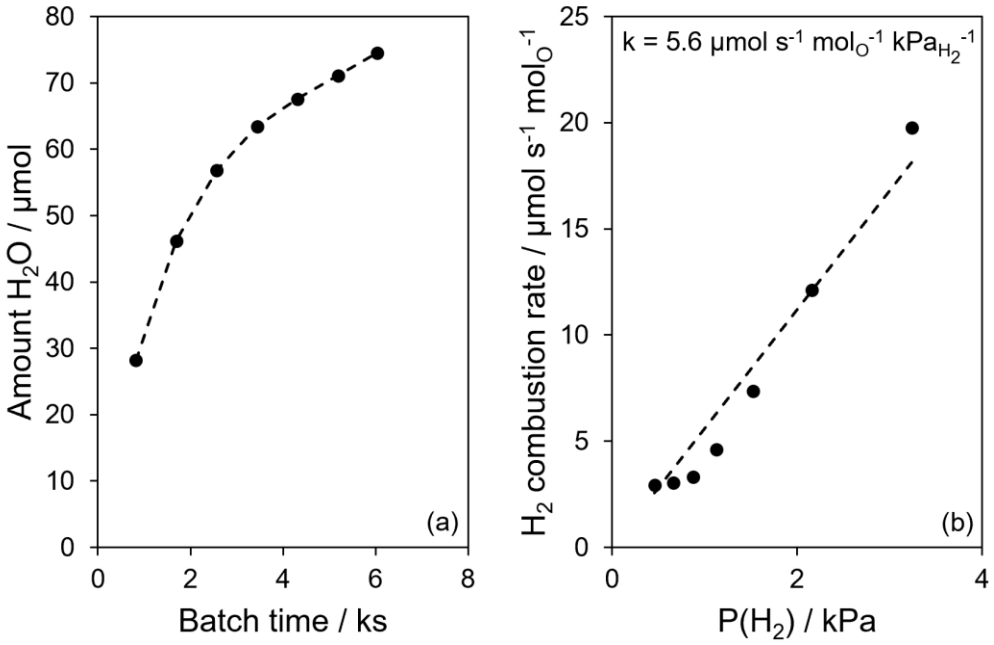

Fig. S21. Amount of water formed and H_2 combustion rates during H_2 combustion on Bi_2O_3
(a) Amount of water formed and (b) rates of H_2 combustion during an experiment in a recirculating batch reactor exposing H_2 to Bi_2O_3 at 663 K. Rates were assessed by the slope between three consecutive measures of the amount of H_2O in the batch reactor and were normalized by the moles of oxygen remaining in the catalyst at the midpoint. The degree of reduction of the catalyst remained below 6% during the experiment. Reaction conditions: $m(Bi_2O_3)$ = 0.217 g, T = 663 K, $P(H_2)_0$ = 4.9 kPa, $P(CH_4)_0$ = 3.0 kPa, balance helium. The batch reactor was initially pressurized to 139.8 kPa before reaction to minimize leaks of air into the reactor.

Bi_2O_3 surface model used for DFT calculations

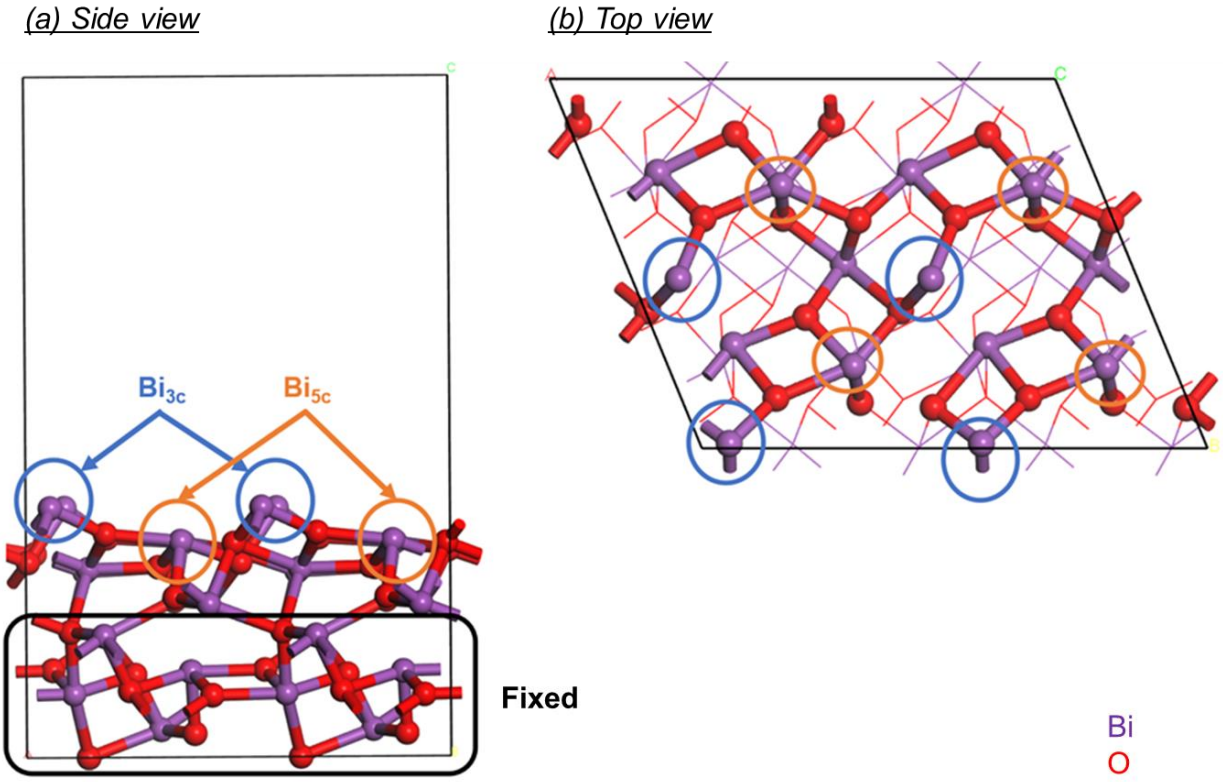

Fig. S22. Periodic Bi_2O_3 model

Periodic Bi_2O_3 model used for DFT calculations, showing the (a) side view and (b) the top view of the (010) facet of α-Bi_2O_3. The subsurface Bi (purple) and O (red) atoms remain fixed during calculations. The surface is terminated with 3-coordinated Bi atoms (Bi_{3C}) and 5-coordinated Bi atoms (Bi_{5C}), denoted by blue and orange circles, respectively.

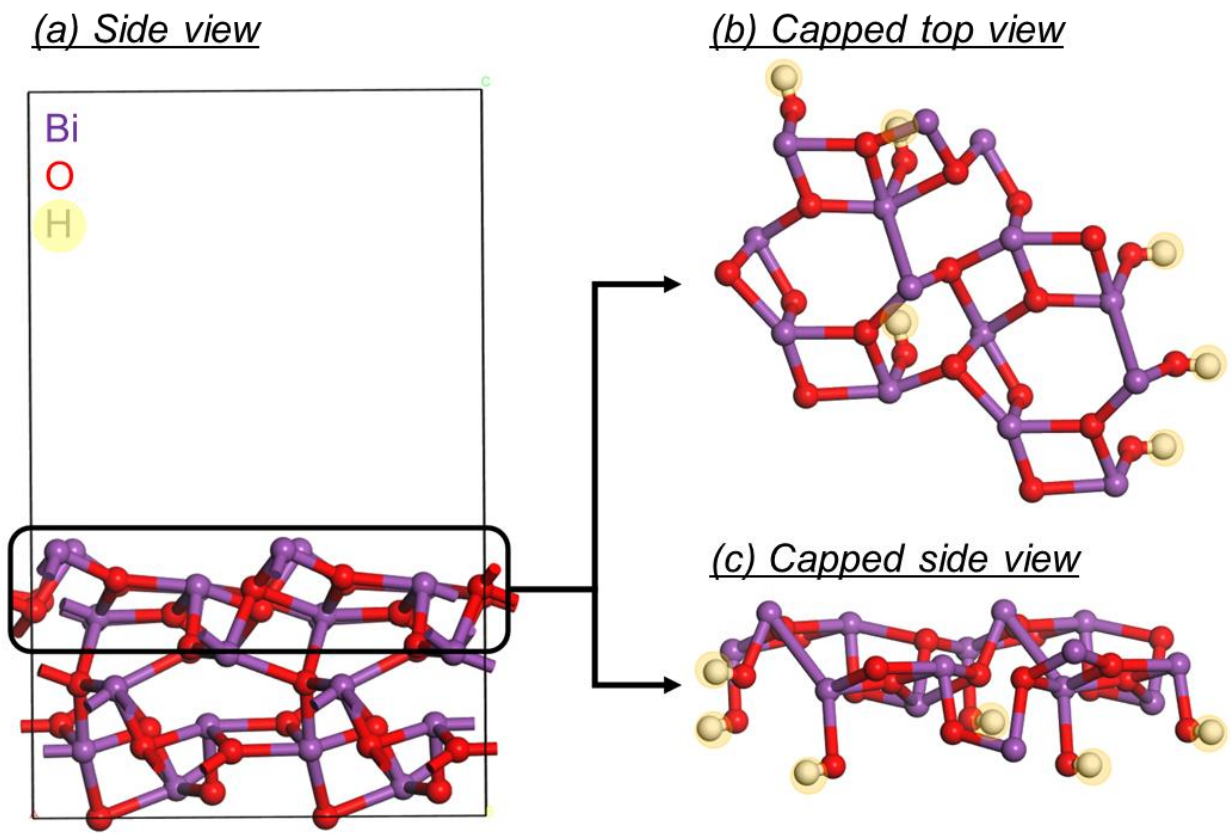

Fig. S23. Bi_2O_3 cluster model

(a) The optimized periodic slab of (010) α-Bi_2O_3 used in periodic DFT calculations. The black box encloses atoms that were cut to build cluster models used in Gaussian cluster calculations. (b) Top and (c) side views of the cluster model. Capping hydrogens (white) are highlighted with yellow circles. The cluster contains 14 Bi, 21 O, and 6 capping H atoms.

Evaluation of C-H activation pathways on Bi and Bi-O sites

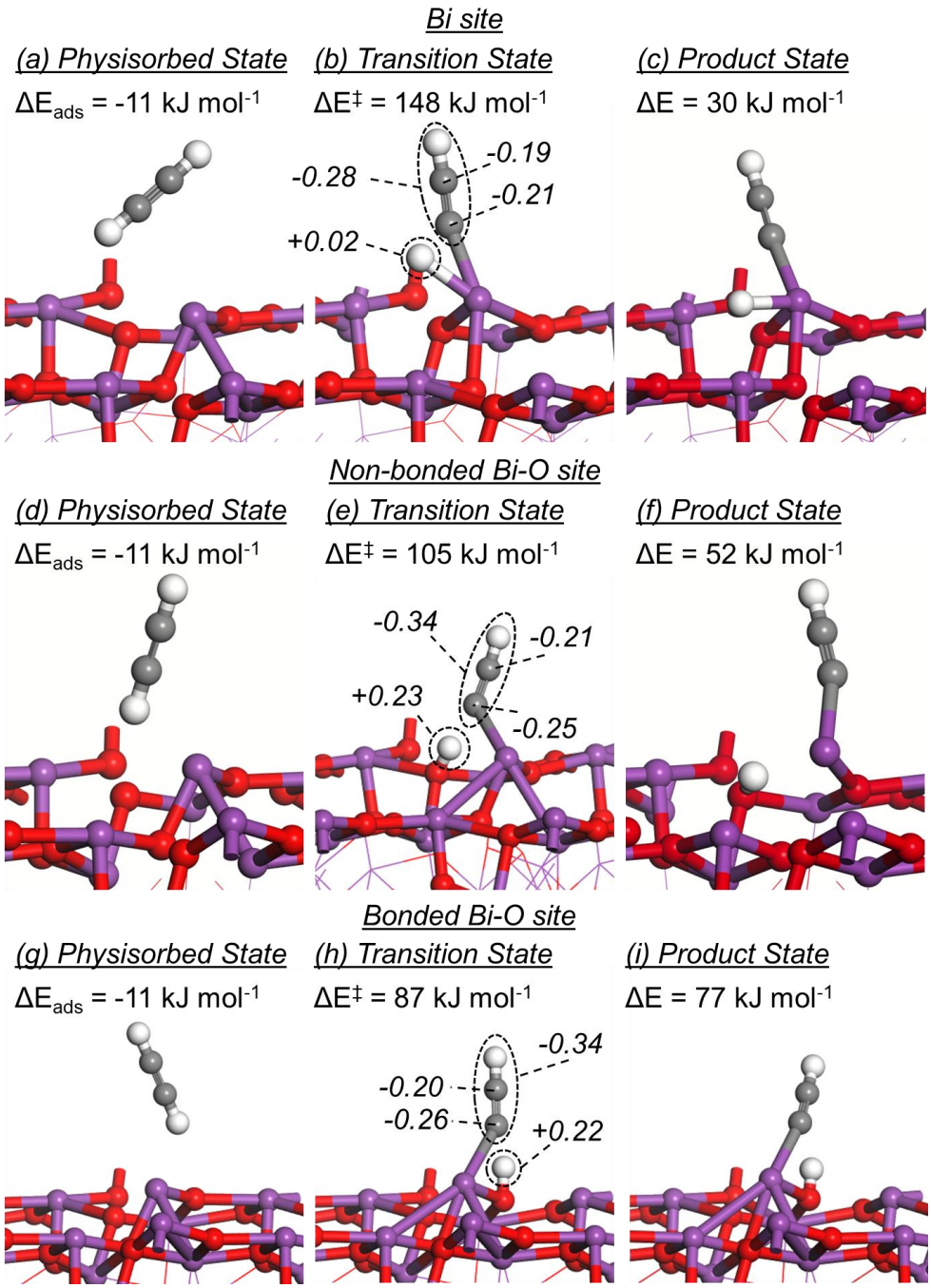

Fig. S24. Reactant states, transition states, and product states of C_2H_2 activation

Homolytic C_2H_2 activation on (a-c) a Bi site and heterolytic C_2H_2 activation on (d-f) a non-bonded Bi_{3c}-O site, and (g-i) a bonded Bi_{3c}-O site, showing the physisorbed state, transition state, and product state and the corresponding electronic energies on each site. In the transition state, the numbers shown correspond to atomic charges on C and H atoms and the net charge on the CCH fragment. Bi atoms are purple, O atoms are red, C atoms are gray, and H atoms are white.

Table S1. Geometries of C_2H_2 activation

Bi-H or O-H and Bi-C bond lengths in the physisorbed state, transition state, and product state during C_2H_2 activation on a Bi site, the non-bonded Bi-O site, and bonded Bi-O site.

	Bi site		Non-bonded Bi-O site		Bonded Bi-O site	
	Bi-H bond length / Å	Bi-C bond length / Å	O-H bond length / Å	Bi-C bond length / Å	O-H bond length / Å	Bi-C bond length / Å
Physisor-bed state	3.587	3.585	2.285	3.487	2.670	3.766
TS	2.011	2.343	1.049	2.577	1.101	2.630
Product state	1.935	2.353	1.007	2.254	0.990	2.357

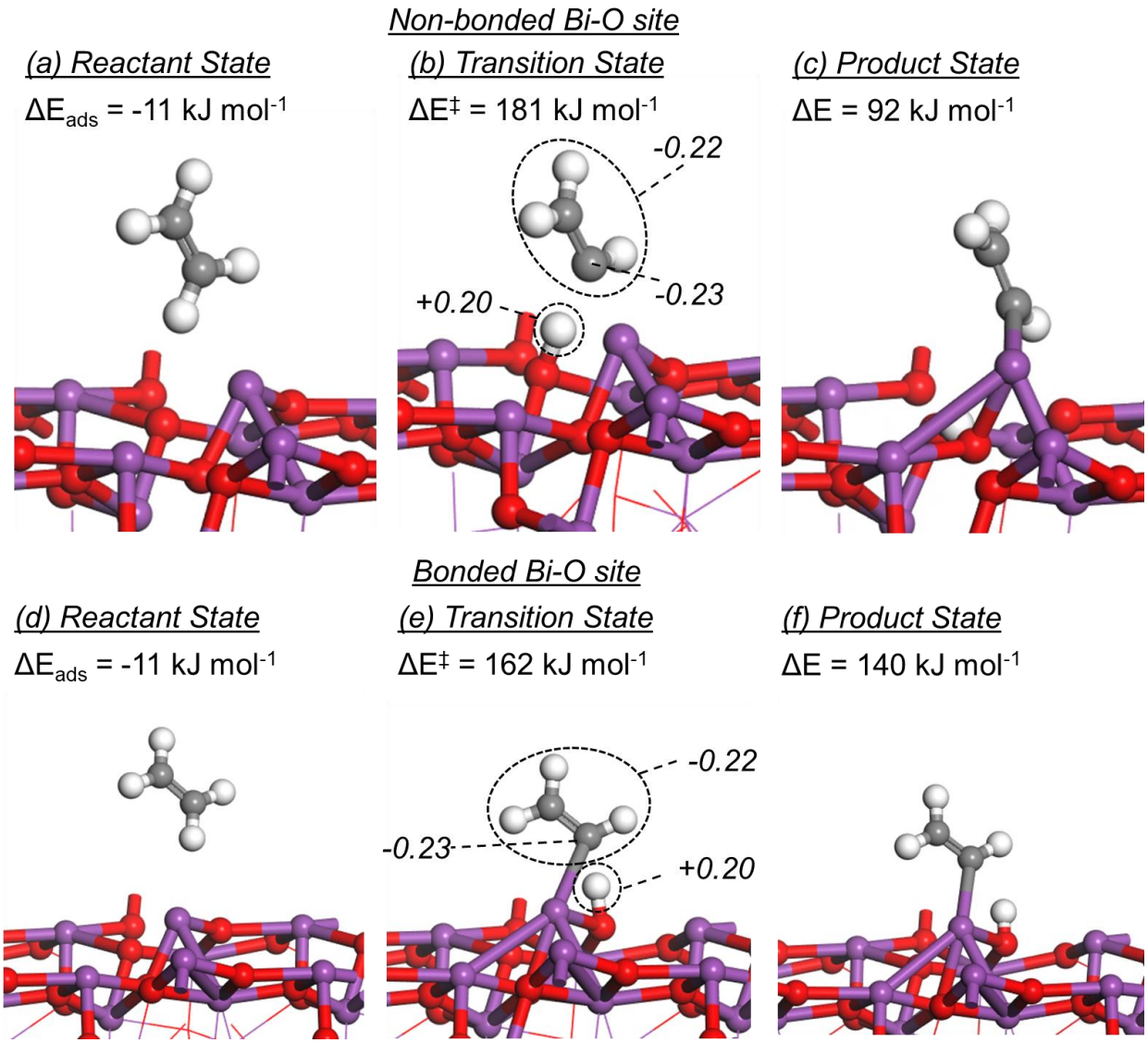

Fig. S25. Reactant state, transition state, and product state of C_2H_4 activation on Bi-O sites

C_2H_4 activation on (a-c) a non-bonded Bi-O site and (d-f) a bonded Bi-O site, showing the reactant states, transition states, and product states and the corresponding electronic energies. In the transition state (b), numbers shown correspond to atomic charges on C and H atoms and the net charge on the C_2H_3 fragment. Bi atoms are purple, O atoms are red, C atoms are gray, and H atoms are white.

Table S2. Geometry of C_2H_4 activation on Bi-O sites

O-H and Bi-C bond lengths in the physisorbed state, transition state, and product state during C_2H_4 activation on the non-bonded Bi-O site and the bonded Bi-O site.

	Non-bonded Bi-O site		Bonded Bi-O site	
	O-H bond length / Å	Bi-C bond length / Å	O-H bond length / Å	Bi-C bond length / Å
Physisorbed state	2.45	3.61	2.91	4.02
Transition state	1.11	2.64	1.11	2.61
Product state	1.01	2.25	0.98	2.34

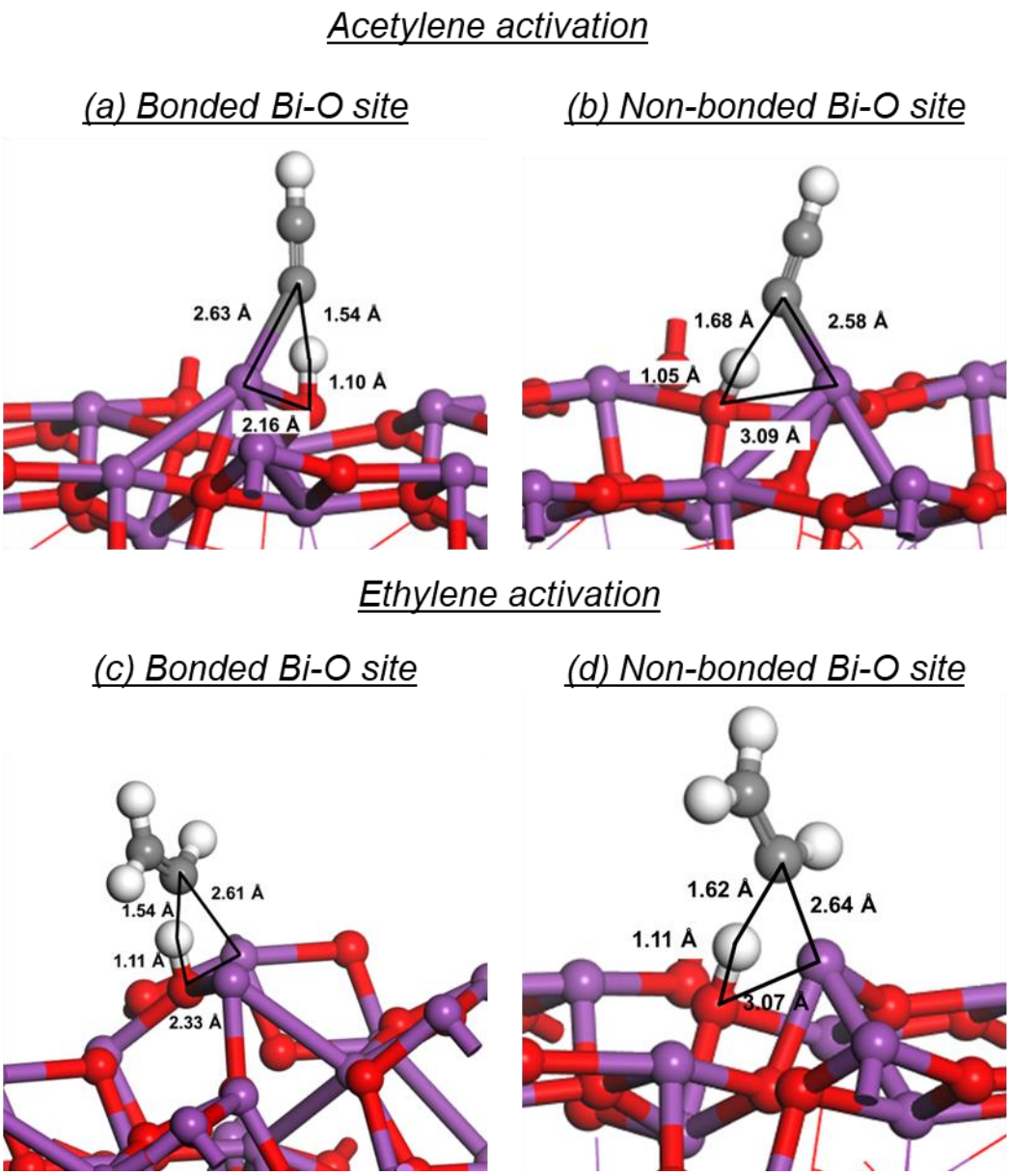

Fig. S26. Bond lengths in C-H activation transition states on bonded and non-bonded Bi-O sites

Bi-O, Bi-C, O-H, and C-H bond lengths for the transition states involved in acetylene activation on (a) bonded Bi-O sites and (b) non-bonded Bi-O sites and ethylene activation on (c) bonded Bi-O sites and (d) non-bonded Bi-O sites. Transition states on bonded Bi-O sites consistently have shorter C-H bonds. The Bi-C bonds in transition states on bonded Bi-O sites are longer for C_2H_2 but shorter for C_2H_4 compared to on non-bonded Bi-O sites. The O-H bonds in transition states on bonded Bi-O sites are longer for C_2H_2 but the same for C_2H_4 compared to on non-bonded Bi-O sites. The lower transition state energies observed for C-H activation on bonded Bi-O sites may be rationalized by earlier transition states, as assessed by the C-H bond distance, which can stabilize charged $R^{(\delta-)}$ and $H^{(\delta+)}$ intermediates on proximal Bi^{3+} and O^{2-} sites, respectively, more effectively than on non-bonded Bi-O sites with longer Bi-O bond distances.

Evaluation of alternative selective hydrocarbon combustion processes

Fig. S27 shows that Bi_2O_3 combusts 1,3-butadiene in propane with >98% selectivity, consistent with the hypothesis that more acidic hydrocarbon molecules are activated more readily on Bi_2O_3 surfaces to initiate combustion. We addressed the feasibility of selective combustion of 1,3-butadiene in 1-butene mixtures by evaluating rate constants for activation of 1,3-butadiene and 1-butene in independent batch reactions. Fig. S28 shows the consumption of 1,3-butadiene in a batch reaction exposing 1,3-butadiene to Bi_2O_3 at 773 K. The pseudo first-order rate constant for 1,3-butadiene activation is 1.5 μmol s^{-1} mol_O^{-1} $kPa_{C_4H_6}^{-1}$. Upon exposure of 1-butene to Bi_2O_3 in the batch reactor, 1-butene combusts to form CO_2 and dehydrogenates to form 1,3-butadiene which also combusts, as shown in Fig. S29. Analysis of the rate of 1-butene activation during this batch reaction yields a pseudo-first order rate constant of 7.1 μmol s^{-1} mol_O^{-1} $kPa_{C_4H_8}^{-1}$, which is higher than the pseudo-first order rate constant for activation of 1,3-butadiene despite a DPE for 1-butene which is 57 kJ mol^{-1} higher than the DPE of 1,3-butadiene.

The dependence of transition state energies on molecular and catalytic properties during a bond scission event can be captured with thermochemical cycles which predict that interactions between molecular fragments and the catalyst surface (or the molecular fragments themselves) can alter transition state energies. Reactivity trends with molecular descriptors such as DPE only provide complete scaling relations among different molecules if the interaction energies between the catalyst surface and the molecular fragments formed in the transition state (or the energies of interaction between the molecular fragments themselves) of a rate-determining elementary step are identical among different molecules. Differences in these energies or differences between reaction mechanisms will limit the utility of molecular descriptors as complete reactivity descriptors.

In the case of 1-butene, a low BDE of 350 kJ mol^{-1} (*31*), reflective of a stable 1-buten-3-yl radical formed upon homolytic C-H scission, may enable a more energetically favorable C-H activation route than the heterolytic C-H scission pathway hypothesized to occur for C_2H_2 or C_2H_4 activation on Bi_2O_3. During a bond scission event occurring on a catalytic surface, electrons in the bond shift either towards molecular fragments or to the catalytic surface. Assessments of bond scission as purely homolytic or purely heterolytic assume that the electron density shifts to form two radical species or a proton/anion pair, respectively. In reality, however, we expect that shifts in electron density from the reactant state to the transition state of C-H scission lie in a gradient between these two bookend cases. For C_2H_2 and C_2H_4 activation on Bi_2O_3, we hypothesize that C-H activation is more heterolytic and depends more strongly on molecular acidity, because homolytic C-H activation routes are inaccessible for activation of C_2H_2 or C_2H_4 on Bi_2O_3 due to their high BDE values of 558 kJ mol^{-1} and 464 kJ mol^{-1}, respectively (*29*), whereas C-H activation of 1-butene may be more radical-like.

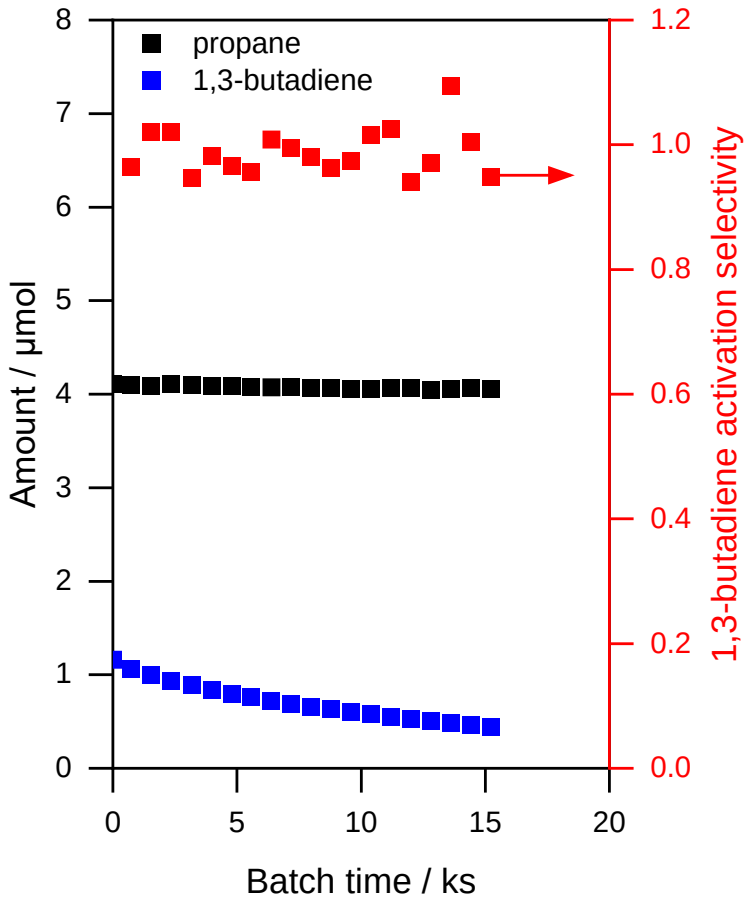

Fig. S27. Selective combustion of 1,3-butadiene in propane by Bi_2O_3

The number of moles of 1,3-butadiene and propane present in a recirculating batch reactor exposed to Bi_2O_3 at 773 K. 1,3-butadiene activation selectivity is plotted on the right y-axis and is enumerated as $S = \frac{\hat{k}(C_4H_6)}{\hat{k}(C_4H_6)+\hat{k}(C_3H_8)}$, where $\hat{k}$ denotes the pseudo-first-order rate constant for the consumption of 1,3-butadiene or propane, in µmol s^{-1} g_{cat}^{-1} kPa^{-1}. The selectivity exceeds unity at points due to a negative calculated rate of propane consumption across three consecutive data points. Assessment of the average rates of consumption of 1,3-butadiene or propane normalized by the average reactant partial pressures across the entire experiment yields a 1,3-butadiene activation selectivity of 98.5%. The extent of catalyst reduction remained below 1% throughout the experiment. Batch reaction conditions: m(Bi_2O_3)=0.4905 g, T=773 K, P(1,3-butadiene)$_0$=0.04 kPa, P(C_3H_8)=0.16 kPa, P(Ar)=51.7 kPa, balance helium.

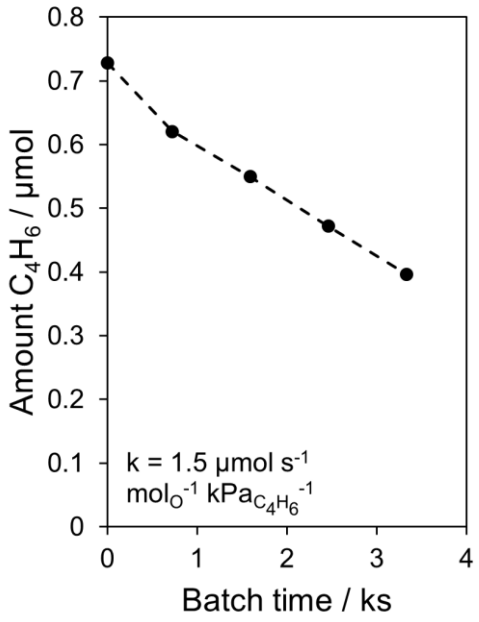

Fig. S28. 1,3-butadiene combustion by Bi_2O_3

Amount of 1,3-butadiene during a batch reaction exposing 1,3-butadiene to Bi_2O_3 at 773 K. Rates of 1,3-butadiene activation used to enumerate a pseudo first-order rate constant were assessed based on the slope between three consecutive measures of the amount of 1,3-butadiene present in the batch reactor. The extent of catalyst reduction remained below 1% throughout the experiment. Batch reaction conditions: $m(Bi_2O_3)$ = 0.52 g, T = 773 K, $P(C_4H_6)_0$ = 0.03 kPa, $P(He)_0$ = 55.6 kPa, balance argon. The batch reactor was initially pressurized to 139.8 kPa before reaction to minimize leaks of air into the reactor.

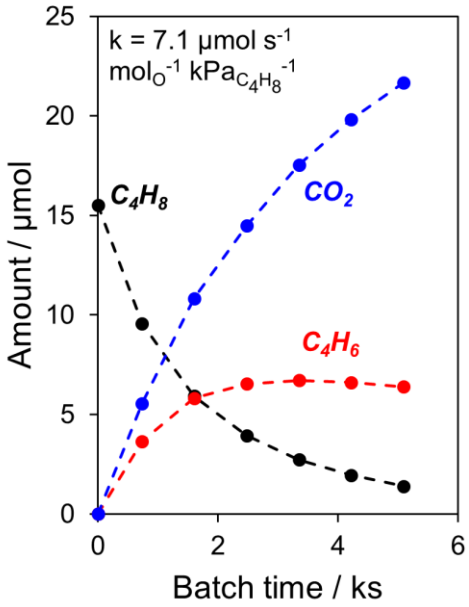

Fig. S29. 1-butene reaction on Bi_2O_3

Amounts of 1-butene, CO_2, and 1,3-butadiene during a batch reaction exposing 1-butene to Bi_2O_3 at 773 K. Rates of 1-butene activation used to enumerate the pseudo first-order rate constant were assessed based on the slope between three consecutive measures of the amount of 1-butene present in the batch reactor. The extent of catalyst reduction remained below 2% throughout the reaction. Reaction conditions: m(Bi_2O_3) = 0.5046 g, T = 773 K, P(C_4H_8)$_0$ = 0.5 kPa, balance argon. The batch reactor was initially pressurized to 139.9 kPa before reaction to minimize leaks of air into the reactor.

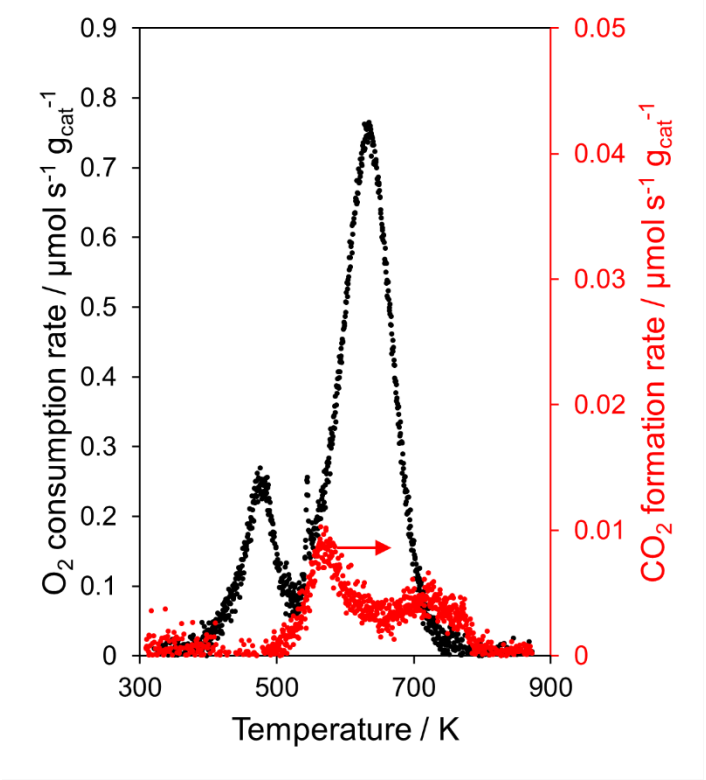

Fig. S30. Temperature programmed oxidation of partially reduced Bi_2O_3 by O_2

O_2 consumption rate and CO_2 formation rate (on the right y-axis) during a TPO experiment in which O_2 was exposed to partially reduced Bi_2O_3. The partially reduced Bi_2O_3 was prepared by an isothermal reduction at 673 K upon exposure of Bi_2O_3 to 1.0 kPa C_2H_2 at 1.67 cm^3_{STP} s^{-1} for 4.2 ks to remove 310 µmol O (θ_O = 0.84). The degree of reduction was calculated by integration of the flow rates of CO_2 and H_2O in the effluent during reduction. After reduction, the reactor was rapidly cooled to 308 K while stabilizing the O_2 flow in the bypass stream. The reoxidation was started simultaneously with the temperature program heating the catalyst from 308 K to 873 K at 0.17 K s^{-1}. The rate of O_2 consumption was tracked relative to the baseline O_2 ion intensity (m/z=32) with an Ar internal standard (m/z = 40), and the rate of CO_2 formation was tracked relative to the Ar internal standard (m/z=40). Reaction conditions: m(Bi_2O_3) = 0.2953 g, $T_{initial}$ = 308 K, ramp rate = 0.17 K s^{-1}, P(O_2) = 2.1 kPa, P(He) = 18.5 kPa, balance Ar, total flow rate = 1.67 cm^3_{STP} s^{-1}. O_2 conversion remained below 16% throughout the experiment.

Supplemental X-ray diffraction patterns

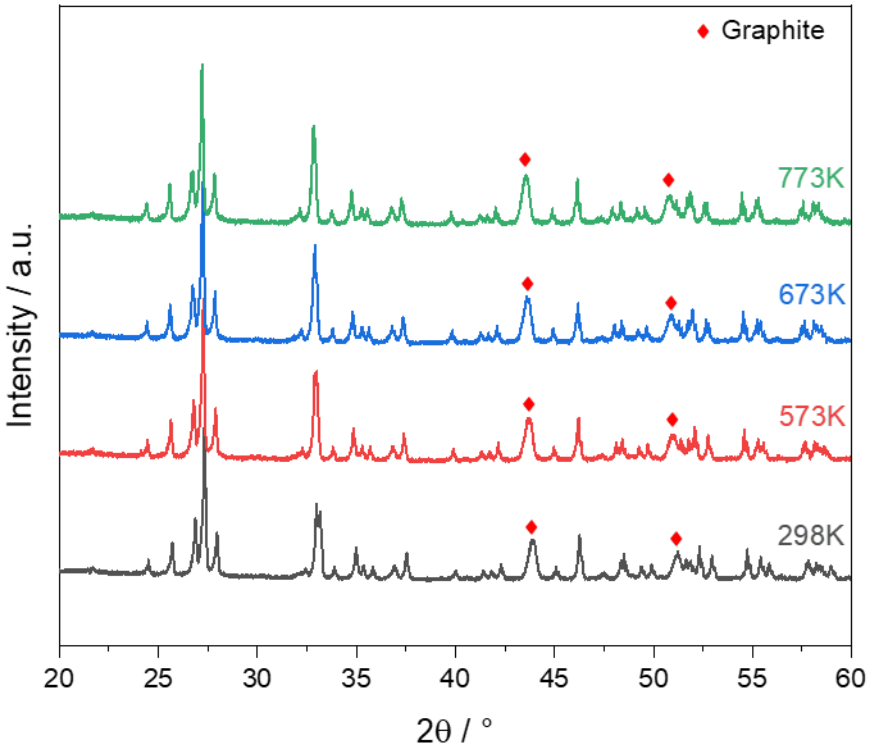

Fig. S31. XRD of fresh Bi_2O_3 at 298 K – 773 K

Temperature programmed XRD patterns for fresh α-Bi_2O_3. Peaks corresponding to the graphite dome surrounding the Bi_2O_3 sample to ensure a controlled gas environment with flowing air are denoted. No peaks corresponding to other polymorphs of Bi_2O_3 or Bi metal were detected.

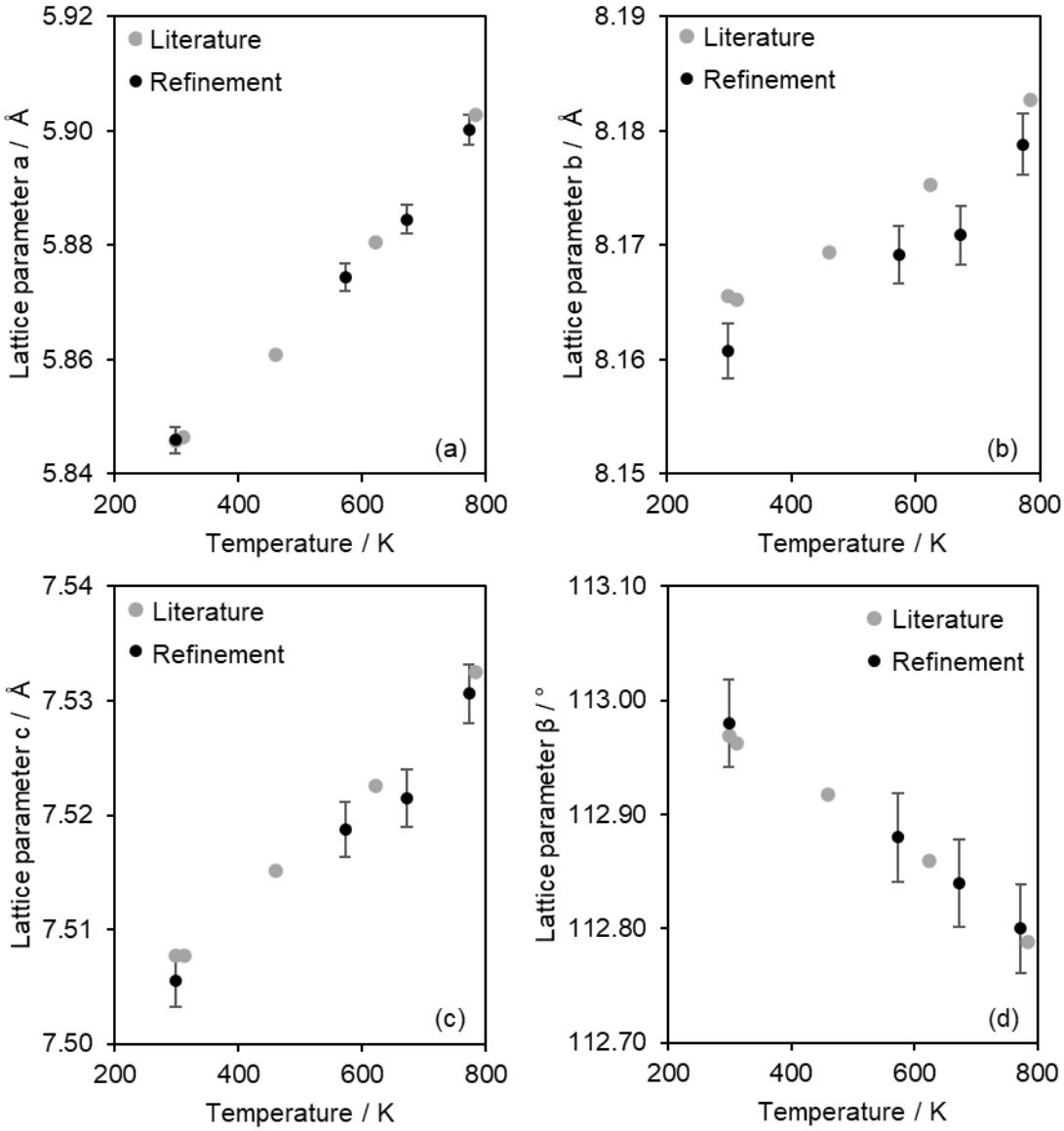

Fig. S32. Lattice parameters of Bi_2O_3 at 298 K - 773 K

Monoclinic lattice parameters (a) a, (b) b, (c) c, (d) and β evaluated by Rietveld refinement of α-Bi_2O_3 using Jade MDI software (*55*) from the temperature-programmed XRD patterns shown in Fig. S19, compared to the lattice parameters reported by Yashima et al. (*34*) The reported lattice parameters correspond to the parameters which yield the lowest χ^2 value (i.e. the smallest difference between the calculated and real XRD patterns). Initial a, b, c, and β values used in refinement were 5.8444 Å, 8.1574 Å, 7.5032 Å, and 112.97°, respectively, as reported by Ivanov et al. (*32*). Regions containing peaks from the graphite dome used to maintain a controlled gas environment were excluded from the fitting.

Characterization of partially reduced Bi_2O_3

Partially reduced Bi_2O_3 samples were prepared to understand how the phase, coordination environment, and Bi oxidation state change upon partial reduction by C_2H_2 combustion. Reduced Bi_2O_3 samples were prepared by reduction with C_2H_2 at 673 K in a recirculating batch reactor. Each sample was reduced to a known extent (8%, 17%, and 28%) which was enumerated via the oxygen mole balances shown in Eqs. S1 and S2. Following reduction, the samples were cooled to ambient conditions in inert gas.

Ex situ XRD was employed to understand the differences in bulk phases exhibited upon partial reduction. Fig. S33 shows XRD patterns of each of the Bi_2O_3 samples. An increase in the degree of reduction lead to a monotonic increase in peaks corresponding to Bi metal, which is consistent with peaks for Bi metal observed by XRD in a sample reduced to $\theta_O = 0.8$, shown in Fig. S34. Despite the formation of metallic Bi domains, the crystallinity of each of the samples is imperceptibly affected by partial reduction. Although these results show that samples reduced by C_2H_2 combustion and cooled to ambient conditions contain both α Bi_2O_3 and Bi metal domains, the catalyst at reaction conditions may contain stoichiometric α Bi_2O_3, oxygen-deficient α Bi_2O_3, Bi metal, or a combination thereof.

Each of the partially reduced Bi_2O_3 samples were also characterized by ex situ XAS measurements to understand the evolution of the bulk-averaged Bi coordination environment and oxidation state upon partial reduction of the oxide. Fig. S35a and Fig. S35b show normalized absorbances at the Bi L_3-edge which exhibit a monotonic decrease in white line intensity with increasing extent of reduction, consistent with reduction of Bi^{3+} cations present in Bi_2O_3. Abstraction of lattice oxygen by combustion liberates two electrons which can either delocalize through the oxide or reduce nearby Bi sites to result in the observed reduction. Isosbestic points observed in the pre- and post-edge oscillations in Fig. S35b indicate that the reduction process results in the formation of an absorbing Bi species with a distinct chemical environment from Bi^{3+} in Bi_2O_3; the absorbance spectra represent a superposition of the individual spectra of these species. A forward Fourier-transform was applied to the data with 4.01 $Å^{-1} < k < 12.4$ $Å^{-1}$. k^2-weighted $\chi(k)$ oscillations between 1 $Å^{-1}$ and 7 $Å^{-1}$ are dampened upon reduction (see Fig. S35c), and the magnitude of Fourier-transformed $\chi(R)$ oscillations exhibits reduction in the intensity of scattering paths at ~ 1.7 Å and 3.5 Å and changes in intensity of the scattering features at ~ 2.6 Å (see Fig. S35d).

We employed EXAFS fitting using Artemis XAS data processing software to understand the evolution of the oxides upon reduction by C_2H_2. Considering the observation of metallic Bi domains from X-ray diffraction patterns of partially reduced Bi_2O_3 samples and the observation of isosbestic points in the Bi L_3 edge, the fitting procedures assess whether the EXAFS data is consistent with a physical mixture of Bi_2O_3 particles and Bi metal. XAS is a bulk-averaged technique which reflects a convolution of all chemical environments surrounding all Bi atoms in the sample. The α Bi_2O_3 unit cell has a monoclinic structure with two unique Bi sites, so the Bi_2O_3 scattering paths used in EXAFS fitting were obtained by utilizing the aggregate function in Artemis, which averages scattering paths between the unique Bi sites to obtain effective scattering paths for one Bi site, with a margin of 0.1 Å and a beta value of 3°. All samples were fit using one Bi-O scattering path in α Bi_2O_3 (N = 2.5, R = 2.174 Å) and one Bi-Bi scattering path in α Bi_2O_3 (N = 2.5, R = 3.574 Å) which were obtained using the aggregate function in Artemis. For partially reduced samples, a Bi-Bi scattering path (N = 3, R = 3.110 Å) was also included. Coordination numbers were fixed in the fits. The fraction of Bi_2O_3, denoted by x, and the fraction of Bi metal, denoted by (1-x), were assessed for each sample. An amplitude reduction factor of 0.74 was used,

and fitting was conducted with a k range of 4.01 $Å^{-1}$ < k < 12.4 $Å^{-1}$ (dk = 1 $Å^{-1}$) and an R range of 1 Å < R < 4 Å (dR = 0 Å) and a Hanning window. All samples were fit at the same time and share the same R and σ^2 values which were optimized in the fitting procedure along with x values for each sample and ΔE values for the Bi_2O_3 paths and metallic Bi path.

The k-space oscillations, imaginary component of Fourier-transformed EXAFS χ(R), and magnitude of Fourier-transformed EXAFS χ(R), along with the corresponding fits, are shown in Figs. S36 – S38, for the partially reduced Bi_2O_3 samples. Table S3 contains a summary of the fit parameters for the Bi-O and Bi-Bi paths in Bi_2O_3 and the Bi-Bi path in Bi metal. An R-factor of 1.90% and good agreement between the data and EXAFS fits in Figs. S36 - S38 demonstrates that the EXAFS data is consistent with the partially reduced Bi_2O_3 samples containing physical mixtures of Bi_2O_3 and Bi metal. Using the x-values obtained from the fitting procedure, Fig. S39 compares the extent of reduction of the samples as assessed by enumeration of the number of oxygen atoms removed from the samples by C_2H_2 combustion in a recirculating batch reactor to the extent of reduction of the samples as assessed by the x values obtained from the EXAFS fitting procedures. Parity between the two values within error implies that upon cooling to ambient conditions, partially reduced Bi_2O_3 samples separate into two phases: one stoichiometric Bi_2O_3 phase and one O-deficient metallic Bi phase. As previously noted, however, these results cannot discriminate between sole existence of an O-deficient Bi_2O_3 phase, the coexistence of an O-deficient Bi_2O_3 phase and a metallic Bi phase, or coexistence between a stoichiometric Bi_2O_3 phase and a metallic Bi phase at reaction conditions.

To supplement the results from ex situ characterization of fresh and partially reduced Bi_2O_3 particles by XAS and XRD, which probe structural and electronic changes throughout the bulk of the particles, we performed XPS analyses of fresh and 28% reduced Bi_2O_3 particles. Fig. S40 shows Bi 4f peaks for fresh and 28% reduced Bi_2O_3. The Bi 4f peaks exhibit symmetric bands for the Bi 4f 5/2 and Bi 4f 7/2 peaks with area ratios of 0.75 for the doublet located at 164.1 eV and 158.8 eV (corresponding to Bi^{3+} in Bi_2O_3) and the doublet located at 162.2 eV and 157.0 eV (corresponding to Bi^0 in Bi metal) (*56*). The 28% reduced sample exhibits peaks for Bi metal which are not observed in the fresh Bi_2O_3 sample, consistent with the observation of Bi metal in the 28% reduced sample from XRD and the EXAFS results which are consistent with presence the of metallic Bi domains in partially reduced samples. The results of the peak deconvolution are shown in Table S4.

Fig. S41 shows the O 1s peak for fresh and 28% reduced Bi_2O_3. Both samples have a dominant peak for lattice oxygen (O^{2-}) at ~ 529.6 eV and a shoulder at ~530.7 eV which has been ascribed to surface hydroxyls (*56, 57*). Table S5 summarizes the energy and fraction of total area for each fitted peak. The area percent of the O^{2-} peak at 529.6 eV is slightly lower in the 28% reduced sample than the fresh sample.

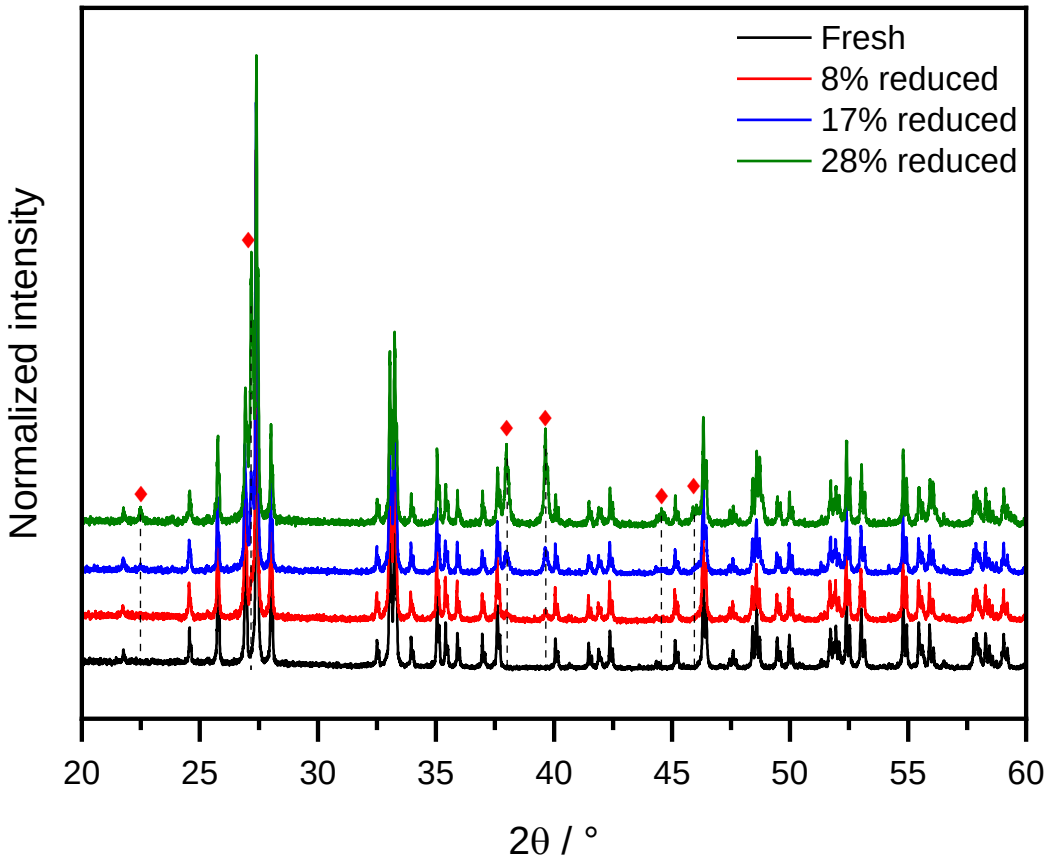

Fig. S33. XRD of partially reduced Bi_2O_3 samples

X-ray diffraction patterns for a fresh Bi_2O_3 catalyst and Bi_2O_3 samples which have been partially reduced to known extents in a batch reactor upon exposure to C_2H_2 at 673 K. Diffraction peaks corresponding to Bi metal are denoted with red diamonds. Intensities were normalized by the maximum intensity during a scan. All samples were exposed to air prior to and during scans.

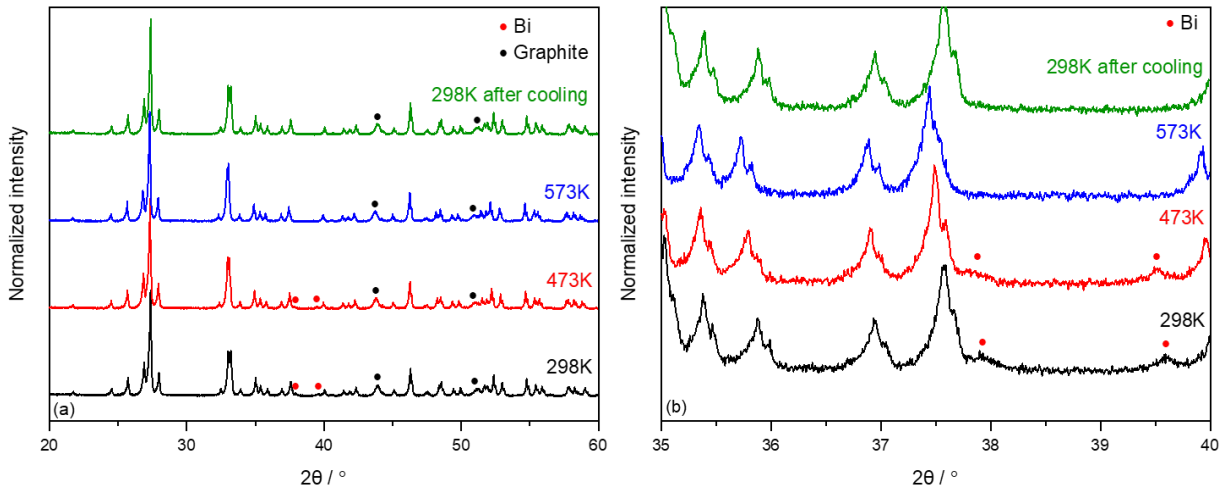

Fig. S34. XRD of reduced Bi_2O_3 at 298 K – 573 K

(a) Temperature programmed XRD patterns for α-Bi_2O_3 after reduction to $\theta_O = 0.8$ by C_2H_2 at 663 K in a recirculating batch reactor, and (b) the region from $35° < 2\theta < 40°$, showing the peaks for metallic Bi. After reduction, the catalyst was isolated in argon and cooled to ambient conditions before being loaded into the Anton Parr in situ XRD cell. Peaks corresponding to the graphite dome surrounding the Bi_2O_3 sample to ensure a controlled gas environment with flowing nitrogen are denoted. No peaks corresponding to other polymorphs of Bi_2O_3 were detected. Small peaks corresponding to metallic Bi were present in the sample at 298 K and 473 K but disappeared after heating above the melting point of Bi (m.p. = 546 K). The metallic peaks did not reappear after cooling the sample back down to 298 K. Intensities were normalized by the maximum intensity during a scan.

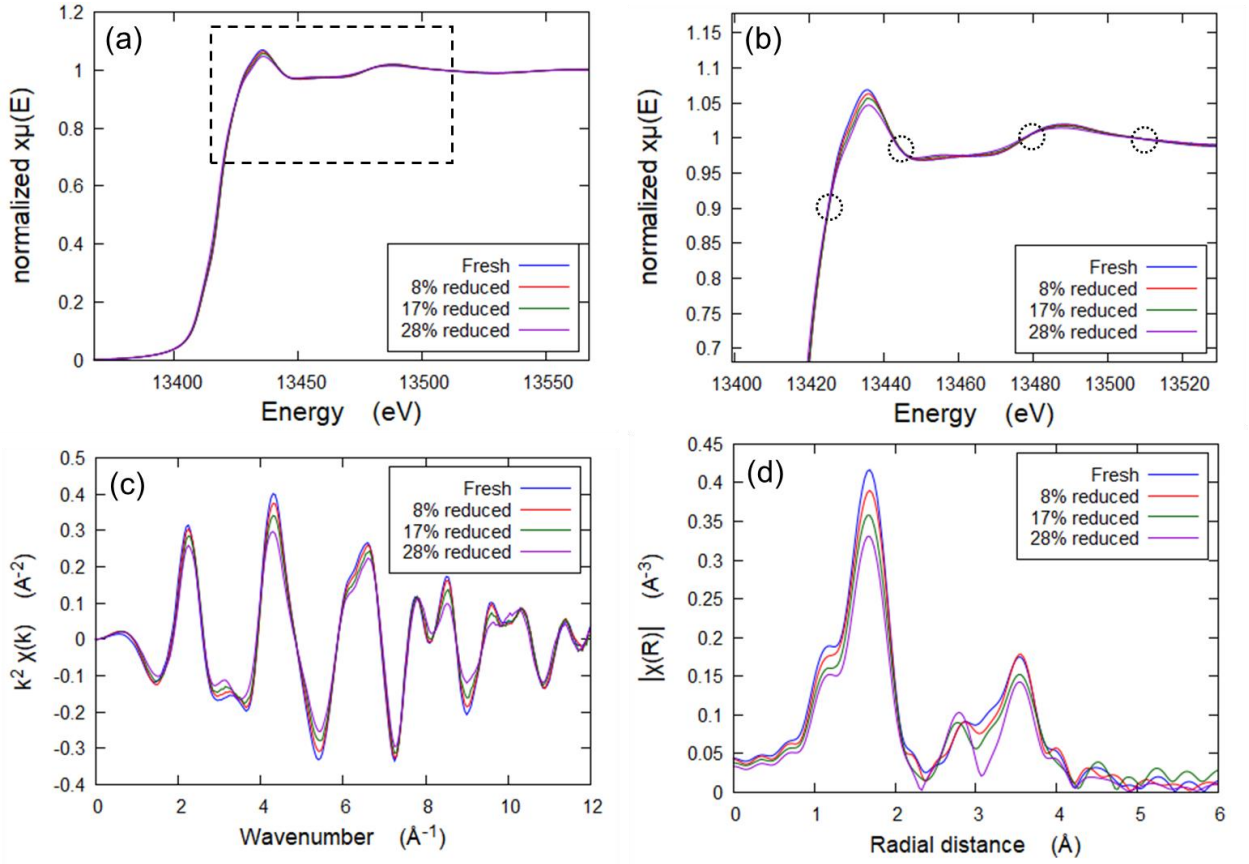

Fig. S35. X-ray absorption spectra of partially reduced Bi_2O_3 samples

Ex situ XAS spectra of fresh and partially reduced bismuth oxide samples, showing the (a) Bi L_3 absorption edge, (b) the white line of the Bi L_3 adsorption edge (showing the area highlighted by the dashed lines in (a) with isosbestic points denoted by the dashed circles), (c) the k^2-weighted $\chi(k)$ oscillations, and (d) magnitude of the Fourier-transformed $\chi(R)$ oscillations.

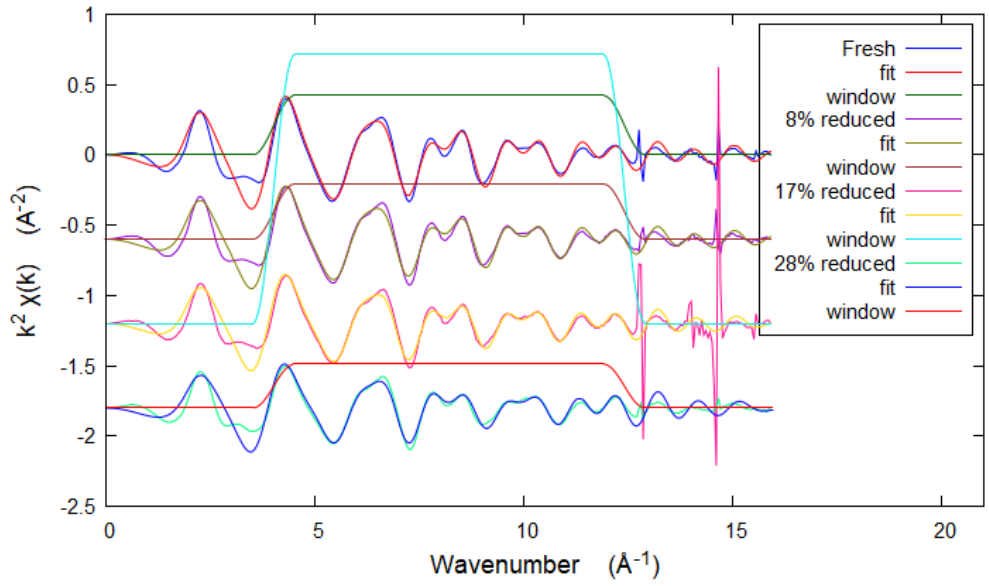

Fig. S36. k-space oscillations for partially reduced Bi_2O_3 samples

k^2-weighted k-space oscillations and the EXAFS fits and window for each sample. The large spikes in k-space observed between 12 $Å^{-1}$ and 15 $Å^{-1}$ are due to glitches in the data which are larger in samples with a lower edge step. All EXAFS data for the fresh and partially reduced Bi_2O_3 samples was fit with one fitting procedure.

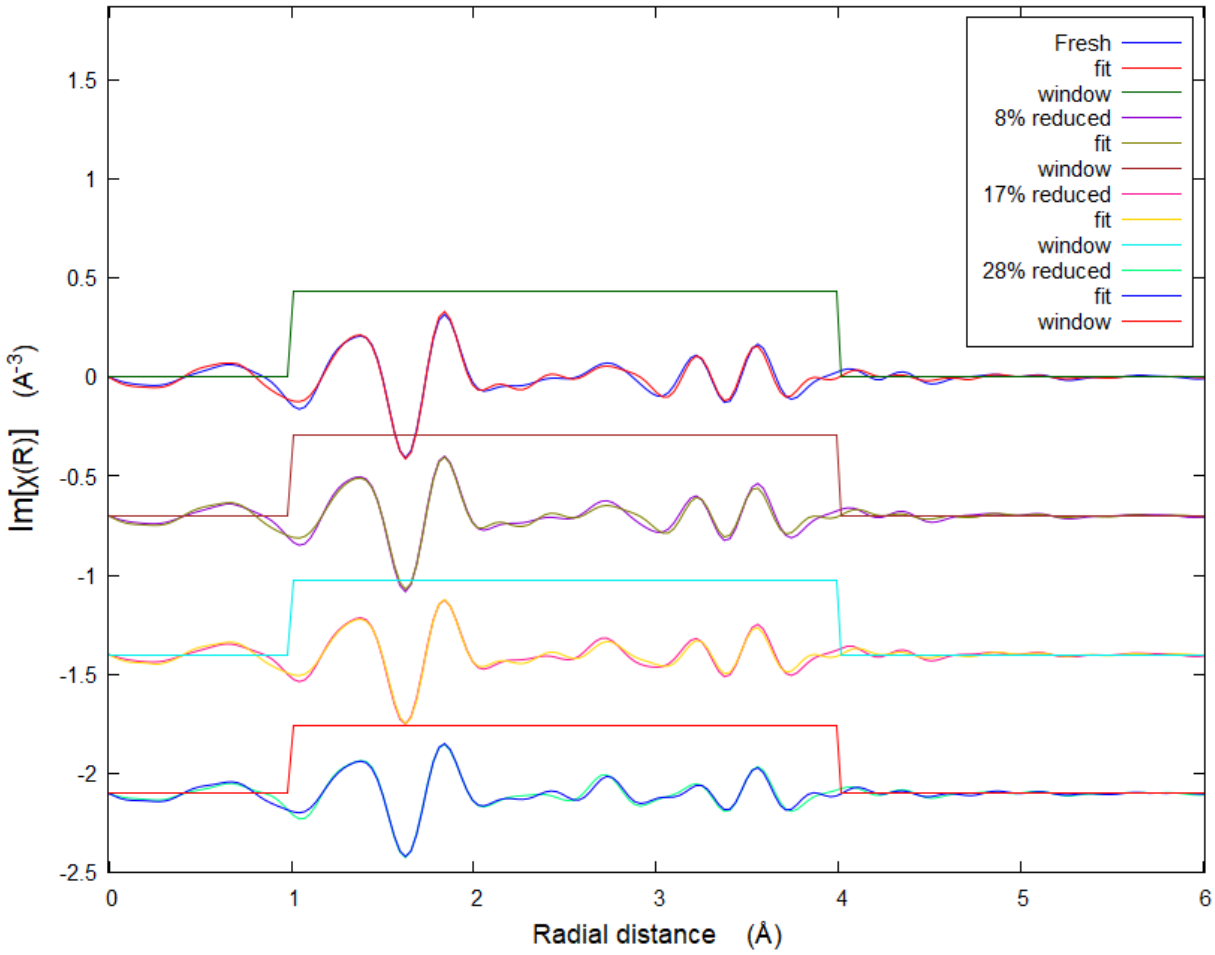

Fig. S37. Imaginary χ(R) for partially reduced Bi_2O_3 samples

Imaginary component of Fourier-transformed EXAFS χ(R) and the EXAFS fits and window for each sample. All EXAFS data for the fresh and partially reduced Bi_2O_3 samples was fit with one fitting procedure.

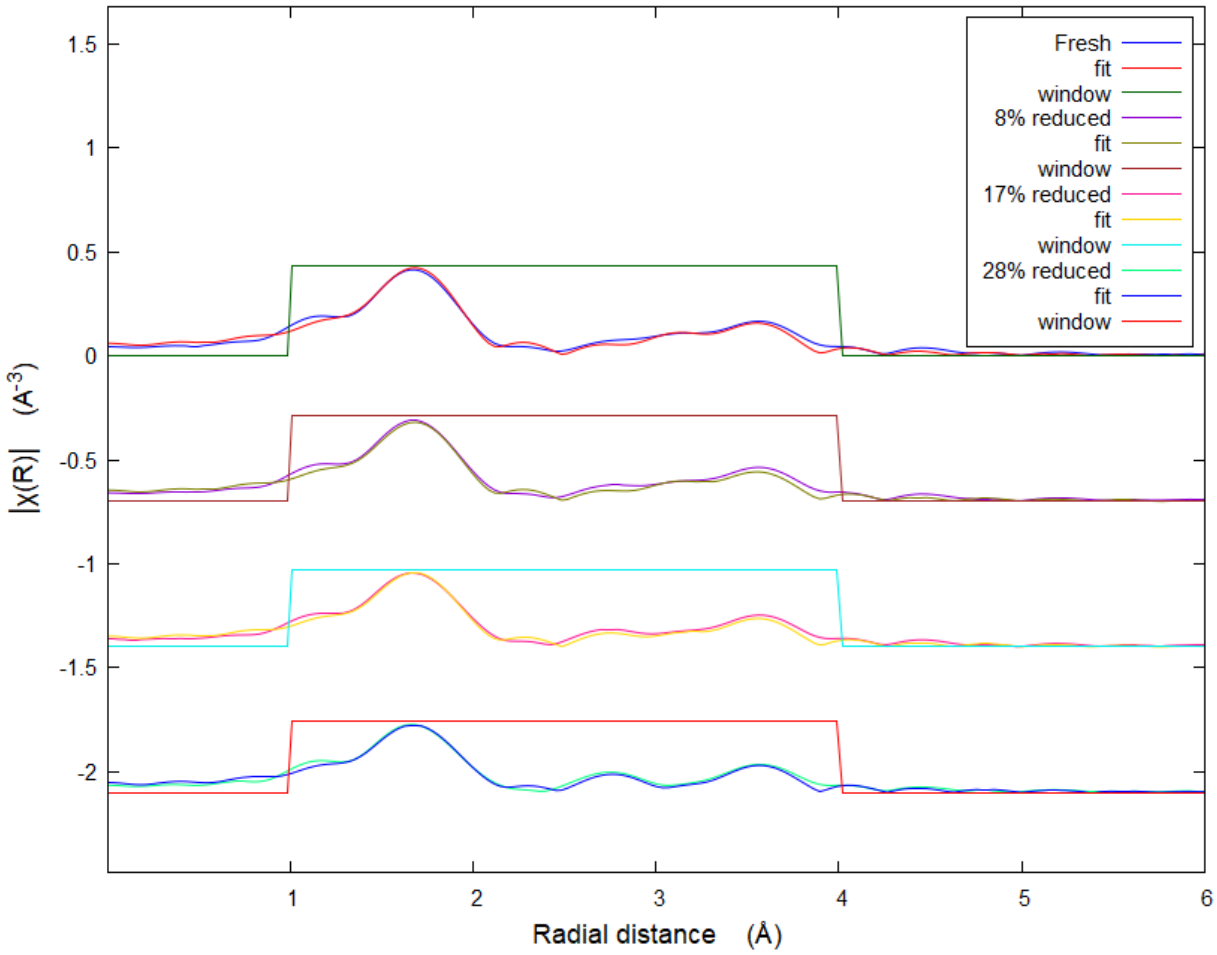

Fig. S38. Magnitude of χ(R) for partially reduced Bi_2O_3 samples

Magnitude of Fourier-transformed EXAFS χ(R) and the EXAFS fits and window for each sample. All EXAFS data for the fresh and partially reduced Bi_2O_3 samples was fit with one fitting procedure.

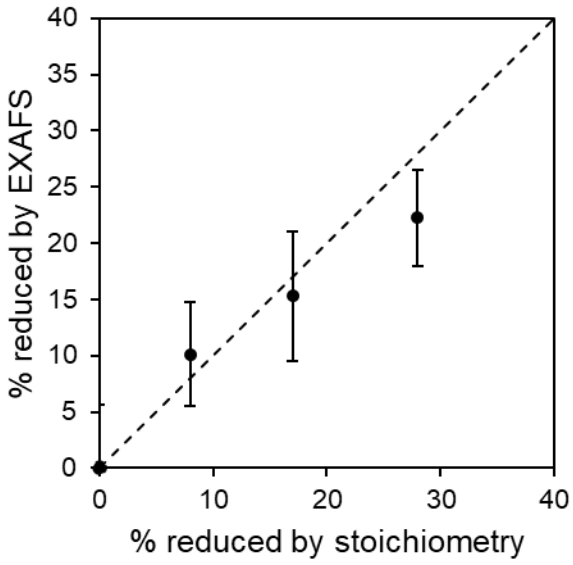

Fig. S39. Degrees of reduction assessed by stoichiometry and by EXAFS fitting

Degrees of reduction assessed by stoichiometry were enumerated via mole balances counting the amount of O removed as H_2O and CO_2 upon exposure of Bi_2O_3 to C_2H_2 at 673 K in a recirculating batch reactor. After reduction, samples were cooled to ambient conditions in inert gas. Degrees of reduction from EXAFS for partially reduced Bi_2O_3 samples were assessed based on the mole fractions obtained when fitting the samples as a physical mixture of fully oxidized α Bi_2O_3 (x) and Bi metal (1-x).

Table S3. EXAFS fitting parameters for fresh and partially reduced Bi_2O_3 samples

Scattering path	N	R / Å	σ^2 / Å^2
Bi-O	2.5	2.15 ± 0.01	0.0047 ± 0.0004
Bi-Bi (Bi_2O_3)	2.5	3.57 ± 0.01	0.0058 ± 0.0004
Bi-Bi (metal)	3	3.09 ± 0.02	0.0029 ± 0.0016

Amplitude reduction factor fixed at 0.74.
$\Delta E(Bi_2O_3)$ = -2.97 ± 0.56 eV
ΔE(Bi metal) = -3.01 ± 5.13 eV
R-factor = 2.06%
Reduced χ^2 = 3445
The fit included data for each sample.

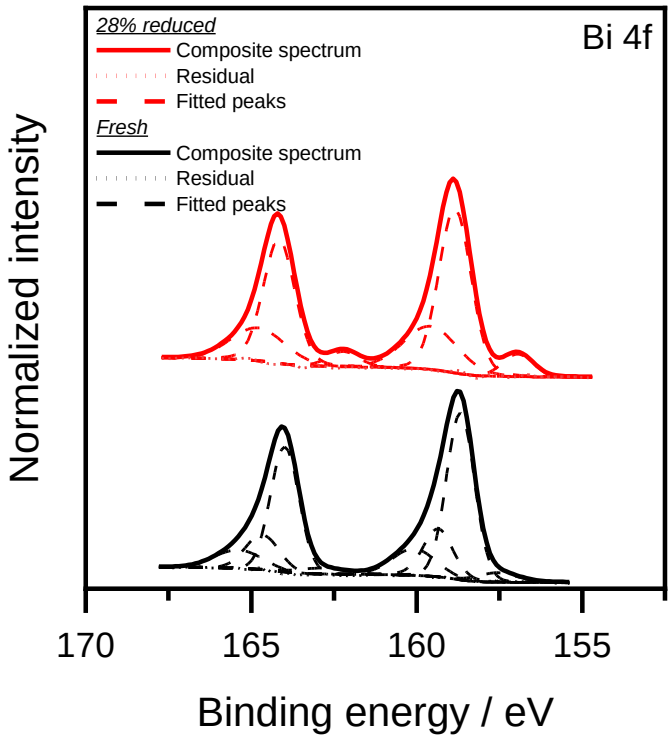

Fig. S40. Bi 4f XPS of fresh and 28% reduced Bi_2O_3

Bi 4f 5/2 and Bi 4f 7/2 XPS peaks for fresh and 28% reduced Bi_2O_3 with area ratios fixed at 0.75 for the doublets located at 164.1 eV and 158.8 eV (corresponding to Bi^{3+} in Bi_2O_3) and the doublet located at 162.2 eV and 157.0 eV (corresponding to Bi^0 in Bi metal). The composite spectrum represents the contributions from each of the fitted peaks shown. The residual corresponds to the difference between the measured and composite spectrum after background subtraction. Intensities were normalized by the maximum intensity during a scan.

Table S4. Bi 4f XPS peak energies and area percents for fresh and 28% reduced Bi_2O_3 samples.

Fresh Bi_2O_3			28% reduced Bi_2O_3		
Energy / eV	Area %	Phase	Energy / eV	Area %	Phase
157.5	3.0	Bi_2O_3	157.0	4.5	Bi
158.7	34.5	Bi_2O_3	158.9	36.7	Bi_2O_3
159.4	11.3	Bi_2O_3	159.6	15.9	Bi_2O_3
160.1	8.4	Bi_2O_3	162.2	3.4	Bi
162.9	2.2	Bi_2O_3	164.2	27.5	Bi_2O_3
164.0	25.9	Bi_2O_3	164.8	12.0	Bi_2O_3
164.7	8.5	Bi_2O_3			
165.4	6.3	Bi_2O_3			

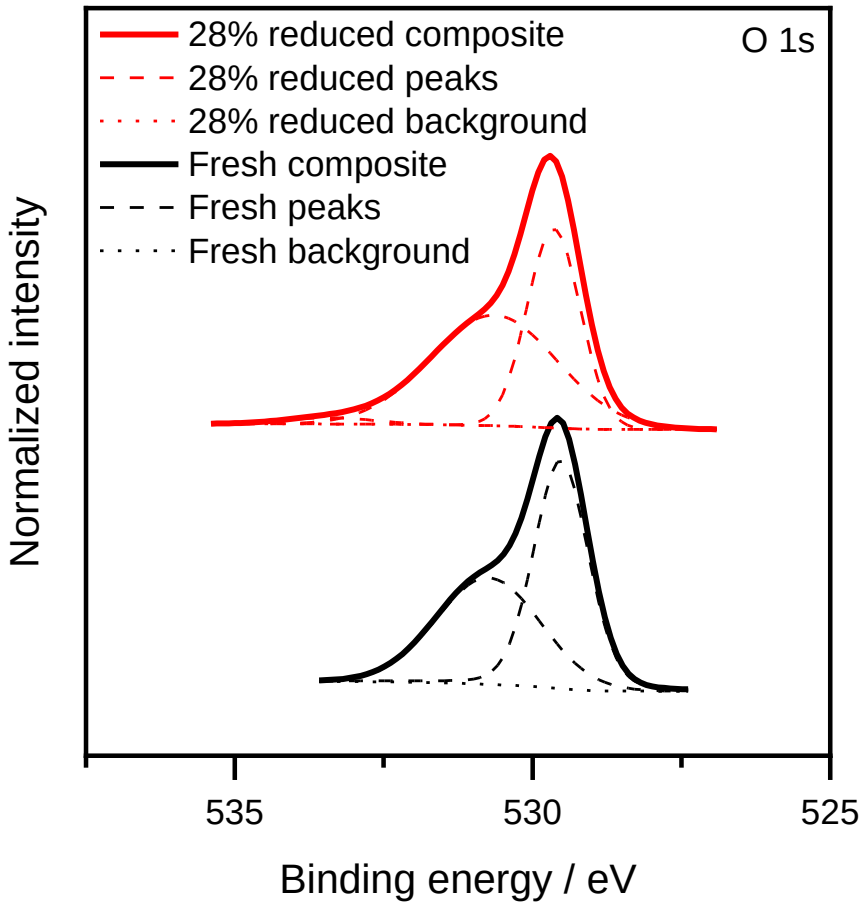

Fig. S41. O 1s XPS of fresh and 28% reduced Bi_2O_3

O 1s XPS peaks for fresh Bi_2O_3 and 28% reduced Bi_2O_3, with the composite spectrum, fitted peaks, and residuals shown. The residual corresponds to the difference between the measured and composite spectrum after background subtraction. Intensities were normalized by the maximum intensity during a scan.

Table S5. O 1s XPS peak energies and area percents for fresh and 28% reduced Bi_2O_3 samples.

Fresh Bi_2O_3		28% reduced Bi_2O_3	
Energy / eV	Area %	Energy / eV	Area %
529.5	54.5	529.6	42.2
530.7	45.5	530.7	55.7
		533.4	2.1

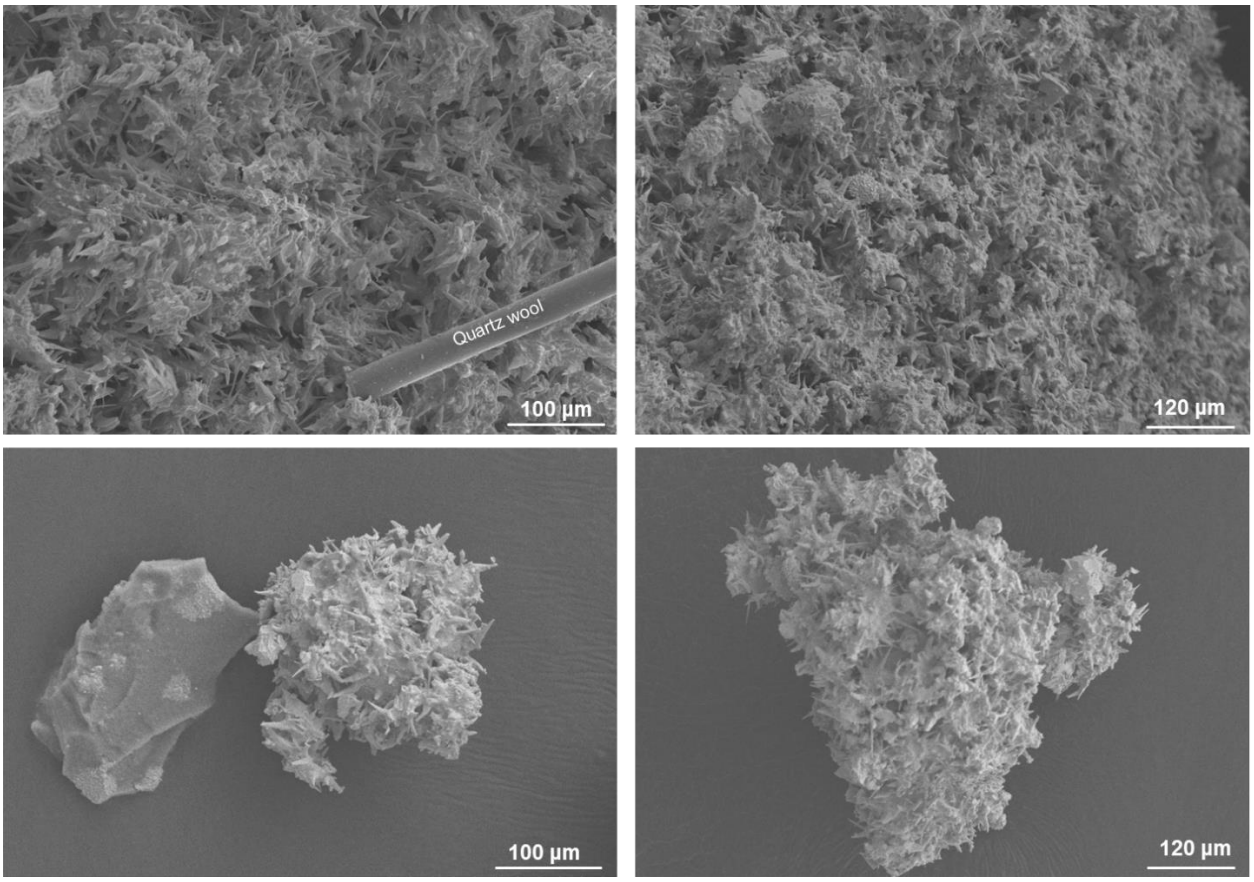

Fig. S42. SEM images of redox-cycled Bi_2O_3

SEM images of redox-cycled Bi_2O_3. See Figs. S3 and S4 for protocols reporting formulation of the redox-cycled Bi_2O_3 sample. In the top-left image, a piece of quartz wool used to support the catalyst within the reactor is denoted.

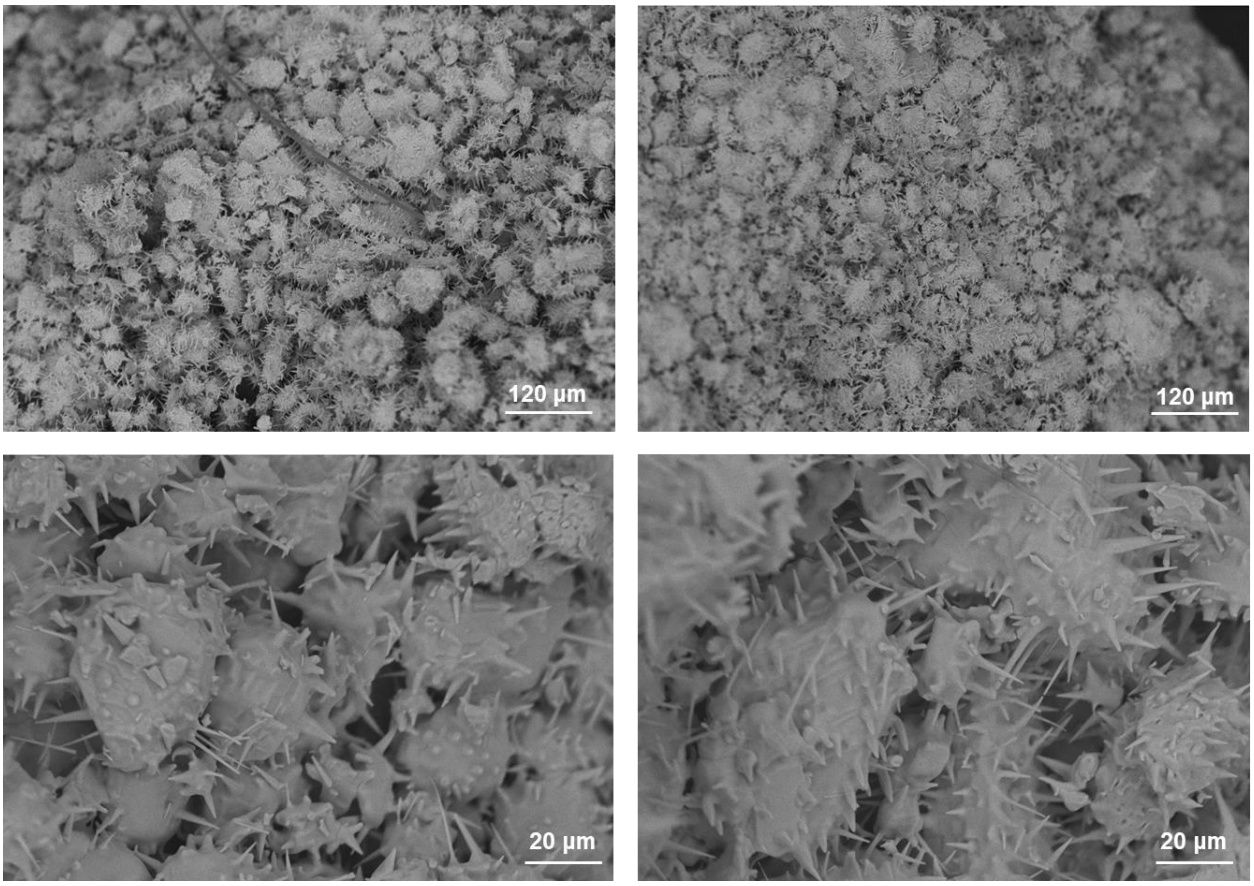

Fig. S43. SEM images of redox cycled Bi_2O_3 at θ_O > 0.9

SEM images of the redox-cycled Bi_2O_3 sample prepared by the procedures outlined in Figs. S7 and S8, in which θ_O was maintained above a value of 0.9 by employing shorter reduction steps. Like the redox-cycled Bi_2O_3 maintained at θ_O above 0.7 (detailed in Fig. 1, E to F, and Figs. S3 and S4), the sample exhibits a surface with needle-like structures.

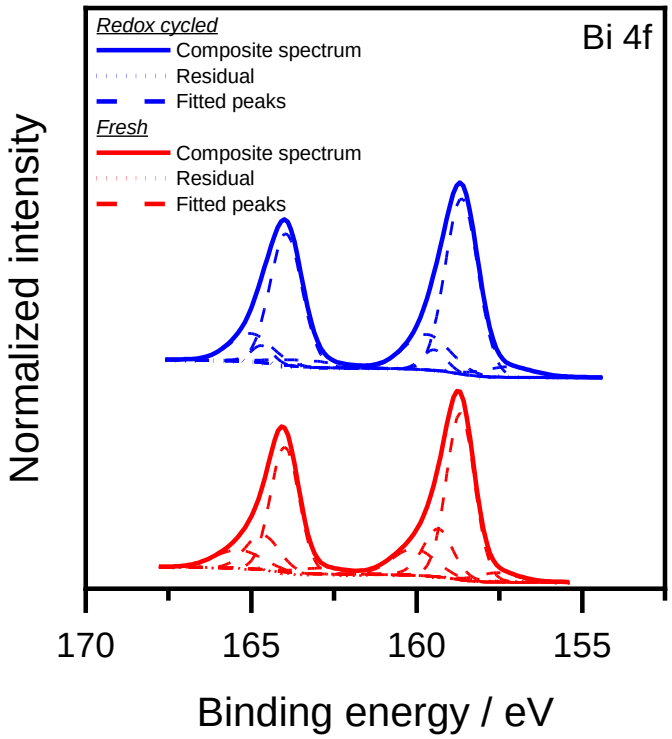

Fig. S44. Bi 4f XPS of fresh and redox-cycled Bi_2O_3

Bi 4f 5/2 and Bi 4f 7/2 XPS peaks for fresh and redox-cycled Bi_2O_3, with area ratios between the doublet located at 164.1 eV and 158.8 eV fixed at 0.75. Multiple Gaussian curves were fit within each peak to account for the observed asymmetry of the Bi 4f 5/2 and Bi 4f 7/2 peaks. The composite spectrum represents the sum of each fitted peak, and the residual corresponds to the difference between the measured and composite spectrum after background subtraction. No peaks corresponding to Bi metal at 162.2 or 157.0 eV were observed. Intensities were normalized by the maximum intensity during a scan.

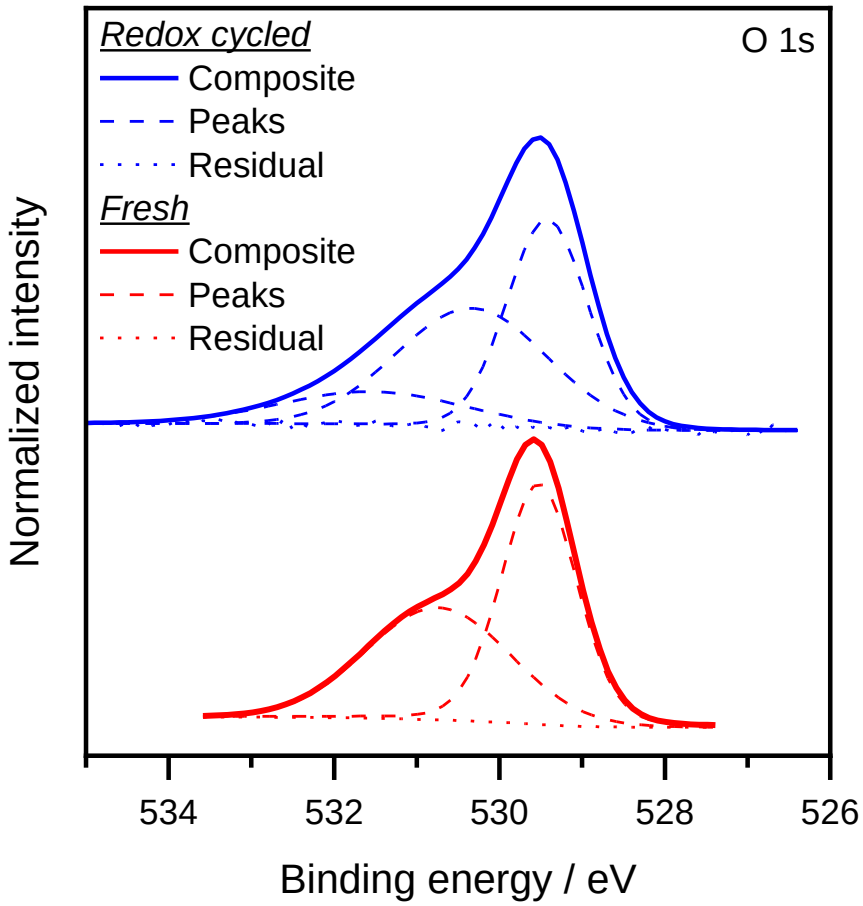

Fig. S45. O 1s XPS of fresh and redox-cycled Bi_2O_3

O 1s XPS peaks for fresh Bi_2O_3 and redox-cycled Bi_2O_3, with the composite spectrum, fitted peaks, and residuals shown. The residual corresponds to the difference between the measured and composite spectrum after background subtraction. Intensities were normalized by the maximum intensity during a scan.

XAS results for redox-cycled and fresh Bi_2O_3 samples

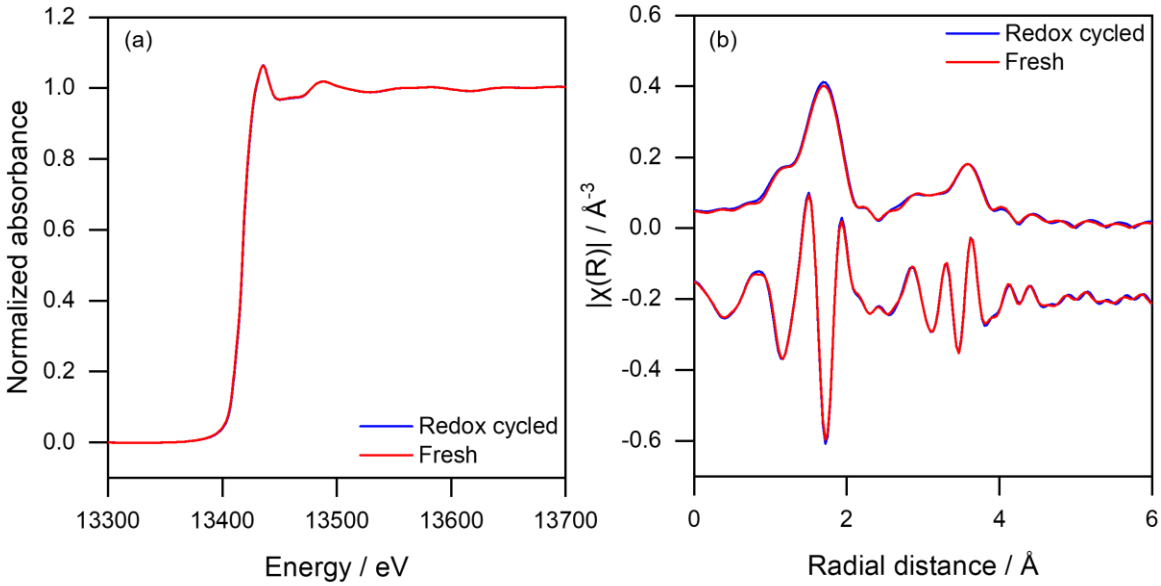

Fig. S46. XAS comparisons between fresh and redox-cycled Bi_2O_3

Comparison of (a) the XANES at the Bi L_{III}-edge and (b) the magnitude of Fourier-transformed k^2-weighted $\chi(R)$ oscillations (4.01 $Å^{-1} < k < 13.4$ $Å^{-1}$ and 1 Å < r < 4 Å), as well as the imaginary k^2-weighted $\chi(R)$ oscillations (offset by -0.2 $Å^{-3}$), for a fresh and redox-cycled Bi_2O_3 sample (see Figs. S3 and S4 for preparation procedures). Absorbances were normalized after background subtraction to yield an edge step of unity.

Table S6. EXAFS fitting parameters of fresh Bi_2O_3

EXAFS fitting parameters obtained by fitting the EXAFS region of a fresh Bi_2O_3 sample to three independent first-shell Bi-O scattering paths and one Bi-Bi scattering path of α-Bi_2O_3 with 4.01 $Å^{-1} < k < 13.4 Å^{-1}$, dk = 1, 1 Å < r < 4.1 Å, and dr = 0. The fitting procedures yielded an amplitude reduction factor of 0.74 ± 0.08, an E_0 of -0.2 ± 1.1, and an R-factor of 1.07%. N is the coordination number, R is the bond length, and σ^2 is the mean square disorder parameter.

Scattering path	N	R / Å	σ^2 / $Å^2$
Bi-O1	3	2.16 ± 0.01	0.0061 ± 0.0009
Bi-O2	2	2.55 ± 0.05	0.029 ± 0.008
Bi-O3	1	3.39 ± 0.03	0.005 ± 0.003
Bi-Bi	4.5	3.58 ± 0.01	0.0086 ± 0.0008

Table S7. EXAFS fitting parameters of redox-cycled Bi_2O_3

EXAFS fitting parameters obtained by fitting the EXAFS region of a redox-cycled Bi_2O_3 sample (see Figs. S3 and S4 for preparation procedures) to three independent first-shell Bi-O scattering paths and one Bi-Bi scattering path of α-Bi_2O_3 with 4.01 $Å^{-1}$ < k < 13.4 $Å^{-1}$, dk = 1, 1 Å < r < 4.1 Å, and dr = 0. The fitting procedures yielded an amplitude reduction factor of 0.79 ± 0.07, a E_0 of 0.05 ± 1.0, and an R-factor of 0.99%. N is the coordination number, R is the bond length, and σ^2 is the mean square disorder parameter.

Scattering path	N	R / Å	σ^2 / $Å^2$
Bi-O1	3	2.16 ± 0.01	0.0064 ± 0.0009
Bi-O2	2	2.54 ± 0.04	0.026 ± 0.006
Bi-O3	1	3.39 ± 0.02	0.006 ± 0.003
Bi-Bi	4.5	3.58 ± 0.01	0.0089 ± 0.0007

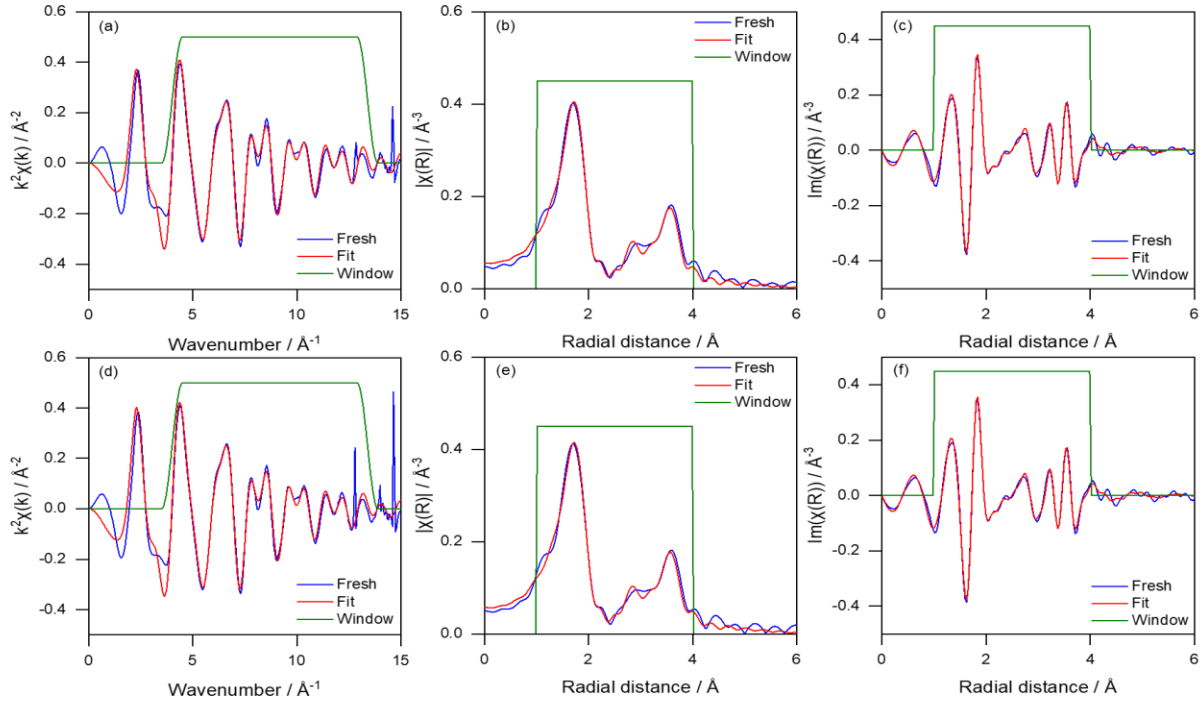

Fig. S47. EXAFS fits of fresh and redox-cycled Bi_2O_3

The (a) k^2-weighted k-space oscillations, (b) magnitude of the Fourier-transformed k^2-weighted $\chi(R)$ oscillations (4.01 $Å^{-1}$ < k < 13.4 $Å^{-1}$ and 1 Å < r < 4 Å), and (c) the imaginary part of k^2-weighted $\chi(R)$ oscillations for a fresh Bi_2O_3 sample, compared to the EXAFS fits, and the (d) k^2-weighted k-space oscillations, (e) magnitude of the Fourier-transformed k^2-weighted $\chi(R)$ oscillations (4.01 $Å^{-1}$ < k < 13.4 $Å^{-1}$ and 1 Å < r < 4 Å), and (f) the imaginary part of k^2-weighted $\chi(R)$ oscillations for a redox-cycled Bi_2O_3 sample (see Figs. S3 and S4 for preparation procedures), compared to the EXAFS fits. Hanning windows (dk = 1.0, dr = 0) are also shown.

Comparison of STEM images of fresh and redox-cycled Bi_2O_3

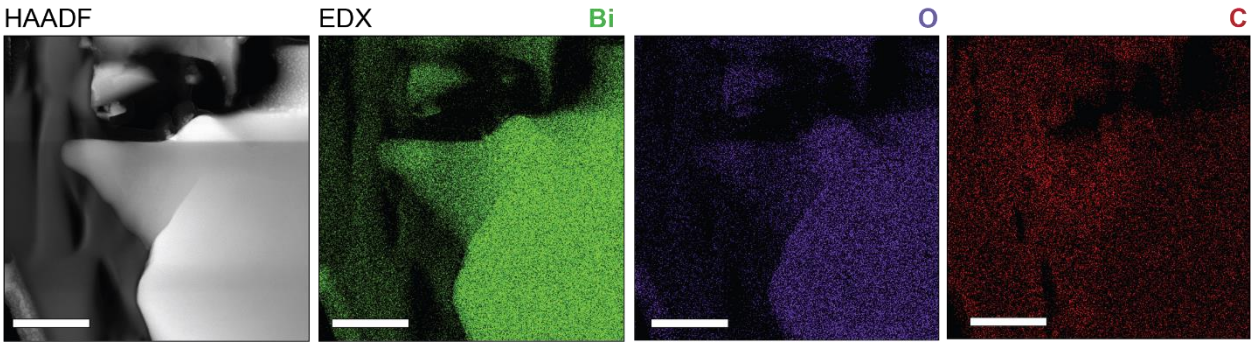

Fig. S48. STEM characterization of redox-cycled Bi_2O_3

Low-magnification HAADF-STEM image and complimentary STEM-EDX composition maps of the redox-cycled Bi_2O_3 sample showing observed distributions of Bi, O atoms. EDX signal of C originated from protective capping layer deposited on the sample before FIB-cutting of a lamella. Scale bars are 0.5 μm.

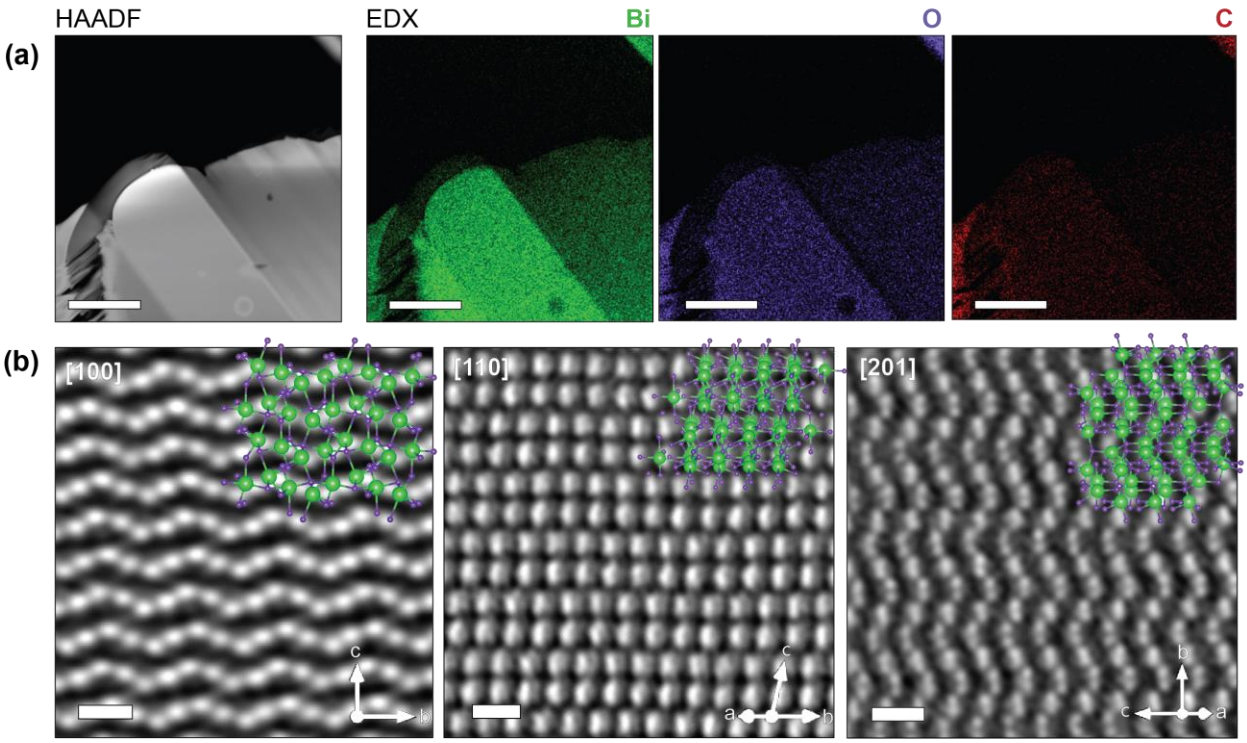

Fig. S49. STEM characterization of fresh Bi_2O_3.

(a) Low-magnification HAADF-STEM image and complimentary STEM-EDX composition map of a fresh Bi_2O_3 sample showing expected distribution of Bi, O atoms. EDX signal of C originated from protective capping layer deposited on the sample before FIB-cutting of a lamella. Scale bars are 2 μm. (b) Atomic-resolution HAADF-STEM images from the sample obtained from three high symmetry zone axis axes: [100], [110] and [201], confirming the structure of α-Bi_2O_3. The images are low-pass filtered for clarity. The atomic model of α-Bi_2O_3 structures is overlayed on each image to show the match. Scale bars are 0.5 nm.